FIRAT UNIVERSITY
GRADUATE SCHOOL OF NATURAL AND APPLIED SCIENCES
TURKEY

MAGNETIC AND THERMAL PROPERTIES OF CoFeNi-BASED HIGH ENTROPY ALLOYS

Pshdar Ahmed IBRAHIM

Master's Thesis

DEPARTMENT OF PHYSICS

Division of General Physics

JANUARY 2022

FIRAT UNIVERSITY
GRADUATE SCHOOL OF NATURAL AND APPLIED SCIENCES
TURKEY

Department of Physics

Master's Thesis

MAGNETIC AND THERMAL PROPERTIES OF CoFeNi-BASED HIGH ENTROPY ALLOYS

Author
Pshdar Ahmed IBRAHIM

Supervisor
Assoc. Prof. Dr. Canan Aksu CANBAY

JANUARY 2022
ELAZIG

FIRAT UNIVERSITY
GRADUATE SCHOOL OF NATURAL AND APPLIED SCIENCES
TURKEY

Department of Physics

Master's Thesis

Title:	Magnetic and Thermal Properties of CoFeNi-Based High Entropy Alloys
Author:	Pshdar Ahmed IBRAHIM
Submission Date:	13 December 2021
Defense Date:	13 January 2022

THESIS APPROVAL

This thesis, which was prepared according to the thesis writing rules of the Graduate School of Natural and Applied Sciences, Fırat University, was evaluated by the committee members who have signed the following signatures and was unanimously approved after the defense exam made open to the academic audience.

	Signature	
Supervisor:	Assoc. Prof. Dr. Canan Aksu CANBAY Firat University, Faculty of Science	Approved
Chair:	Assoc. Prof. Dr. Ömer GÜLER Munzur University, Faculty of Mechanical and Metal Technologies	Approved
Member:	Prof. Dr. Fahrettin YAKUPHANOĞLU Firat University, Faculty of Science	Approved

This thesis was approved by the Administrative Board of the Graduate School on

..... / ..... / 20 .....

Signature

Prof. Dr. Kürşat Esat ALYAMAÇ
Director of the Graduate School

DECLARATION

I hereby declare that I wrote this Master's Thesis titled “Magnetic and Thermal Properties of CoFeNi-Based High Entropy Alloys” in consistent with the thesis writing guide of the Graduate School of Natural and Applied Sciences, Firat University. I also declare that all information in it is correct, that I acted according to scientific ethics in producing and presenting the findings, cited all the references I used, express all institutions or organizations or persons who supported the thesis financially. I have never used the data and information I provide here in order to get a degree in any way.

13 January 2022

Pshdar Ahmed IBRAHIM

PREFACE

The element additions to FeCoNi-based High entropy alloy were investigated to achieve better magnetic properties. Several analysis techniques were taken, such as EDX-SEM, XRD, VSM, and DTA.

Firstly, I thank Allah for all the opportunities, help, and energies given to me to finish this thesis. Secondly, I am grateful to my supervisor, *Assoc. Prof. Dr. Canan Aksu CANBAY* helped me so much and gave me many opportunities to learn and deal with new categories. She has also guided me on how to do research and always encouraged me to work hard and be an active team worker. Indeed, I learned a lot from her and her experience, which will help me in my future career; I am thankful for all these. Thirdly, my endless thanks to *Assoc. Prof. Dr. Iskender Özkül* for his continued help, and I am proud of what I learned from him. Fourthly, thanks in advance to my lab mates who are *Dr. Oktay Karaduman* and *Dr. Nihan Ünlü,* for their great help and positive energy in finishing my thesis. Fifthly, special thanks to *Mr. Sivar Aziz Baiz* for his unlimited help, motivation, and staying with me when I needed it during the study period.

In addition, I would like to express my great thanks to my parents, my siblings, and all my friends who helped me a lot and supported me in all steps. It was impossible to finish and be successful without their help. They gave me enough positive energy to continue, and their encouragements supported me well.

This thesis was supported by the project number **FF.21.11** by Firat University Scientific Research Projects Coordination Unit (FÜBAP).

Pshdar Ahmed IBRAHIM

ELAZIG, 2022

TABLE OF CONTENTS

Page

ABSTRACT

Magnetic and Thermal Properties of CoFeNi-Based High Entropy Alloys

Pshdar Ahmed IBRAHIM

Master's Thesis

FIRAT UNIVERSITY
Graduate School of Natural and Applied Sciences

Department of Physics

January 2022, Page: xiii + 70

The first generation of High Entropy alloys (HEAs) is that five or more equiatomic components are fabricated together in the range of 5-35 at.% concentration. Recently, the second generation of HEAs was identified as non-equimolar compositions. HEAs have outstanding mechanical properties with excellent magnetic behaviour that may be changed further by adding various alloying elements. This study investigated the influences of adding elements (Ti, Cr, Sn, V, Hf, Ga) on AlCoFeMnNi alloy's structure and magnetic properties. Many different measurements were performed for the alloys, including scanning electron microscope, energy-dispersive X-ray (SEM-EDX) were used to structure analysis, and X-ray diffraction (XRD) was used for crystal structure examinations. Besides, thermal analyses were carried out through differential thermal analysis (DTA). Above all, vibrating sample magnetometry (VSM) is used to verify its applicability in magnetic applications.

In equiatomic AlCoFeMnNi alloy, the highest magnetization value has been seen, which is 141.1 emu/g, while the lowest value (51.2 emu/g) was detected through Hf addition AlCoFeMnNi alloy. The change in magnetic characteristics is due to the phase change related to different element additions. The results obtained through materials analysis have been reported by examining HEAs' structural, thermodynamic, and magnetic aspects. In addition, it is calculated that the tested alloys have a coercivity in the range of 78 Oe to 325 Oe, which means the produced alloys have semi-hard magnetic behaviour. All results should guide how these alloys could be used in magnetic applications.

Keywords: High entropy alloy (HEA), Magnetic effect, Fabrication, Phases, Coercivity, Vibrating sample magnetometry (VSM)

ÖZET

CoFeNi-Esaslı Yüksek Entropili Alaşımlarda Magnetik ve Termal Özellikleri

Pshdar Ahmed IBRAHIM

Yüksek Lisans Tezi

FIRAT ÜNİVERSİTESİ
Fen Bilimleri Enstitüsü

Fizik Anabilim Dalı

Ocak 2022, Sayfa: xiii + 70

Yüksek entropili alaşımların (YEA) ilk nesli, beş veya daha fazla eş atomlu bileşenin %5-35 konsantrasyon aralığında birlikte üretilmesidir. Son zamanlarda, ikinci nesil yüksek entropili alaşımlar, eş molar olmayan bileşimler olarak tanımlandı. Yüksek entropili alaşımlar, çeşitli alaşım elementleri katkılanarak daha da değiştirilebilen mükemmel manyetik davranışa ve olağanüstü mekanik özelliklere sahiptirler. Bu çalışmada, AlCoFeMnNi alaşımının yapısına ve manyetik özelliklerine, katkılanan elementin (Ti, Cr, Sn, V, Hf, Ga) etkileri araştırılmıştır. Alaşımlar için taramalı elektron mikroskobu (SEM), yapı analizi için enerji dağıtıcı X-ışını (SEM-EDX) ve kristal yapı incelemeleri için X-ışını kırınımı (XRD) dâhil olmak üzere birçok farklı ölçüm yapıldı. Ayrıca, diferansiyel termal analiz (DTA) ile termal analizler yapılmıştır. Ayrıca üretilen alaşımların, manyetik uygulamalarda kullanılabilirliğini doğrulamak için VSM analizleri yapıldı.

Eş atomlu AlCoFeMnNi alaşımında en yüksek manyetizasyon değeri 141.1 emu/g ile görülürken, en düşük değer (51.2 emu/g) AlCoFeMnNi alaşımına Hf ilavesi ile tespit edilmiştir. Manyetik özelliklerdeki değişiklik, farklı element ilavelerine ilişkin faz değişikliğinden kaynaklanmaktadır. Malzemelerin analizi ile elde edilen sonuçlar, yüksek entropili alaşımların yapısal, termodinamik ve manyetik yönleri detaylı olarak incelenerek rapor edilmiştir. Ayrıca test edilen alaşımların 78 Oe ile 325 Oe aralığında bir zorlayıcılığa sahip olduğu, yani üretilen alaşımların yarı sert manyetik davranışa sahip olduğu hesaplanmıştır. Tüm sonuçlar, bu alaşımların teknolojik uygulamalarında nasıl kullanılabileceği konusunda bir rehber olmalıdır.

Anahtar Kelimeler: Yüksek entropi alaşımı, Manyetik etki, İmalat, Fazlar, Zorlama, Titreşimli örnek manyetometrisi (VSM)

LIST OF FIGURES

Page

LIST OF TABLES

SYMBOLS AND ABBREVIATIONS

Symbols

R	: Gas constant
Al	: Aluminum
Co	: Cobalt
Fe	: Iron
Mn	: Manganese
Ni	: Nickel
Ti	: Titanium
Cr	: Chromium
Sn	: Tin
V	: Vanadium
Hf	: Hafnium
Ga	: Gallium
Nb	: Niobium
Zr	: Zirconium
Pd	: Palladium
G	: Gibbs free energy
H	: Enthalpy
S	: Entropy
ΔS_{mix}	: Mixing Entropy
ΔH_{mix}	: Mixing Enthalpy
ΔS_{conf}	: Configurational Entropy
K	: Boltzmann constant
δ	: Atomic size change
Ω	: competition between enthalpy and entropy
M_S	: Magnetic saturation
$\vec{H}_0$	: Magnetic field
$\vec{m}$	: Magnetic moment
H_C	: Coercivity
T_m	: Melting temperature

Abbreviations

HEAs	: High Entropy Alloys
HEA	: High Entropy Alloy
HESMAs	: High Entropy Shape Memory Alloys
HEE	: High Entropy Effect
VEC	: Valence Electron Concentration
BCC	: Body-centered cubic
FCC	: Face-centered cubic
HCP	: Hexagonal closed-pack
RSS	: Random Solid Solution
OSS	: Ordered Solid Solution
IM	: Intermetallic
SOP	: Simple Ordered Phase
SDP	: Simple Disordered Phase
CALPHAD	: Calculation of phase diagrams

DFT	: Density functional theory
DTA	: Differential Thermal Analysis
XRD	: X-ray Diffraction
EDX	: Energy Dispersive X-ray
EDS	: Energy Dispersive X-ray Spectroscopy
SEM	: Scanning Electron Microscope
VSM	: Vibrating Sample Magnetometry
AC	: As-cast
HM	: Homogenized
TEM	: Transmission Electron Microscopy
at.%	: Atomic percentage
wt.%	: Weight percentage
TEC	: Thermal Expansion Coefficient

1. INTRODUCTION

The alloying phenomena are identified as adding a minor fraction of one or more elements to the main metal to meet the specific mechanical, physical, and chemical enhancements [1, 2]. In revising the concept of traditional alloy design, all alloys have a metallic base component-oriented [3, 4] due to adjusting their properties based on the leading element with only minor doping to many other elements which form an alloy family [5]. Although to avoid the development of complicated microstructures, the alloy's design has been limited to one or two items that may not be easily processed, analyzed, and adversely affected on mechanical properties [6, 7]. The purpose behind alloying is to get new and different properties and achievements that cannot be found with any single material. For instance, the strength of steel could develop with carbon additions, so the result is that new steel is much harder than iron [8].

Besides, High entropy alloys (HEAs) are all these alloys consisting of different key alloying elements [9] also; in HEAs, the number of components was changed to three or more [10], and these new kinds of alloys give a chance to produce alloys with five items [4, 5, 11-17] and more than 5, in some cases, it may get 13 elements to fabricate one new alloy in HEAs [18]. In conventional alloys, the additions of minor elements to the focused materials are so-called "base composition" to improve their properties, such as NiTi-base or CuAl-base. In these cases, traditional alloys with the method of "base composition" just could make n types of alloys that come from n number of base elements [11]. Whereas several elements could combine to produce HEAs that don't focus on any elements like previous alloys, HEAs consist of some portions that make new novel alloys. With this brand new product of design alloys, a large number of alloys are produced and investigated, and many new phenomena, new features, and new applications can also be found [3, 19]. In the last few years, HEA's metallurgical research group has received significant attention due to its unusual compositions, microstructural and functional properties [9, 15, 16, 20, 21] then; the research of this field is unrestricted [7] as we can notice from Figure 1.1. HEAs have earned a lot of interest and unique properties for their various microstructures and properties [5, 9, 16], like wear resistance [5, 22], corrosion property [10, 23], low-temperature fracture toughness [24], and high-temperature mechanical property [5, 10, 25]. In summary, some unique and unusual features were visible because of their difficulty [5, 9]. HEAs have achieved significant breakthroughs in functional applications, especially soft-magnetic materials [13, 26], films with diffusion barrier [13, 27, 28], materials for Irradiation resistance [29, 30], materials with superconducting [18], materials for photothermal conversion [31].

HEAs are defined as an alloy containing five or more metals in equal atomic or near equal atomic compositions mixed [4, 5, 7, 11-18]. The atomic ratio of each element has to be stated from 5 to 35 atomic percentage [4, 5, 7, 12, 15, 17, 18]. The other description is based on the entropy principle. It describes HEAs as an alloy with a configuration entropy higher than 1.61R, with R as a gas constant [32]. Moreover, HEAs have a new type called the second generation; this is related to non-equimolar portions with a multiphase solid solution [8].

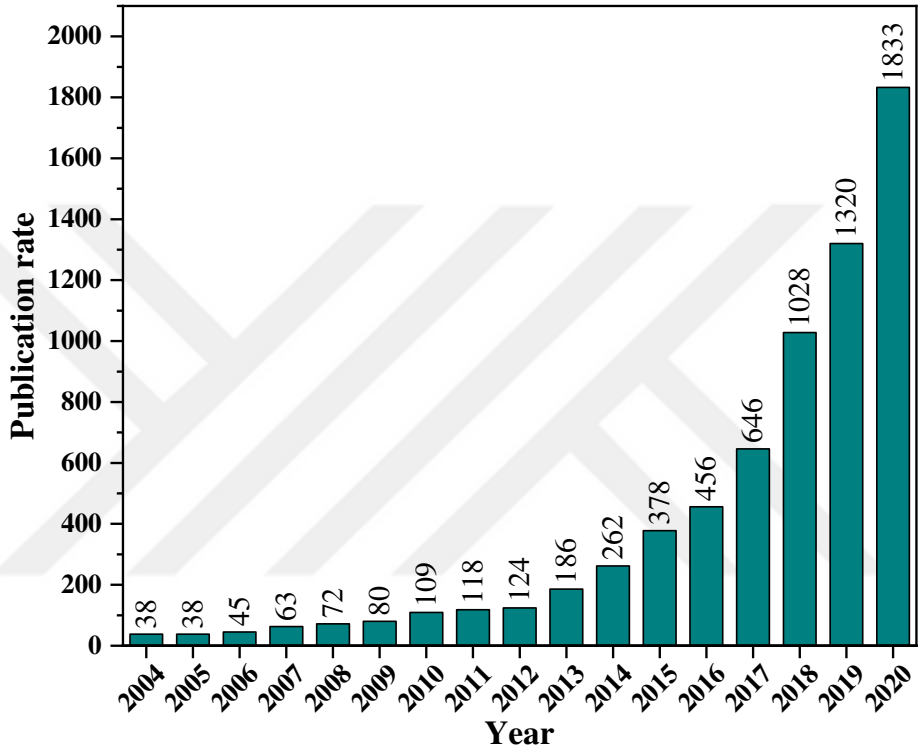

Figure 1.1. Published studies in the field of HEAs since 2004 [21]

HEAs benefit more excellent magnetic properties and improved mechanical properties compared to traditional alloys [33, 34]. While searching for suitable components, it is remarkable that alloys containing Al and Mn have excellent magnetic characteristics and are cost-effective [35, 36]. Besides, the appropriate range and proportion of Fe, Co, and Ni components and the addition of various elements into HEA should offer ferromagnetism and other magnet abilities [6]. The magnetic characteristics of a ferromagnetic alloy could be significantly changed by as little as a few impurities. Additionally, M_s value is highlighted due to its great reliance on alloying elements and the HEA's crystal structure [34, 37]. Zuo et al. [38] reported that the M_s value should be enhanced from 18.14 to 148.7 emu/g with Al addition, decreasing the antiferromagnetic ordering of Mn atoms in FeNiCoMn as well.

Furthermore, Mishra et al. [39] advised that the Al additions for Mn contain HEAs to improve magnetic properties. As a result, the Al doping to the CoFeMnNi alloy can enhance magnetic saturation remarkably. Based on that result, Hariharan et al. studied the effect of Al additions in different compositions on the magnetic properties of CoFeMnNi alloy [40]. They stated that the magnetic saturation could be improved through the BCC phase in equiatomic or near-equiatomic alloys. As a result, by reducing the brittle intermetallic phase, a homogenized AlCoFeMnNi alloy with excellent ferromagnetic characteristics was considered suitable for soft magnetic purposes. Soft magnetic materials are employed in transformer cores and signals like controllers and transducers due to their high magnetic saturation (M_s) and low coercivity (H_c) [41]. Thus, there are still numerous opportunities to research to improve magnetic saturation for use in various magnetic applications.

In this research, the AlCoFeMnNi in equiatomic composition with another six alloys were fabricated in an arc melting furnace. Then, the influence of element additions (Ti, Cr, Sn, V, Hf, and Ga) on the magnetic characteristics and microstructure of AlCoFeMnNi equiatomic alloy have been examined. Structure analysis was carried out through the scanning electron microscope, energy-dispersive X-ray (SEM-EDX), and X-ray diffraction (XRD) was used for crystal structure tests. To determine their magnetic usefulness, the vibrating sample magnetometry (VSM) were carried out. Furthermore, differential thermal analysis (DTA) was used to make thermal analyses. The purpose of this research is to improve the microstructure and magnetic properties of a homogenized alloy (AlCoFeMnNi) by doping different elements. Meanwhile, there is some research on that alloy, but they didn't study the effect of element additions on that base alloy (AlCoFeMnNi).

2. LITERATURE REVIEW

Some topics have been highlighted in this chapter, clarifying several concepts in the theoretical background that refers to literature. It starts with a short history of HEAs; then it includes some basic concepts in HEAs, core effects, Valence electron concentration (VEC), crystal structure and phase formations, HEAs' properties, and instruments used in that thesis work have also been mentioned.

2.1. A brief History of HEAs

Developing materials have a significant role in the progress of human society. The age of metals has located between the Bronze-Iron age and longer than fifty centuries. Humanity's necessaries are still remarkable in the last 150 years, which has been easy to notice the developments of most high-performance metals. As compared to the whole metal age, that isn't a long period [3]. When considering alloys, not from one or two "basis" elements but several elements entirely from the conventional box and design, this new creation was first fabricated by Yeh et al. [3]. Figure 2.1 which is a historical literature diagram explaining this history between years and materials. In Taiwan, Tsinghua University had a master's project supervised by prof. Yeh, in 1995, was the first to study the main basic phenomena dealing with multi-element alloys [42].

In the early 21st century, the entropy principle started, and then the HEAs phenomena were widely used [4, 12]. In spring 2004, Yeh and his co-workers had a first work related to the HEAs concept by showing results from experimental data and related theories. The article was published in the "*Advanced Engineering materials*" journal titled "*Nanostructured high entropy alloys with multiple principal elements: novel alloy design concepts and outcomes*" [43]. Also, in February 2004, in the same mentioned journal, another research was published under the name "*Multi-principal-element alloys with improved oxidation and wear resistance for thermal spray coating*" [44]. Still, the HEAs term wasn't mentioned in that paper.

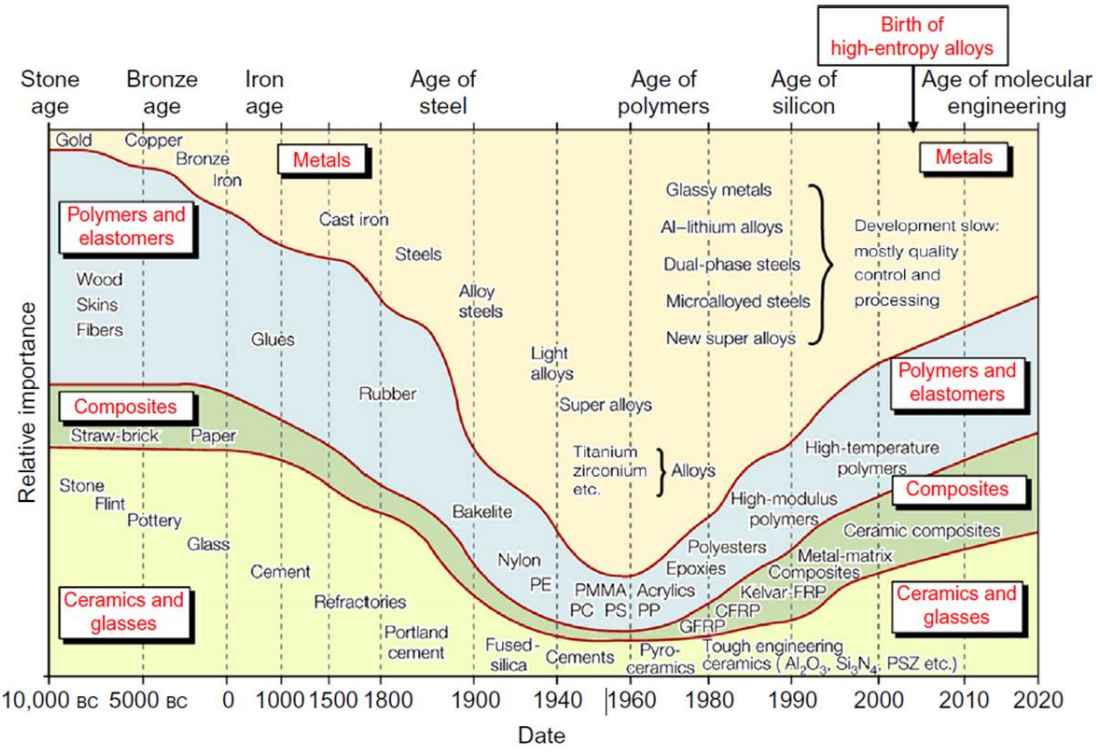

Figure 2.1. Some materials in an explanation of historical diagram [6]

The expression of High entropy alloys used by Yeh et al. [5, 6, 12, 15] and Cantor et al. used multi-component alloys [15, 20]. Both of these two refer to the same concept. Other names were also used like multi-principal elements, alloys with multi-component alloy, equimolar-alloy, substitute alloy, and equiatomic-ratio alloys [15].

In 2015, Firstov et al. published an article entitled "*High entropy Shape memory alloys*". Its variety of opportunities to work more with HEAs and Shape memory alloys under the new criteria: High entropy Shape memory alloys (HESMAs). This new way to make alloys make some unique and have different applications in smart materials [45]. After all these, in this master project the magnetic properties of CoFeNi-based HEAs were studied, and the results are shown in the following chapters.

2.2. High Entropy Alloys

In the last century, when alloying metals became a fascinating topic in the science community, these conventional alloys were produced with one base element mixed with minor portions of the second element. These works focused on the properties of base metal elements [19]. The discovery in multi-component random solid solution (RSS) formation equiatomic alloy was stated differently by Yeh et al. [12] and Cantor et al. [46]. HEAs apply widely to multi-based solid-solution alloys, owing to high configuration entropy. Compared to typical alloys typically centred

on this side of the phase diagram, these compositions are located near the centre of a multi-component phase diagram [47]. Yeh et al. explained that the formation of the RSS may be due to a high structure entropy in these multi-component equiatomic alloys, thus coining the term "high-entropy alloy" (HEA) [19]. These new types of alloys are so-called “HEAs” because of their higher entropy of mixing compared to traditional alloys in their states of RSS or liquid [5, 7]. The expression of HEAs was applied since these alloys were wondered to have ideal solutions [11]. Although the name of HEA and the high entropy mixing of HEA results in the primary explanation for the control is mixing entropy, there is no good evidence to support this justifier for the existence of SS-phases [48]. Contrary to these hypotheses, however, experiments show that the greater mixing entropy in these alloys encourages the formation of SS-phases in simple structures, which leads to decreases in the various phases [5].

The mixing configuration-entropy of the mixing alloys should be a multi-component phase diagram in the middle and approach its limit for a solution phase [15]. The thermodynamic equilibrium method aims to calculate the stability of the Gibbs-free energy process for different phases, which possibly occur in that HEA [11]. If enthalpy is H and entropy is S, a scheme can minimize its Gibbs free energy G=H-TS by a thermodynamic [18]. One of the definitions of HEAs refers to the entropy concept, and it states that the configurational mixing entropy has to be greater than 1.6R ($\Delta S_{mix} \geq \ln\ (5)\ R = 1.6\ R$) in their RSS where R represents the gas constant [8]. As shown in Figure 2.2 sketched region limits in mixing entropy, as we can see from these figures when it’s just one material then the theoretical value of entropy is close to zero and it names Ultrapure materials. Although, when it’s containing one or two elements then $\Delta S_{conf} \leq 0.69\ R$ and it is called low entropy alloys. Medium entropy alloys are these alloys that have 2 to 4 materials in the range of $0.69 \leq \Delta S_{conf} \leq 1.61\ R$. Wherever five elements or more are combined to make an alloy, then the result of configurational entropy would be $\Delta S_{conf} \geq 1.61\ R$ and it is termed high entropy alloys. For the case of HEA, the addition of an extra composition could improve mixing entropy and favor the formation of a solid solution phase rather than precipitating intermetallic phases [39]. To summarize what is mentioned here, the equiatomic percentage alloys have variable configurational entropies, as seen in Table 2.1. The mixing of the compositions creates a value of $\Delta G_{mix} = \Delta H_{mix} - T\ \Delta S_{mix}$ in a method of multicomponent alloys. Boltzmann's theory indicates that the configurational entropy of mixing of an ideal gas with r elements [18]. The entropy of configuration for each mole could determine with $\mathrm{R}\ln n$ from (2.1 or (2.2), it also deals with the relation of complexion and entropy of a system based on Boltzmann’s hypothesis [7]:

$$\Delta S_{conf} = -k \ln w = -R\left(\frac{1}{n}\ln\frac{1}{n} + \frac{1}{n}\ln\frac{1}{n} + \cdots \frac{1}{n}\ln\frac{1}{n}\right) \qquad (2.1)$$

$$\Delta S_{conf} = -R \sum_{i=1}^{n} X_i \ln X_i \qquad (2.2)$$

where the gas constant is R= 8.314 J/K mol and n is the number of elements [6, 7] if k represents a Boltzmann constant and w is the number of ways that the energy available can be combined or exchanged between the system's particles.

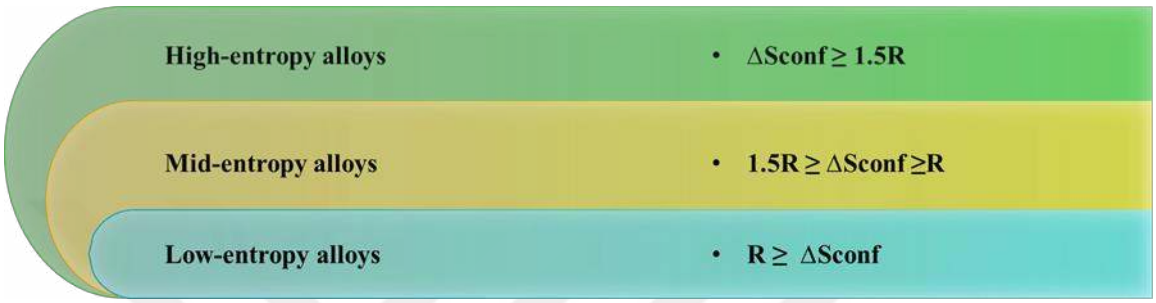

Figure 2.2. Limits in alloys word with the entropy of mixing [4, 6, 7]

Generally, an alloy with HEA items is made such as Cr, Fe, M, V, which categorized as BCC-type, elements like Al, Cu, Ni related to FCC-type, and HCP-type includes Co, Ti [49]. The highly mixing entropy can maintain unordered SS phases of simple structures, like a face-centred cubic (FCC) or a body-centred cubic (BCC), compared to ordered crystalline intermetallic phases mostly involving large unit cells that are structurally complex [18, 50]. Therefore, certain phases such as BCC, FCC, mixed BCC and FCC were possibly found in the resulting crystalline phases [48, 49].

Beside all these, so many articles detected that ΔH_{mix} play like a critical parameter to determine crystal structure. HEAs with a too positive or too negative value of ΔH_{mix} are expected to lead to phase segregations and thus contribute to multi-phase alloys [16, 17, 51]. Thermodynamic analysis for multielement alloys suggests that non-configurational entropy and enthalpy play a key role in the stability of phases. Still, when only a single phase is noticed, just entropy of configuration plays a critical role [2]. At fewer temperatures, phase stabilizations are decreased due to entropy [18].

Table 2.1. ΔS_{conf} of equiatomic alloys [32]

n	**1**	**2**	**3**	**4**	**5**	**6**	**7**	**8**	**9**	**10**	**11**	**12**	**13**
ΔS_{conf} (R)	0	0.069	1.1	1.39	1.61	1.79	1.95	2.08	2.2	2.3	2.4	2.49	2.57

Furthermore, the task of HEA selection certainly will significantly help in better understanding and knowledge of exotic systems, step creation, and the ability to predict complex microstructures in our multi-component systems [9]. There are many probable HEAs, and it would be difficult to search for valuable alloys by examining any alloy composition by a trial and error method [11, 15, 52]. The most challenging phase diagram is often created when an alloy consists of more components. In such cases, aside from theoretical modelling [11, 49, 53, 54], Computer approaches including density theory calculations (DFT) [11, 55] were also used. HEA simulations are used to analyze the development of phases [11]. Quantification of the HEA entropy source is the central topic in the fundamental understanding of HEA creation [15]. The most common example of a unique HEA activity is probably CrMnFeCoNi. The problem was that Cr-Mn-Fe-Co-Ni is not thermodynamically stable at all temperatures as a single phase. While this could be heat treated as a single solid solution for FCC, it displays several noticeable properties in this condition when tested [9].

Rather than considering dislocations in a matrix to be blocked by separate solute atoms, it was suggested that they might be seen as moving through an effective medium in which an average impact generates resistance. Because of this, Wu et al. [56] reported that the influence of temperature on the dislocation range was explained by the yield model behaviour in CrMnFeCoNi, that is, thermal activation.

2.3. Core Effects

The multi-component principal character of HEAs is responsible for various main effects that are less apparent in conventional alloys and can be termed as 'four core effects' [5]. In addition, the equimolar amount of each element in HEAs compositions isn’t as simple as traditional alloys [15]. The following section will give some descriptions and introductions of the core effects.

2.3.1. High Entropy Effect

The most apparent core effect is the high-entropy effect (HEE) which gives the title to alloys [57]. Commonly HEE is being used to explain the solid solutions for multi-component compositions [15]. HEE is the critical concept of the HEA. It shows that high configurational entropy in near-equimolar alloys with five or more elements will favour single-phase rather than intermetallic (IM) compounds [58]. As indicated in the title, high entropy could improve the formation of SS phases by providing unique and most powerful HEAs [7]. However, HEE increases the entropy of higher mixing in HEA declines the free energy of solid solution phases [5], and the microstructure was simpler than first thought [5, 7], especially when the temperature is high [5].

This could be found that three potential types of competition phases are present in the solid-state of an alloy, notably intermetallic compounds, primary phases, and solid-solution phases, as well as competition in solidifying the liquid phase [7]. In solid solution phases, the entropy in traditional alloys is more remarkable (including terminal and intermediate solid solutions) than in IM compounds [5]. Based on the theory of "maximum entropy production principle (MEPP)" [59], besides IM phases, high entropy offers to keep stable in phases of high entropy like the SS phase. On the other hand, low entropy configuration forms the phase of IM [15]. Therefore, there have only been two major phases. In these phases, clear structures such as BCC and FCC contradict common simple structure expectations: developing various forms of binary/ternary compounds [5, 7, 15, 60], as can be seen from Figure 2.3.

Moreover, the number of steps in HEAs may be reduced based on the increased mutual solubility between elements [4, 5, 15, 60]. Entropy can maintain a mechanism with enhanced entropy based on the free energy equation of Gibbs since the temperature is high enough [5]. HEAs at high temperatures, the solid solution phases incredibly possible to achieve phase stability [5, 7]. According to Richard's rule, the entropy difference at the melting point in the two states is almost equivalent to R (gas constant) [61]. Dependent on the second thermodynamic law, the equilibrium condition of all points shall be the lowest free mixing energy ΔG_{mix} [7].

In summary, to prevent the development and understanding of several different types of stoichiometric compounds, an HEE is required for HEAs. On the contrary, it improves the production of phases of solution type and consequently reduces the phase rate as predicted by Gibbs, enabling the number of phases of balance to expand with the count of parts [7].

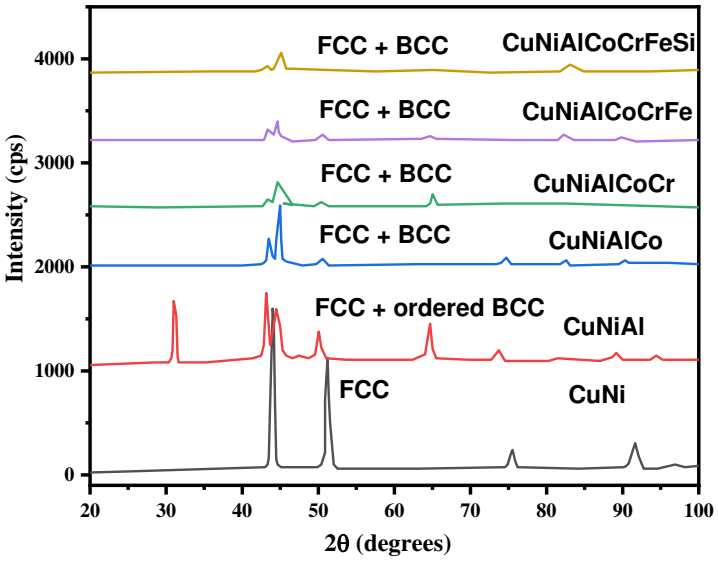

Figure 2.3. XRD patterns of a serial alloy constructed by doping one additional element to the previous one sequentially. One or two main phases are detected in all alloys which have a simple structure [4-6]

2.3.2. Sluggish Diffusion Effect

HEAs' kinetic process and propagation have been slower than conventional alloys [5, 62]. Two main points can be explained. At first, HEA and its neighbours before and after an atom leap into a position, therefore, differ in a kind of distinguishing atom on each lattice field [5]. The separation of atomic structures at each site results in separate coupling and thus separate energy of regions. On the other hand, the atom is more likely to return to its original environment when the location is a high-energy spot. The diffusion mechanism can minimize any such cases. Thus, the regional atomic structure in traditional alloys with low solvent concentration could be seen to be mostly the same before and after being vacated [5].

The phase transformations based on atomic diffusion contain cooperative elements, which restrict the efficient diffusion rate in HEA combined with the lattice distortion, which hinders atomic motion, to achieve a split balance among the phases [4, 12, 63, 64]. HEA components have a varying rate of diffusion, as some components are not as involved as others (high-melting-point components are the great examples for it), therefore, these components have lower output values as they compete in vacancies with some other components, and the slow-moving components are the factor which adversely affects change in these scenarios [5]. The third consequence of the RSS presented by Yeh is the reduction of diffusion kinetics in HEAs. Due to the potential fluctuations in a local lattice caused by different constituent sections of the RSS, Yeh defines atomic diffusion in HEA as “sluggish” [57]. However, apart from direct diffusiveness tests, several experimental proofs prove that atomic motion is not very slow in HEAs [9].

Tsai et al. [5, 65], a seven-bond model was used to quantify the effects of the diffusion of local energy variations. Two reports recording diffusion coefficients can test this slow diffusion [65, 66]. Tsai has conducted the first research on HEAs diffusion ratios, whereby a 'quasi-binary diffusion pair' was added to the self-diffusion ratio of device components of CrCoMnNiFe alloy [65]. Tsai combined the conclusions with austenitic steels and pure metal systems and found that the rate of self-diffusion in HEA for any element in HEA is also weakest. Vaidya's research on the diffusion of Ni-bullets in CrCoNiFe and CrCoMnNiFe were conducted, and conclusions were compared to other FCC systems. The slightest diffusion of Ni in comparisons with the inverse homologous temperature was observed for a more significant entropy configuration [57, 66]. Since some studies have found that HEA diffusion is slower, the relative reduction is not very high [57]. Disrupted energy in lattice sites faced with species diffusion, Figure 2.4 states that the distance between atomic locations is considered to have been fixed.

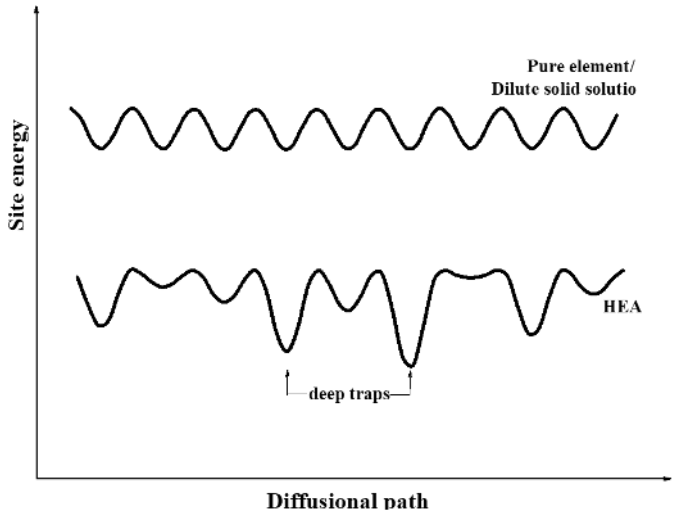

Figure 2.4. Schemas demonstrate the complete variation in the lattice potential energy profile in a pure element or dilute solid solution (top) along an atomic diffusion path and in a lattice of HEA (bottom) [9, 57]

As can be seen in several published literature, the slow diffusion effect can offer several significant benefits [64, 67, 68]: supersaturated stage and fine precipitates easily obtainable, rising recrystallization temperatures, increased crumb resistance, slower grain growth, and lower particles coarsening rate. These benefits to greater efficiency can be used through microstructure and property controlling [7]. The ability to shape nanocrystalline or amorphous structures could be used to promote the mechanic, chemical, and physical properties of these alloys [4, 69].

2.3.3. Severe-Lattice Distortion Effect

There are several types of components in HEAs, each of which has different dimensions. These size differences eventually help to distort the lattice and to drive their inhabitants far enough with larger atoms, and there is additional space for tiny atoms around them. The stress-energy of the lattice associated with distortions increases the overall free energy of the HEA lattice [4, 5]. In complex condensed phases, the atoms that shape crystal lattices cause extreme lattice distortions [58]. The movement depends on the atom and types of atoms for each location in the region. These distortions have proven more significant than in conventional alloys [58]. Apart from the variable atomic size, the propensity of a separate energization and the crystal structure between constituent objects is thought to be much greater in lattice distortion, provided that there are no symmetric relationships with the atom and the neighbouring electronic structures [7, 70]. Additionally, the extent of lattice distortion is much greater than in conventional, which are centred a remarkable piece and many solvent atoms which have the same atomic structure as their competitors in conventional alloys [7].

It affects the mechanical, electrical, thermal, optics, and chemical behaviour of materials through distortion in crystalline or amorphous structures, which are named "lattice distortion effects" [4]. Instability of the atomic location with extra configurational entropy from these distortions results in the structure. The strength of X-ray diffraction peaks decreases [4, 58, 71], the conductivity of heat and electricity drops [4, 5, 58, 72] to hardness improving [4, 58], and the properties do not depend on temperature that much [4, 58]. In HEAs, many such properties are susceptible to temperatures since the distortion of the lattice induced by the thermal vibration of atoms is relatively modest compared to the lattice distortion caused by the severe distortion [7, 70].

Although high-resolution TEM (HRTEM) images have been proposed to display distortion in lattice [9, 73], the slight distortions of long-range are not consistent with the localized strain by Yeh et al. because faults like dislocation occur [64, 71, 74]. Furthermore, as the idea of a typical crystal structure in HEAs is normal for solid solution phases with multi-principal components, one or two elements become a multi-element basis [4].

2.3.4. Cocktail Effect

It was used to describe the ability to concentrate on only the speaker by combining conversations with external noise and saving it from discussions. In metal alloy, the impact implies that unpredictable properties can still be achieved after mixing many elements that cannot be obtained from any single product [15]. The first work about cocktail effects has done by Ranganathan [15, 75]. Unlike the other 'core effects', the cocktail effect is not expected. It doesn't have to prove, and cocktail effects make us realize that uncommon materials are often characterized by unexpected abilities [58].

Moreover, a cocktail effect also drastically affects alloy properties by the composition and alloy changes [15]. HEA characteristics refer to their including elements; for example, the alloy density reduces with additions of light elements. However, it is essential to consider the relationship between component-element even concerning the properties of the individual component elements. However, adding a soft element that is also a low melting point element (e.g. Al) shall tough the HEA [4, 5]. HEAs can also be used as a composite at an atomic scale since combined multi-key elements. As a result, in addition to the implied effects on the microstructure, the various components have a cumulative impact from their fundamental characteristics and relationships [12, 63, 75-77]. The oxidation resistance may also be improved at high temperatures if additional elements like Si, Al, and Cr are used. It would enhance strength if an element such as Al were added, which is strongly connected and develops a BCC-phase with elements such as Co, Cu, Ni, Cr and Fe [4, 57]. In all kinds of alloys, the properties depend entirely on microstructure and portion of including elements. Perhaps, it is best to use this term concerning the unusual and exotic features

in HEA because of its complex compositions. It can also be argued that this effect should be ignored [9].

2.4. Valence Electron Concentration

All above thermodynamic principles are helpful guidelines in selecting stages in HEAs and then whether they produce single or multiple phases. Though, for detecting phases like FCC, BCC, and HCP made in HEAs, a rule or a parameter was needed [11]. Valence electron concentration (VEC) became a significant parameter that affects solid solution phases when the atomic size is lacking; this is all stated by Hume–Rothery rule [11, 49, 78]. The crystalline lattice types could be predicted by VEC, guided by the Hume-Rothery rule. Furthermore, the single-phase BCC structure could detect when the value of VEC is less than 6.87; also, both FCC and BCC phases have existed when the condition $6.87 \leq \text{VEC} \leq 8$ verified, and if the VEC gets over from 8, then the phase would become FCC phase [49, 79, 80]. "*The smaller the VEC, the higher the BCC-phase volume fraction is*" [49]. If VEC is high, it leads to the greater power of atomic bonding such atoms tend to comply with a higher atomic packaging density in FCC structure. When the value of VEC is low whereas, the atomic bonding potential is lower when these atoms are arranged in a low atomic packaging density as marked in BCC structure; typically, a low VEC number will grow a material's strength. In contrast, a high VEC value will increase a material's ductility [80]. VEC is represented mainly in a symbol like e/a; it could also use it instead of VEC when dealing with phase structure. Guo defined that variable. & Liu. [49] and Guo et al. [48] to be beneficial to wonder phase formations in HEAs. As a result, the BCC phase would be stable in low VEC regions, and FCC phases remarkably when VEC is high [80]. To evaluate the value of VEC, the following equations (2.3 or(2.4) should be used [49, 80]:

$$e/a = \sum_{i=1}^{n} c_i \, (e/a)_i \tag{2.3}$$

or

$$VEC = \sum_{i=1}^{n} c_i \, (VEC)_i \tag{2.4}$$

where c_i is the percentage of atoms for each element $(VEC)_i$ & $(e/a)_i$ are the VEC and e/a.

On the other hand, some researchers mentioned various scientific ways and strategies to predict phases in HEAs, such as melting points T_m and atomic size difference ∂ [81], ΔH_{mix} which is the mixing enthalpy [82], ΔS_{mix} is the mixing of entropy [12, 15], VEC which is valence electron concentration [48, 49, 80]. Above all, the greatest variable to predict the formations in HEAs of

sole-solid-solutions is ΔH_{mix} (formation of compounds does not occur). ΔH_{mix} could form solid solution in the range ($-5\ KJ\ /mol \leq \Delta H_{mix} \leq 5\ KJ\ /mol$), compounds perhaps noticeable when ΔH_{mix} is more negative [49].

2.5. Crystal Structures and Phase Formations

The phases in HEAs have commonly been very different in previous studies. They categorized as ordered solid solution OSS (e.g. B2 and L12), intermetallic phases (e.g. Laves phases), and random solid solution RSS (e.g. FCC, BCC), it can be listed as RSS, OSS, and intermetallic phases [5]. That topic could cause some doubts. Intermetallic phases should be described as OSSs; they often have composition sizes and are ordered by default. In this regard, we regard classifications of the phases based on their structure arrangement (simple or complex) and (ordered or unordered).

2.5.1. Simple-Solid-Solution Phases in HEAs

Simple structures (simple ordered phase SOP and simple disordered phase SDP) are the most frequently found in as-cast (AC) HEAs, which made scientists surprised [5]. Besides simple phases, various phrases like (σ, μ, Laves, etc.) under the name complicated organized phase COPs are also found in HEAs [5]. Factors affecting the production of solid binary solutions again under classical Hume Rothery rules differ in the concentration of electrons, atomic size, and electronegativity [83]. Besides all these parameters, both enthalpy and entropy of merging are the most relevant variables to phase formations in HEAs. Guo and his colleagues [48] and Zhang with his co-workers [84] promoted the role of these two parameters in phase formations, and they conclude that changes in atomic size (δ), mixing of enthalpy (H_{mix}) and mixing of entropy (S_{mix}) are mostly effect on the creation of simple or complex phases. Some points are remarkable such as the sizeable positive value of H_{mix} causes separation of phases, it had better do not have a considerable value of H_{mix}, mostly intermetallic phases occur when the value of H_{mix} is highly negative. The δ must be small enough because when δ is high, it helps destabilize simple structures and strain energy. Also the great amount of S_{mix} is required in order to form simple phases because it has been a key element for that formation [84].

The phases macroscopically found in as-cast HEAs can involve atomic irregularities. It could be proved by atomic probe test and transmission electron microscopy (TEM) [85]. In HEAs, there are also similar disordered models of the same base structure [86]. BCC coexistence and regulated phases BCC (B2) are frequently reported as a background [87]. It is significant that the phases FCC and ordered FCC (L12) exist, and the peaks of XRD correspond with the virtually identical parameters of these phases [86].

As a consequence, if the SOP sum is not high, XRD can only show the SDP peaks while the SOP would appear [86, 87]. As a result, it shows that TEM is an important tool to present SOP [86, 87]. CoCrFeNi alloy has a phase of FCC solid solution. When the Al ratio changes between 0 to 2 in $Al_xCoCrFeNi$, the phases from FCC and mixture of FCC and BCC turns to BCC single phase [88]. Although his HCP phase is often defined as a standard HEA structure with simple solid solutions that cause have much attention. Tsau has observed the solid solution phase of HCP in the TiCrZrNb alloy, but the phase of HCP did not occur on its own, but it was in an interphase zone [89]. Also, GdHoLaTbY as-cast alloy has the HCP phase, which was discovered by Qiao et al. [90].

2.5.2. Phases at Enhanced Temperatures

As explained in the previous section, our information about the HEA phases mainly caught on their as-cast condition. However, thermodynamic equilibrium is generally not in the caste situation [5]. Therefore, phase transition will be less meaningful to alloys located in the BCC/FCC phase area described by Guo et al. [91]. For example, no phase formations had been seen during its high-temperature annealing through Co-Cr-Fe-Mn-Ni FCC alloys [92]. In the meantime, the phase transition will occur in the FCC+BCC phase at higher temperatures between alloys [5]. Annealing with or under ~800 ^{0}C increases the portion of the BCC cycle in the Al-Co-Cr-Cu-Fe-Ni model [93]. The ratio of the FCC phase rises when the temperature is higher than 800 ^{0}C, and it causes annealing. The FCC phase, being ductile, and the BCC phase incredibly unstable and can be adjusted to mechanical properties by annealing [5].

2.5.3. Simulations to Phase Predictions (Phase predictions with Computer programing)

All such new HEAs have many potential opportunities to combine and create unique compositions. However, studying all kinds of that new alloy composition means testing all these new samples in different situations, and it needs a big budget and too much time. Simulations are a fantastic tool to predict future results in any project; it's the best way to save both money and time. To understand more about alloys, phase diagrams are the key to it. Furthermore, simulations should help researchers see phase diagrams, and then the wok needs shrink due to having that theoretical knowledge, just some exceptions to prove some ideas and concepts.

The calculated phase diagram model (CALPHAD) is the most known method which deals with phase equilibrium [94]. In higher-level structures, detecting a problem from CALPHAD with HEAs improvement is to examine the phase equilibrium. This depends on a thermodynamic database for phase diagrams, with some results from experiments [57, 95]. Skenov tried to predict possible compositions; for analyzing and testing 130000 alloys, he got help from CALPHAD [96]. Senkov [96] stated that the validity parameters based on the fraction of the available binary and

ternary areas were selected to determine potential error caused by measuring the compositional zone within the target range for a data set. Planned compositions with CALPHAD studies have to be observed from experiments. Zhang et al. [95] developed the thermodynamic database for alloys includes Co-Fe-Cr-Al-Ni, which forms increasing structures (binary and ternary) to a greater scale of compositions. By using a Ni-based dataset, the divisions of phases and phase nature could be predicted in some alloys like $Al_{23}Co_{15}Cr_{23}Cu_8Fe_{15}Ni_{16}$, $Al_8Co_{17}Cr_{17}Cu_8Fe_{17}Ni_{33}$ and $Al_{0.5}CoCrCuFeNi$ [97]. The theoretical approaches and experimental data would match some exceptions in some deviations [97]. Thus, the idea of studying HEAs with that simulation programs is supported by these mentioned works.

2.6. Properties of High Entropy Alloys

In this section, the properties of HEAs have been clarified, which is shows the importance of that new field of alloying elements. The properties listed are mechanical, electrical, thermal, and corrosion properties.

2.6.1. Mechanical Properties

Mechanical properties deal with so many categories like elongation, ultimate strength, hardness, elastic modulus, elongation, fatigue, creep, and yield strength. These properties provide structural applications with practical combinations [6]. As a comparison between conventional alloys and this kind of novel new alloys, which are HEAs, studies on the mechanical properties of HEAs are more significant. It leads to having the ability for these new alloys to have better different applications. Mechanical properties focused mainly on microstructure and compositions, including elastic properties that specify the interaction of atoms and the behaviour of dislocations. Also, the element proportion defines current phases and their fractions of scale, which influence phase properties by their inherent properties. And then, the mechanical characteristics of materials are greatly influenced by microstructural elements. Atomic defects and pores, cracks, chemical segregation, and residual stress are vacancies, dislocalizations, and grain boundaries that involve macroscopic or microscopic faults. These must be discussed to be more common and better understand mechanical properties [58]. Scientists have to care about microstructures to examine mechanical properties with mechanical characterizations. Thermal or thermo-mechanical treatment in general through thermal treatment results in a stronger balance of strength and ductility both in materials [58].

A mixture of atomic components forms secondary phases and contributes to precipitation reinforcement. For example, the highest hardness (566 HV) was achieved in ten systems investigated by Li. Et al. with Zr & Ti doping, which have a larger atomic size and precipitation of

secondary phases [6]. In $AlCoCrFeNb_xNi$ alloy, the Nb additions in range $X = 0 - 0.5$ cause the change in hardness from 500 to 750 HV, this work was developed by Ma and Zhang. In 2013, Razuan et al. worked on adding Ti & Nb together in these alloys; as a result, the hardness gets a more extensive value which is 797 HV, which is more significant than when only one of two elements is dopped [6].

A microstructural and mechanism methodology-based design is the choice for the systemic compositional analysis of existing HEAs. Conventional load-bearing materials like steel and aluminium alloy use specific reinforcing techniques, depending on temperature and intensity of stress-strain [98]. Moreover, a variable number of articles and researches could be found about mechanical properties since it has been a debatable category, and this was a brief knowledge about it. More details can be achieved elsewhere [5, 6, 15, 58, 99].

2.6.2. Magnetic Properties

Researches into the magnetic properties of HEAs are mainly based on alloys produced with Cr-Co-Fe-Cu-Al-Ni-Ti elements [100-103]. Fe, Co, and Ni are the main composition of ferromagnetism in fabricating an alloy. These elements' required range and amount, and adding different items into HEA could provide ferromagnetism and other magnet properties [6]. In more detail, in general, more than 50 per cent of the magnetic elements (Co, Fe, Ni) exist; either they are just paramagnetic [100, 103] or ferromagnetic with a magnetic saturation (M_s) Perhaps between 10-50 emu/g counted [72].

Furthermore, alloy elements might have a significant influence. Such as, magnetization significantly reduces when Cr is added [102]. That action is explained by Zhang et al. [102] as the magnetic moment of Cr is anti-parallel to Fe, Co, Ni, which helps cancel magnetization. Furthermore, combining various constituents with the Co-Cr-Fe-Ni alloy leads to different phases and structures, contributing to other magnetic behaviours.

The addition of the Cu element only aids in producing the Cu-rich interdendritic phase. It has no significant effect on the solid-solution of the CoCrFeNi FCC phase. As a result, the paramagnetic CoCrFeNiCu alloy exists [72, 104]. In the case of Al doping to CoCrFeNi alloy, the sole FCC phase structure turns to phases of BCC+B2 [72, 100, 105]. The two phases have virtually identical lattice characteristics but extremely different ratios. In these alloys, which are rich in metals (Fe, Co, Cr), the BCC phase appears, whereas if the compound had (Al, Ni) components, the B2 phase occurred [105]. In these alloys, the ferromagnetism base is defined as the BCC phase. The grade of spino-decomposition with a higher decomposition rate contributes to higher magnetization and coercivity and a remanent saturation [72, 105]. Also, if the addition of Pd to Co-Cr-Fe-Ni alloy does not impact the crystal structure processes of the sample, but it would be ferromagnetic [103]. In addition, alloy ($FeCoNiAl_{0.2}Si_{0.2}$) is very bombinated to make it a probable

soft-magnetic material, with a high M_S, strong malleability, and a strong resistivity in available HEAs [102]. Additionally, when the Al and Si increased, M_S decreased considerably [72].

In the progress of researching alloys for magnetic purposes, FeNiCuMnTiSnx alloy series were investigated [101]. If x were zero, the alloy would be in separate intermetallic phases like Fe-Ti Ni-Ti, etc., and it is paramagnetic. On the other hand, the alloy includes two phases concerning the structure of Cu_3Sn and $TiNi_2Sn$ respectively when x=1, so the atomic-magnetic moment of prospective zinc blende structures is calculated with the density-functional-theory (DFT) [101]. Zhang and Ma in 2012 [6] determined that the increasing of Nb portion to $AlCoCrFeNb_xNi$ affect saturation+residual magnetizations negatively while it shows ferromagnetic properties. Adding Pd could increase the Curie temperature and magnet moment in the FCC phase. They discovered that changing the curie temperature with Pd doping makes these alloys advantageous almost at room temperature for magnetically cooled applications [6].

2.6.3. Electrical Properties

In 2009, Chou et al. started studying about electrical resistivity of HEAs. In experimental work, the portion of Al increased from 0 to 2 in $Al_xCoCrFeNi$ alloys. The examinations were focused on Al's influence since Al has a strong BCC and larger atomic size [6]. Resistivity changes were detected in $Al_xCoCrFeNi$ alloy as a function of temperature [6, 100]. As cast HEAs, electrical resistivity is typically offered 100 to 220 μΩ per cm [106]. As in traditional alloys could be noticed, the resistivity value of $Al_xCoCrFeNi$ alloys should increase with temperature rises. Since the slope of the graph between temperature and resistivity becomes temperature coefficient resistivity (TCR), this is generally less than previous alloys one order of magnitude [72, 100]. The level of resistivity at near-absolute zero temperatures compared to (1100 μΩ/cm) in conventional alloys and extreme lattice distortions can be caused by the high level of resistivity of electricity [6]. Electric conductivity decreases with increased x in single-phase regions and is lower in the duplex phase zone. This can be explained and when the interface between the FCC&BCC phases causes the scatter of electrons to decrease, following the theory that greater quantities of Al induce extremely grid distortion and scattering of electrons. The BCC-phase is more conductive compared to phase of FCC in comparison [6].

2.6.4. Thermal Properties

Several researchers have been working on alloys like $Al_xCoCrFeNi$ and $Al_xCrFe_{1.5}MnNi_{0.5}Mo_y$; they determined thermal conductivity or diffusivity [106]. Thermal conductance, κ, and the thermal conductivity with temperature increase concerning that of metal alloys. The frequency of electrons colliding with lattice phonons increases compared to pure metal

temperature and results in shorter accessible paths [6]. The value of thermal conductivity varies between 10 and 27 $\frac{w}{m.k}$ in $Al_xCoCrFeNi$ alloys. These levels are also far less than among other pure metals but close to the levels of highly alloyed, regular metals such as high-alloy steel or Ni-based superalloys [107]. HEAs get some variations in thermal conductivity when the temperature rises from 27 °C to 300 °C [106]. Thermal expansion coefficient (TEC) data are valid for $Al_xCoCrFeNi$ alloys. While Al proportion grows, the TEC of these alloys changes from 8.84×10^{-6} to 11.25×10^{-6} K^{-1}, also because Al can cause a production of BCC phase, which means that TEC decreases once the alloy structure passes from FCC to BCC [72]. Many HEAs in high temperatures have a significant hardness/strength, which thermal softening resistance comes from it [5]. Hsu et al. [108] above the transition temperatures, in $AlCoCr_xFeMo_{0.5}Ni$ alloys, the softening coefficient at high temperatures was investigated with temperature-hardness graph line, and it is less than its value in conventional high-temperature alloys (Inconel-718 & T-800) [5]. The hardness decreases steadily when the temperature increases in alloys ($Al_{0.2}Co_{1.5}Cr\ FeNi_{1.5}Ti$ and $AlCoCr_2FeMo_{0.5}Ni$), but normally at room temperature, these alloys have a great hardness [5]. The resistance of thermal softening in HEAs is mainly due to sluggish diffusion. The processes of deformation are above the transition temperature through diffusion mechanisms. Thermal softening can successfully minimize the sluggish diffusion in HEAs [5].

2.6.5. Corrosion Properties

To examine corrosion behaviour of any material, there is a normal process of electro-chemical which named potentiodynamic polarization test [109]. In both (Na-Cl & H_2SO_4) solutions, HEAs were most frequently tested for corrosion resistance [23, 110]. As compared to 304-SS and 304L-SS, HEAs have greater corrosion property strong pitting resistance in both solutions [110-112]. Alloy compositions and microstructures, particularly corrosion-resistant amounts and distributions (e.g. Cr) and galvanic corrosion participation are key factors. Fe, Co, Ni and Cr are based on several alloys analyzed [5].

Corrosion in NaCl solutions: The single-phase alloy Co-Cr-Fe-Ni has considerably better corrosion resistance than 304L-SS in this solution [5, 113]. The great amount of Ni and Cr is the factor behind it. Taking into account (Co-Cr-Fe-Ni) results in Cu rich and interdendritic phase formation, which are caused by galvanic corrosion and significantly decrease corrosion resistance [5]. By attempting to minimize the rate of the Cu-rich phase, corrosion can be enhanced with high-temperature receding [5, 114]. Additionally, the ratio of Al damages the corrosion resistance of $Al_xCrFe_{1.5}MnNi_{0.5}$ alloys, which also lowers the pitting potential of Al and extends the pitting / localized region of the corrosion of these alloys in the Na-Cl solution [115].

Corrosion in $H_2 SO_4$ Solutions: In that kind of solution, the better resistance of corrosion detected in CoCrFeNi, and compared to 304-SS, a vast difference could be noticed [112]. The corrosion qualities are harmed when Cu is attached to the Co-Cr-Fe-Ni alloy. That is because the Cu-rich cycle formed, and the action is close to the Na-Cl solution. Therefore, the size of the passive region is limited [110]. Also, additions of Al are risky and harmful [112, 115]. Thus, the structure of both phases (FCC+BCC/BCC+B2) is formed, and it is selectively removed the FCC/B2 phase in Al, Ni-rich zone [115].

2.7. Instruments

This section describes instruments (i.e., equipment) that have been used in this thesis work. These tools use various measuring methodologies based on fundamental principles of physics to give some physical quantities. In the listed sub-sections below, some schematic diagrams are mentioned to explain the details of these laboratory devices.

2.7.1. Arc Melting

Arc melting is a device widely used to fabricate alloys in so many applications. Inert gas can be supplied to prevent contamination because the atmosphere could be regulated by a vacuum chamber. However, time-consumers and expensive costs are the limitations of this strategy. In addition, the technology offers no porosity formation, and while Ti can readily be oxidized, a regulated environment eliminates the undesired reactions.

A high-voltage power supply, schematic chart of vacuum arc melting equipment, a chiller, and a turbopump all have been shown in Figure 2.5. For a melting process in producing an arc melter device, the following procedures are necessary. First of all, any undesirable dust or residuals of recent melting processes should clean the whole chamber properly with alcohol and tissue. Secondly, in a copper furnace are placed the compact mixed elements (pellet). The chamber is locked, and the vacuum pump is activated. In case the more vacuumed chamber, the better the ingot result with the least pollution. The chamber is then charged with an argon gas, a medium needed to create a spark from the electrode to the powders (raw material). Even at greater temperatures, argon gas doesn't interact with raw materials. The chamber pressure is usually selected less than air pressure ($<10^5$ Pa), which could be formed in the chamber by the assessed temperature. Using appropriate voltage and current with a power supply, the electrode is pushed after the inert injection

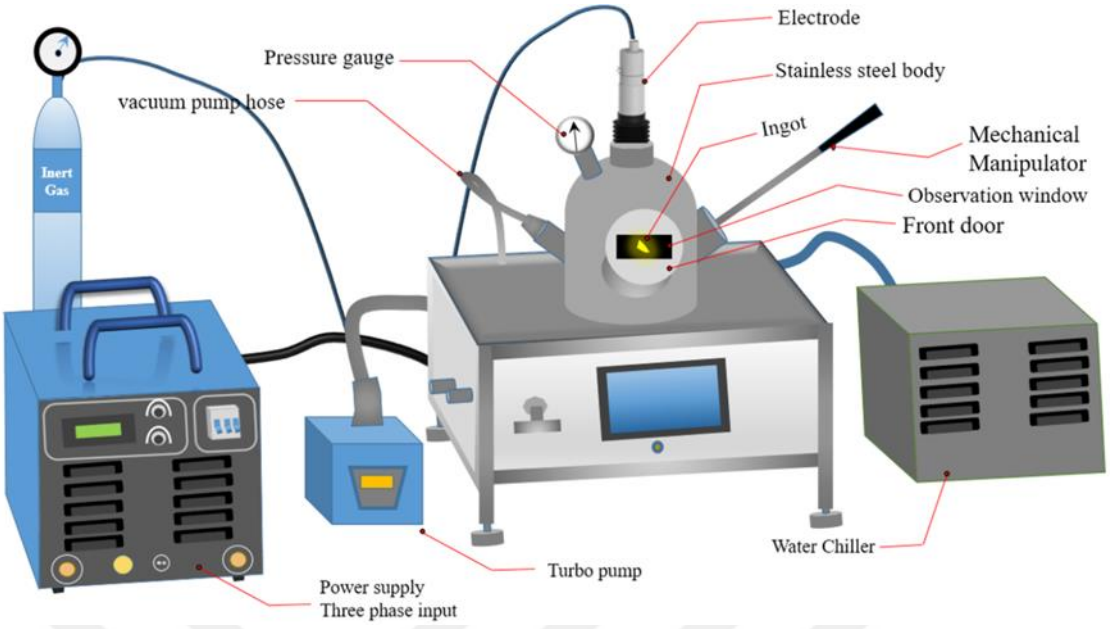

a.

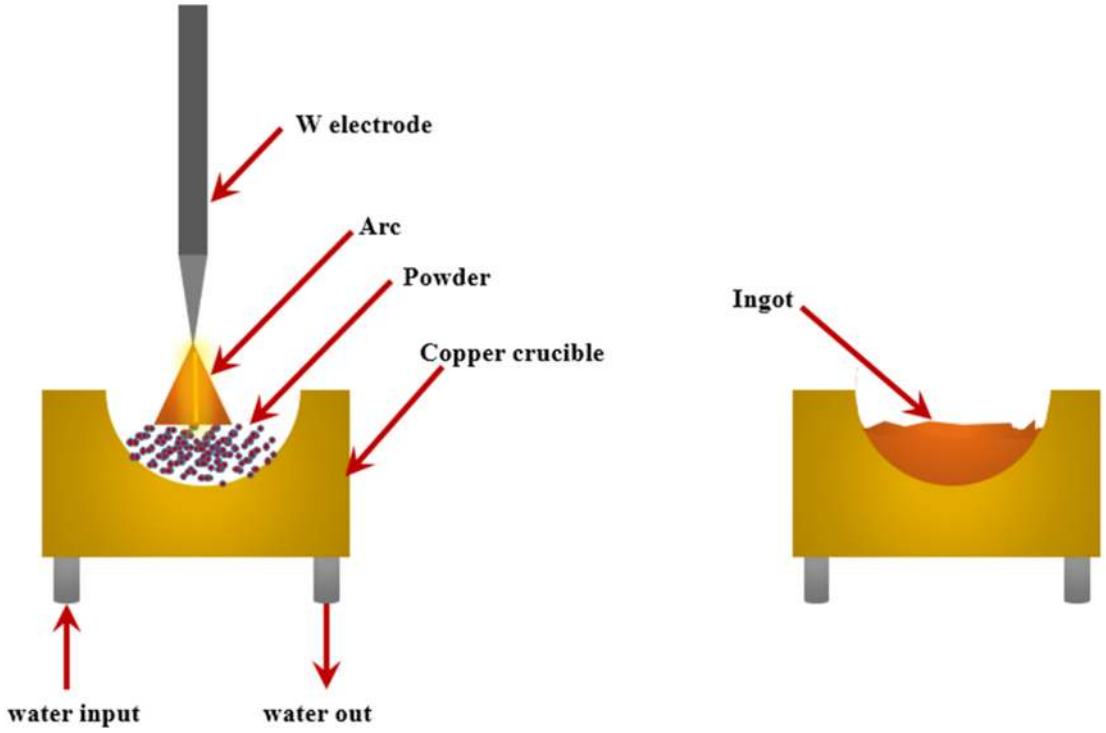

b.

Figure 2.5. (a) A scheme of a vacuum arc melting mechanism, **(b)** method of melting and ingot creation

of gas. As the electrode is negative, the crucible is positive, and the electron beam moves from the electrode. It collides with the argon gas to generate a spark-like which shows an ionized medium. The raw material could be heated up to a high degree, dependent on supplied energy. The power really should be modified to melt the material. Using a mechanical manipulator can revert after melting the entire material. The melting might be repeated numerous times to ensure the alloy's

homogenization. A fraction of the material can be evaporated or dispersed within a chamber which must be evacuated by using a fan and then let the air fill the chamber with the same air pressure to cool down within the furnace.

2.7.2. Scanning Electron Microscope – Energy Dispersive X-ray Spectroscopy

A key factor in materials is the form of crystal structure. In addition, during crystallization, microstructures develop, which depend mainly on the cooling process. Energy dispersive X-ray spectroscopy (EDS) scanning electron microscope (SEM) can determine the shape, size, and content of microstructures. SEM is an amazing technology for analysis employing a powerful beam of the electron beam on the sample surface with a lens, which is higher in magnification than an optical microscope (see Figure 2.6 (a)) [116]. Figure 2.6(b) shows specific SEM image [117]. A tungsten filament emits electrons, and an anode accelerates the electrons in one direction. The electrons are then focused with a magnetic lens on the sample. A scan coil changes the direction of the electron beam. When highly kinetic electrons hit the atoms on the sample surface, they are exposed to many scenarios.

Besides, a particular portion of the electrons is dispersed by a backscatter detector on the object's surface. A computer analyzes this measurement component to simulate a clear photograph of the sample. This measurement may also need more pre-works for some samples, like when the sample is cutting and the cross-section needs to be smoothed. In addition, another component of the electrons involved could penetrate the material and transfer a portion of their energy into atomic core electrons. When core electrons receive enough energy, they depart the atom, so additional electrons from high energy levels are filled into their states. Photons are therefore emitted from these specific atoms with a defined wavelength. An energy-scattering x-ray detector observes all these radiations. Each element has a particular number of electrons that make the creation of X-rays different [118]. Thus, the type of chemicals and their amounts, especially for heavy metals as Ni, Ti, Sn, Zn, Cu, may be correctly defined by examining the patterns received [119]. Furthermore, the components can be displayed on the sample surface on a map depending on different colours, as can be noticed from Figure 2.6(c) [120].

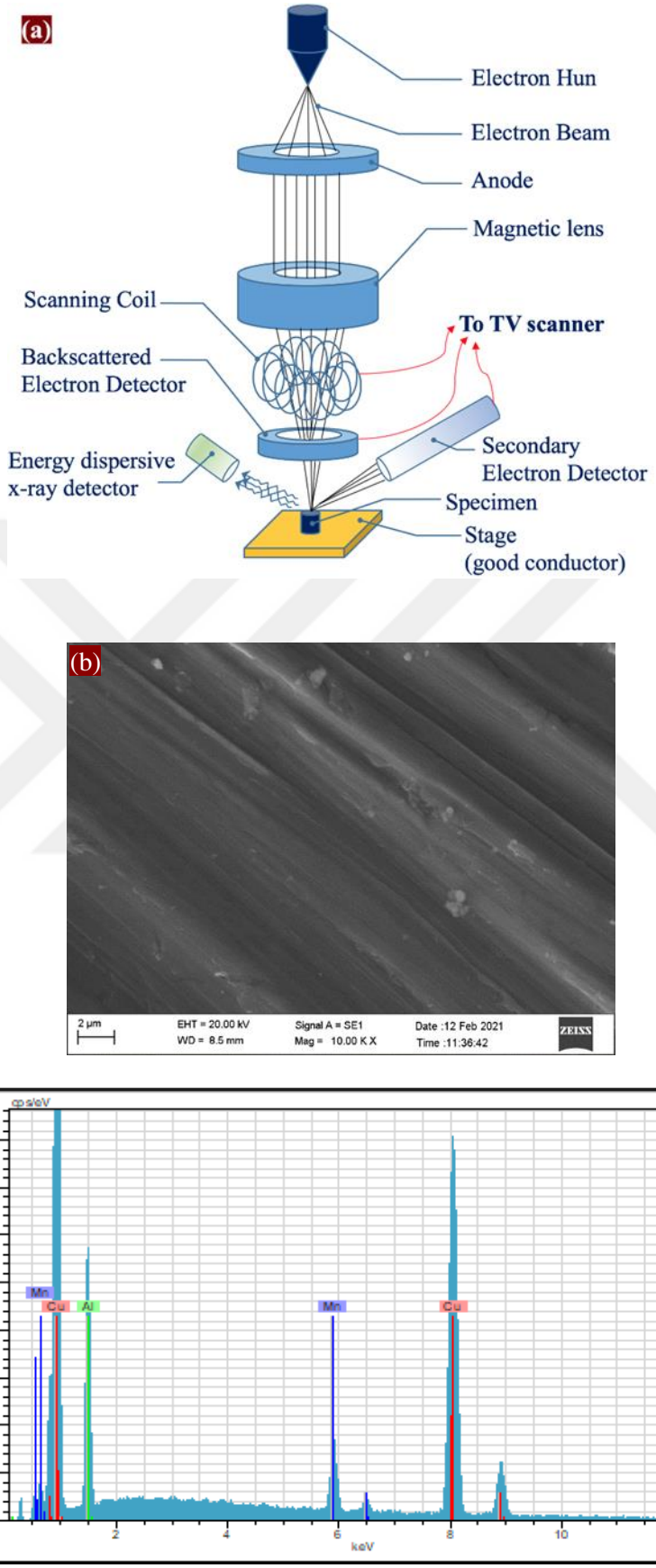

Figure 2.6. **(a)** The schematic diagram of SEM-EDX equipment [116], **(b)** SEM picture of NiTiCoMnFe-V sample [117], and **(c)** CuAlMn alloy's EDX result [120]

2.7.3. X-ray Diffraction (XRD)

The most used technique to deal with crystal structure and atomic spacing is X-ray diffraction (XRD). This is because the material's crystal structure affects the mechanical and other physical qualities. The XRD device consists of three main parts: a sample holder, an X-ray tube, and a detector to detect diffracted X-ray beams. The creation of X-rays is carried out by heating a filament; it uses metal with a high melting temperature; in a cathode tube, the filament has to produce an electron from the metal, after heating the filament, the electrons start to escape the atoms outer shell since they have enough energy. After this operation, the formatted electrons have to be accelerated to the target direction or a direction by placing the high voltage on the target material and bombarded with electrons, as shown in Figure 2.7(b) [121].

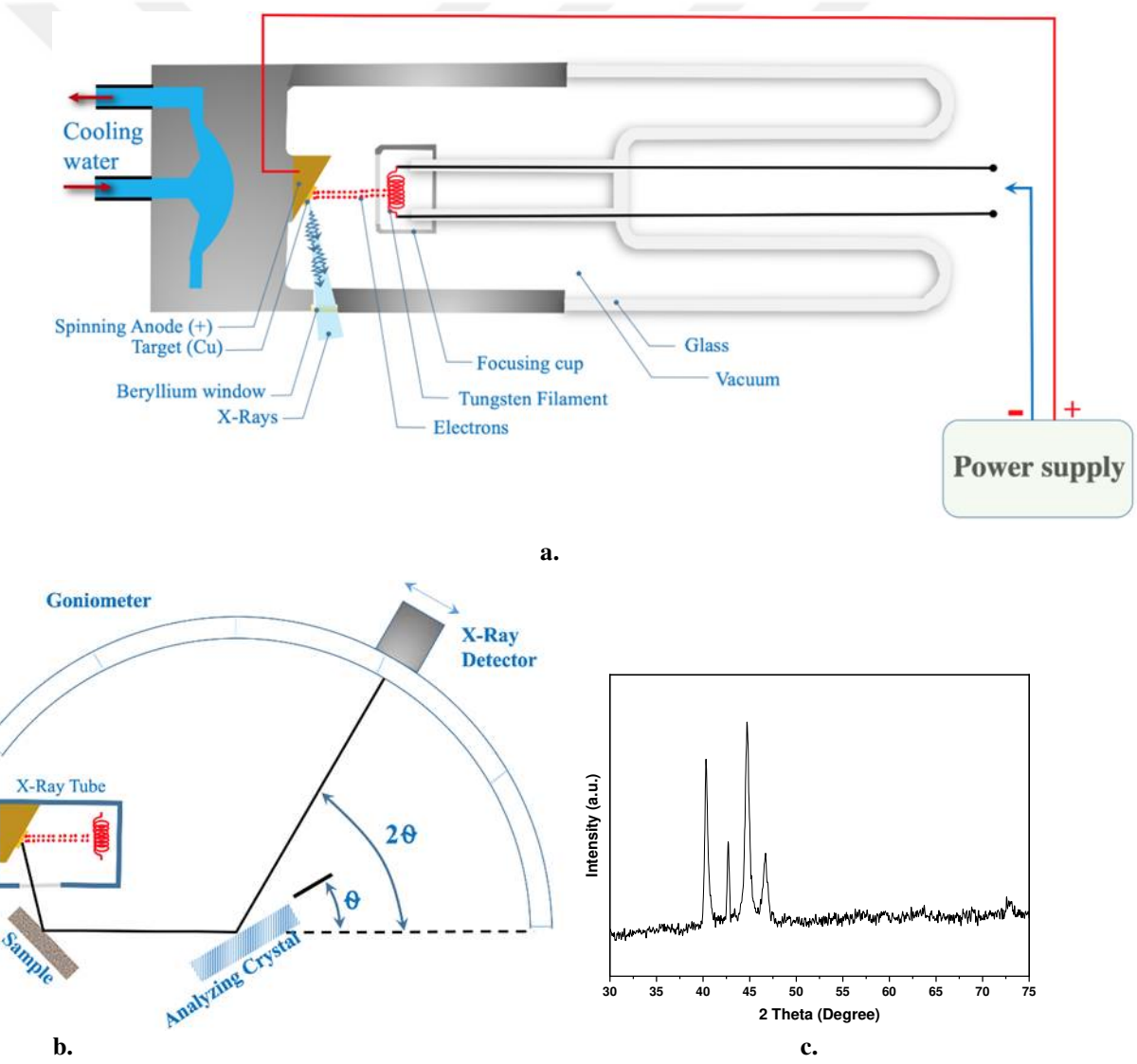

Figure 2.7. (a) The X-ray device illustration, **(b)** X-ray diffraction testing technique, and **(c)** peaks represent diffracted X-ray patterns [121, 122]

In addition, the crystal structure of an atom could be obtained from X-ray results based on Bragg's law ($n\lambda = 2d \sin\theta$) where n is an integer number, λ is a wavelength of the X-ray beam, d is the crystal's constant distance, and θ is a diffraction angle [123]. Because X-rays have a short wavelength, they can be employed to search for crystallographic issues. Figure 2.7(a) shows an overview of an X-ray tube and its performance of the X-ray diffraction test. Besides, Figure 2.7(c) presents X-ray diffracted patterns peaks [122].

Moreover, the outcome is a pattern that cannot be easily understood but must be analyzed. The lattice characteristics for different elements and compounds are different, and hence an updated database should be used to index the findings. Copper is usually employed for the target in an X-ray pipeline, and X-rays with different wavelengths are produced by bombarded electrons. Monochromatic radiation is used, and the remaining wavelengths are filtered through the beryllium glass.

2.7.4. Vibrating Sample Magnetometry (VSM)

Vibration sample magnetometry (VSM) is dependent on Faraday's law, which provides the generated electromagnetic force in a spherical coil when flux through a spindle is changed [124]. A magnetic sample moves towards two pickup coils, as shown in Figure 2.8, during the measurement operation.

The oscillator sends a sinusoidal signal converted into a vertical vibration through the transducer movement. The sample attached to the sample rod swings at a specific frequency in a range of 60-80 Hz and amplitude 1 mm. It is centrally located between two poles of an electromagnet that creates a high-homogeneity magnetic field $\vec{H}_0$. In laboratory VSM setups, field strengths of 10^6 A/m are usually possible. Steady pick-up coils are placed on the electromagnet poles. Their centre for symmetry corresponds mostly with the static sample magnet. The magnetic flux fluctuation that comes from the vertical movement of a magnetized sample causes a voltage in the coils. $\vec{H}_0$ remaining unchanging, it has no voltage effect, but it is solely necessary for sample magnetization. The sample is magnetized with in field direction, giving in the $\vec{m}$ magnet moment, when the sample is brought into the homogeneous field $\vec{H}_0$ on the x-axis. The sample is then regularly shifted concerning the pick-up coils. The variation of the magnetic flux density $\vec{B}$ can be observed when the magnetic moment moves at the distance (r) of one point from the sample.

The changes in magnetic flux duration are clear from the vertical sample movement regarding the coils. Therefore, the flux changes recorded by the coils are due to several amounts: the magnetic moment of the sample, the distance to pick-up coils, the vibration's frequency, and its amplitude. Consequently, a voltage can be raised by increasing the number of winds used in the modified device and the number of pick-up coils. Induction is also influenced by the shape of the

coils [125]. Even at very low magnetic moments, the measures are sensitive. Recently, the vibrating magnetometers of the sample can determine magnet moments of μ emu that are equivalent to 10^{-9} g of iron.

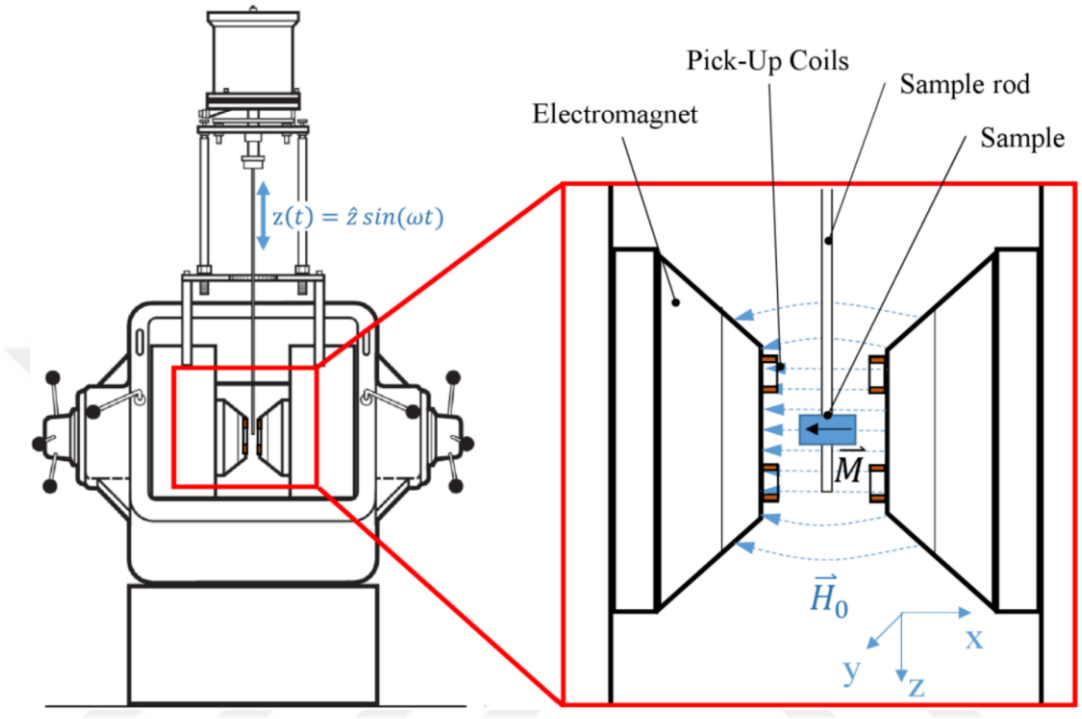

Figure 2.8. The schematic diagram of the VSM device [124]

2.7.5. Thermogravimetric Analysis/Differential Thermal Analysis

Thermogravimetric analysis/Differential thermal analysis (TGA/DTA) is an instrument that measures mass changes and other thermal characteristics of a material in isothermal and non-isothermal (athermal) operations. Figure 2.9 is a schematic illustration of the TGA/DTA device, where there is a heating system based on Joule heating (Ohmic heating), yet the cooling process is naturally done out.

The TGA/DTA device has two sensitive balances to determine mass variation in the microgram (μg). The sample is usually placed in a crucible formed of inert material, such as silver, aluminium, and platinum, dependent on material type. A crucible is enclosed in some of these DTA scenarios to limit evaporation. The crucible must be open to allow weight loss and mass gain through the sample throughout the thermogravimetry procedure. To achieve a successful measurement, some thermal effects of the crucible should be cancelled. Hence, a reference used in this device could be the same blank container. The bottom of the crucibles (reference and sample) is attached to a sensitive thermocouple to measure temperature depending on the time.

In addition, this device combines two instruments that could measure two different things in the way of DTG/DTA. For athermal and isothermal processes, TGA can indeed be done. The sample atmosphere is not controlled during the athermal process, and the temperature is constantly increased (K/min). The temperature difference can be observed in oxidation (mass increase) or reduction (mass loss). Software to examine the findings of the thermographs and specific fundamental calculations can be done. The conclusions may be drawn in a graph of two dimensions to represent the change of mass and temperature (or time) accordingly in the y-axis and x-axis.

DTA requires a regulated atmosphere; hence pure gas is used during the actual test. Argon, nitrogen, helium, air, various gasses, and vacuum may control the atmosphere. Multiple materials can be analyzed, including glasses, ceramics, polymers, plastics, metals, and composite materials. The shape of the material is no different for measuring, either in powder or in bulk [126]. The sample weight should be from 1 to 150 mg, although for measurement accuracy, the sample is preferable with more than 100 mg, while the sensibility is up to 0.01 mg [127].

Besides, there is another device which is differential scanning calorimetry (DSC), which can give almost the exact measurements, even though DSC works in a limited region refer to temperature (>400 ℃). In comparison, DTA could be used in high-temperature measurements (till 1000 ℃).

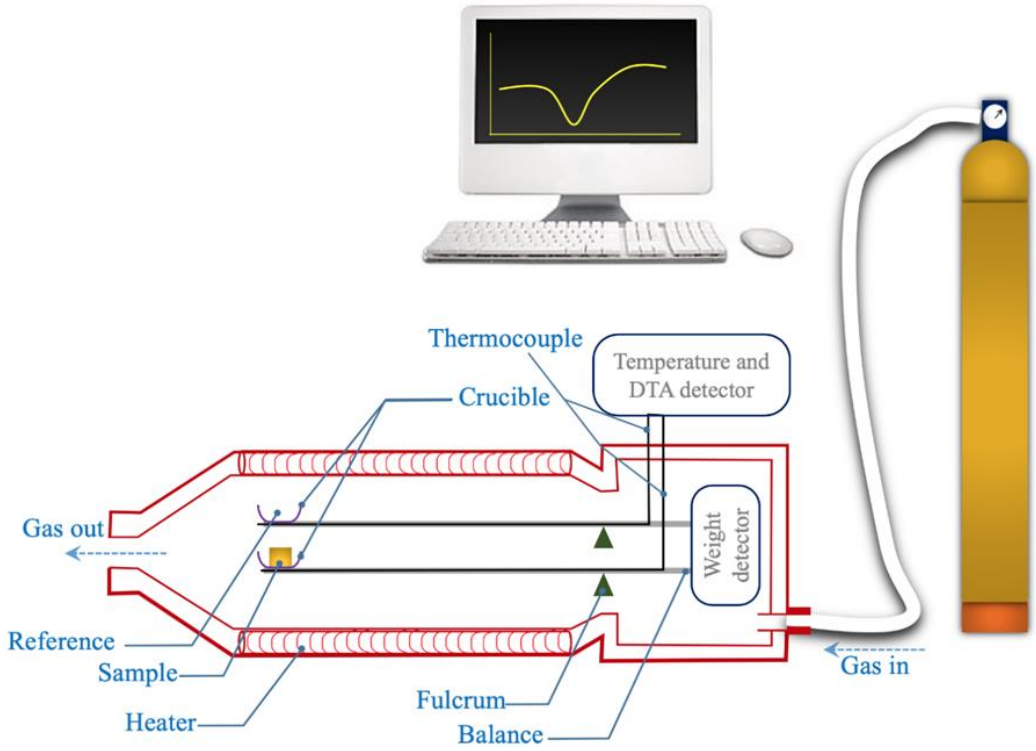

Figure 2.9. The TG/DTA system schematic illustration

3. MATERIALS AND METHODS

This chapter is divided into three main sections: materials, fabrication process, and characterization methods. Furthermore, it will give details about the compositions of the samples, fabrication process, and characterization methods for all alloys that have been studied in that research work.

3.1. Materials

In this research, eleven different elements were used to produce seven other new composition alloys, High entropy alloys (HEAs). Furthermore, all powders of impurity elements near 99.99% were picked. Table 3.1 shows the selected compositions of the alloys in atomic ratios with named alloys (alloys' codes). To perform the equivalent computation for changing weight percentage to atomic percentage and vice versa, the following equations (3.1 and(3.1)) were used [128]:

$$(at.\%)_x = \frac{(wt.\%)_x/(at.wt.)_x}{\sum_i (wt.\%/(at.wt.))_i} \times 100 \quad (3.1)$$

$$(wt.\%)_x = \frac{(at.\%)_x \times (at.wt.)_x}{\sum_i (wt.\%)_i \times (at.wt.)_i} \times 100 \quad (33.2)$$

Table 3.1. Compositions in at.% and Alloys' code

Alloys' code / Elements	PCI-1	PCI-2	PCI-3	PCI-4	PCI-5	PCI-6	PCI-7
Al	20	18	18	18	18	18	18
Co	20	18	18	18	18	18	18
Fe	20	18	18	18	18	18	18
Mn	20	18	18	18	18	18	18
Ni	20	18	18	18	18	18	18
Ti	-	10	-	-	-	-	-
Cr	-	-	10	-	-	-	-
Sn	-	-	-	10	-	-	-
V	-	-	-	-	10	-	-
Hf	-	-	-	-	-	10	-
Ga	-	-	-	-	-	-	10

3.2. Fabrication Process

To get accurate results, highly sensitive devices and tools were used. Indeed, a few steps were taken to produce FeCoNi-based HEAs samples. First, the weighing process was done to determine powders using a sensitive balance machine (0.1 mg). Figure 3.1 shows the balance equipment that used in this research. After that, the prepared powders were mixed mechanically using a stirrer bar inside the container with the Hot&Stirrer (MA300HS) device, shown in Figure 3.2. The device could use heating till 380 ℃ and rotating ability till 150 rev/min. Pelletizing is widely used before the melting process in metallurgy community and material science studies. For that, a handheld compressor with a gauge to show the given pressure to press powders can be seen in Figure 3.3. The handheld compressor was used to apply pressure on powders to get pellet form. Furthermore, weighed elements were compressed into 20 mm diameter of pellets.

Lastly, the arc melting furnace (as shown in Figure 3.4) was vacuumized first, and argon gas was used to fill the chamber. This procedure was performed twice to remove unwanted gases. The pressed pellets were then put in the arc melting oven. Tungsten electrodes on the copper skillet were used in melting materials. By reversing the melted materials being re-melted, the atoms were distributed homogenously. During the solidification of the material, the same atoms form precipitations in a specific region. To prevent unwanted irregular structures or dendrite formations made by these atoms, the distribution of atoms within the structure is provided by diffusion. Therefore, the material is exposed to high temperatures for a period that will allow the melting temperature to be around 0.8-0.9Tm. At the end of the period, the material is quickly cooled in ice water. In this way, atoms are prevented from escaping through crystal structures that contract during cooling. Before taking characterizations, the samples received from arc melting were cut into small pieces for EDX-SEM, XRD, VSM, and DTA analyses.

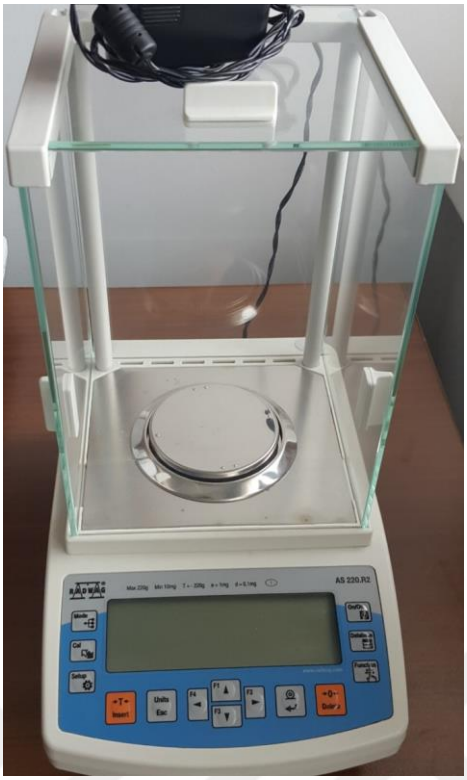

Figure 3.1. An electronic balance which used for weighting materials powders

Figure 3.2. Mechanical mixture

Figure 3.3. A handheld compressor

Figure 3.4. Arc melting device that used in this study

3.3. Characterization Methods

A critical step towards the various behaviour of the alloys is the characteristics of the fabricated alloys. This procedure guarantees the provision of critical information on the different physical characteristics of alloys. The results were compared with the literature to improve future research in good and bad influences.

3.3.1. SEM-EDX Analysis

Compositional and microstructural tests were done by utilizing SEM-EDX for enough portions of all sample alloys with 20 kV power. Besides, all samples' surfaces were scanned at room temperature using SEM-EDS equipment. The SEM-EDS chamber was vacuumed, and a different magnification of the scanning surface was done. T_o achieve the composition of different microstructures, EDS measurements were also carried out. Figure 3.5 shows the SEM-EDX device (Zeiss EVO/MA10) used in this research.

Figure 3.5. SEM-EDX device which used in this study

3.3.2. Crystal Structure Analysis

The crystal structure study for all sample alloys was carried out using a Bruker D8 Advance X-ray diffractometer. Figure 3.6 shows the X-ray diffractometer that could be controlled with

computer help being used in this work. In addition, all measurements were taken for the 2θ scan ranging from 20° to 90° with step size 0.02 at room temperature with a speed of 2 deg/minute. A monochromatic X-ray (Cu K_α) was used. The Braggs law can use to analyze patterns of XRD.

Figure 3.6. X-ray diffraction instrument which used in this work

3.3.3. Vibrating Sample Magnetometry (VSM)

Vibrating sample magnetometry (VSM) was performed to examine the alloys' usefulness for magnetic applications. Figure 3.7 shows the VSM (model Quantum Design PPMS9T) device used in this study. Moreover, all measurements have been done at room temperature with the applied field through -60Koe to +60Koe.

Figure 3.7. The VSM device used in this work

3.3.4. Thermal Analysis

Differential thermal analysis (Shimadzu DTG-60AH) was used to take thermal measurements. Figure 3.8 shows the photograph of the DTA devices used in that study. Moreover, all samples were located in a platinum pan and heated from room temperature to 900 ℃ with a heating/cooling rate of 20 ℃/min. The homogenized samples' mass was in the range of (29mg – 54mg). Argon gas is used to control the atmosphere in order to keep safe samples in oxidation. DTA peaks were analyzed by a thermal analyzer device (Shimadzu TA-60WS) with a software program. That program uses the Tangent differentiation method to calculate the DTA peaks and determine the integrated peak areas, and it also counts peak start, finish, maximum/minimum. Therefore, these integrated peak areas could obtain the enthalpy and heat change amount.

Figure 3.8. The TG/DTA equipment which used in that research

4. RESULTS AND DISCUSSION

In this chapter, all results from the experimental part are listed in five sections, including EDX, SEM, XRD, VSM, and DTA measurements. Besides, all results are given through graphs and tables with explanations for all seven fabricated alloys. Furthermore, the physicochemical properties of used elements are provided in Table 4.1, which help some thermodynamic and physical calculations (Table 4.3).

Table 4.1. Atomic number, symbol, radius, Pauling electronegativity, VEC, and melting point for elements used in that study [48, 129]

Elements	Symbol	Atomic No.	Radius (Å)	Pauling electronegativity	VEC	Melting point (℃)
Aluminum	Al	13	1.432	1.61	3	660.32
Cobalt	Co	27	1.251	1.88	9	1495
Iron	Fe	26	1.241	1.83	8	1538
Manganese	Mn	25	1.35	1.55	7	1246
Nickel	Ni	28	1.246	1.91	10	1455
Titanium	Ti	22	1.462	1.54	4	1668
Chromium	Cr	24	1.249	1.66	6	1907
Tin	Sn	50	1.62	1.96	4	231.93
Vanadium	V	23	1.316	1.63	5	1910
Hafnium	Hf	72	1.578	1.3	4	2233
Gallium	Ga	31	1.392	1.81	3	29.76

Once Al is included in CoFeMnNi HEA, it could offer several advantages. Firstly, the Solid solution-phase structure is enhanced because all selected components in CoFeMnNi (provided in Table 4.2) have a negative enthalpy of mixing with Al [39]. Secondly, alloy system lattice distortion prevents dislocation movement and may increase alloy strengthening due to Al having a larger atomic radius than other metals like Fe, Ni, Co, or Mn [5]. Thirdly, when Al and Cr are included in HEA, it improves the corrosion properties of HEAs [130, 131]. Finally, for the case of HEA, adding a different composition could improve the entropy of mixing and favour the formation of a solid solution phase rather than precipitating intermetallic phases [39].

From equation 2.1 and equation 2.2, the ΔS_{conf} calculated for all seven fabricated alloys which meet the boundary of HEAs ($\Delta S_{conf} \geq 1.61\ R$). In this context, all seven samples should be counted as HEA. In addition, the value of ΔS_{mix} could be obtained from multiplying ΔS_{conf} by R. Furthermore, the excellent parameter to determine the formations in HEAs of sole-solid-solutions is ΔH_{mix}. Furthermore, ΔH_{mix} could form a solid solution in the range ($-5\ \mathrm{kJ/mol} \leq \Delta H_{mix} \leq$

5 kJ/mol) [132], but this range recently extended in two separate studies such as $-20\ \text{kJ/mol} \leq \Delta H_{mix} \leq 5\ \text{kJ/mol}$ [84] and $-22\ \text{kJ/mol} \leq \Delta H_{mix} \leq 8.5\ \text{kJ/mol}$ [5]. Additionally, compounds may be noticed when ΔH_{mix} is more negative [49]. The following equation (4.1) should be used to calculate the ΔH_{mix} value [84]:

$$\Delta H_{mix} = 4 \sum_{i=1, i \neq j}^{N} \Delta H_{ij}^{mix} x_i x_j \qquad (4.1)$$

mixing enthalpy of the binary liquid between the ith and jth components in an equiatomic ratio represented as ΔH_{ij}^{mix}. Table 4.2 gives the ΔH_{mix} values of the binary alloys which took a part of fabricated samples. Due to the reported range of the ΔH_{mix} which mentioned above, ΔH_{mix} value of all samples (see Table 4.3) is in the range of $-10.98\ \text{kJ/mol}$ to $-19.8\ \text{kJ/mol}$, which means that these alloys are in solid solution and satisfy clearly.

Table 4.2. ΔH_{mix} (KJ.mol^{-1}) values of the binary alloys that participated in produced alloys [82]

Elements	Al	Co	Fe	Mn	Ni	Ti	Cr	Sn	V	Hf	Ga
Al		-19	-11	-19	-22	-30	-10	4	-16	-39	1
Co			-1	-5	0	-28	-4	0	-14	-35	-11
Fe				0	-2	-17	-1	11	-7	-21	-2
Mn					-8	-8	2	-7	-1	-12	-13
Ni						-35	-7	-4	-18	-42	-15
Ti							-7	-21	-2	0	-23
Cr								10	-2	-9	-1
Sn									-1	-35	1
V										-2	-8
Hf											-34
Ga											

As mentioned in chapter two (see section 2.4), in identifying phases, whether BCC or FCC, the VEC plays a critical role [11], and the value of VEC should be determined from equations 2.3a and b. The crystalline lattice kinds can be predicted by VEC assisted by the Hume-Rothery rule [11, 49, 78]. In addition, the sole BCC phase could obtain through $\text{VEC} \leq 6.87$ regions; also, both FCC and BCC phases have coexisted when the VEC value gets between 6.87 and 8, and wherever VEC satisfied $8 \leq \text{VEC}$ (gets over 8), then the FCC phase would be seen [49, 79, 80]. In this present work, the VEC value of all alloys is located in the range between 6.96 and 7.4, which means all samples have BCC+FCC phase, as is confirmed by experimental results. Al has been the most

commonly documented element that causes microstructures to have both BCC and FCC phases [133, 134].

Yang et al. [81] reported two parameters (Ω and δ) to predict phase formations in HEAs. Ω signifies the competition between enthalpy and entropy, and it can be calculated from this equation ((4.2):

$$\Omega = \frac{T_m \, \Delta S_{mix}}{|\Delta H_{mix}|} \tag{4.2}$$

when ΔS_{mix} is the mixing entropy, ΔH_{mix} is the mixing enthalpy, and $T_m = \sum C_i \ (T_m)_i$ is the melting temperature of the alloy. δ symbolizes the difference in atomic size, and it is provided by ((4.3):

$$\delta = \sqrt{C_i \left(\frac{1 - r_i}{\bar{r}}\right)^2} \tag{4.3}$$

when r_i is the atomic radius and C_i is an atomic percentage of the i[th] element. Further, $\bar{r} = \sum_{i=1}^{n} C_i \, r_i$ is the average radius [135]. Based on Yang et al.'s research, the conditions for the formation of high-entropy stabilized solid solution phases are $\Omega \geq 1.1$ and $\delta \leq 6.6\%$ [81]. Zhang et al. extended the limit of δ ($\delta \leq 8.5\%$) [84]. The sixth column, which gives Ω for all samples, it's noticeable that most of the studied alloys do not exceed the limit of Ω. In both cases of PCI-2 and PCI-6, the values of Ω fall between 1 and 1.1, it refers to the high negativity of mixing enthalpy of both two alloys. Besides, the column of δ listed the value of atomic size difference for all studied alloys. Even though most of the values approve the condition for δ but it gets 8.9 for the PCI-6 sample. It can be explained through the high atomic number and Pauling electronegativity of Hf compared to other elements contained in the rest of the samples. In addition, the atomic size difference between the alloying elements must be minimal enough to avoid the crystal structure of the alloy accumulating excessive strain energy, which results in crystal distortion [136].

Table 4.3. The fabricated alloys' physical and thermodynamic properties have been computed

Alloys' code	ΔS_{conf}	ΔS_{mix} (J. Kmol^{-1})	ΔH_{mix} (KJ.mol^{-1})	VEC	Ω	δ	T_m (°C)
PCI-1	1.61 R	13.38	-13.92	7.4	1.23	5.8	1278.9
PCI-2	1.77 R	14.75	-19.77	7.06	1	6.52	1343.3
PCI-3	1.77 R	14.75	-12.71	7.26	1.59	5.67	1375.1
PCI-4	1.77 R	14.75	-10.98	7.06	1.48	8.9	1103.25
PCI-5	1.77 R	14.75	-15.3	7.16	1.33	5.51	1384.9
PCI-6	1.77 R	14.75	-19.62	7.06	1.05	8.2	1391.3
PCI-7	1.77 R	14.75	-14.15	6.96	1.11	5.83	1069.75

4.1. Microstructure Analysis

To get chemical compositions in an atomic ratio (at.%), Burker model energy dispersive X-ray (EDX) was utilized to determine the compositions of all elements for each alloy. All samples produced in that research are equiatomic HEAs. Furthermore, the first sample (PCI-1 alloy) contains $Al_{20}Co_{20}Fe_{20}Mn_{20}Ni_{20,}$ and the rest of the alloys are $Al_{18}Co_{18}Fe_{18}Mn_{18}Ni_{18}X_{10}$ (X= Ti, Cr, Sn, V, Hf, Ga). The composition ratios relying on EDX results are given in Table 4.4. The results from the EDX of all samples are similar to the nominal compositions. The melting temperature of aluminium is lower than the other elements in the system, which explains why the aluminium was lower than expected. Figure 4.1, Figure 4.2, Figure 4.3, Figure 4.4, Figure 4.5, Figure 4.6, and Figure 4.7 show the EDX results of the PCI-1, PCI-2, PCI-3, PCI-4, PCI-5, PCI-6, and PCI-7 alloy, respectively.

Table 4.4. The compositions ratio of different elements provided by EDX results of all samples in at.%

Alloys' code / Elements	PCI-1	PCI-2	PCI-3	PCI-4	PCI-5	PCI-6	PCI-7
Al	12.97	10.15	4.11	9.09	2.94	14.42	14.00
Co	24.14	24.06	22.28	21.47	24.85	22.71	20.76
Fe	23.97	21.92	22.66	22.84	24.05	21.09	18.85
Mn	17.46	8.67	17.39	14.36	16.80	13.45	14.86
Ni	21.47	21.79	21.71	23.44	21.21	17.42	19.44
Ti	-	13.41	-	-	-	-	-
Cr	-	-	11.87	-	-	-	-
Sn	-	-	-	8.81	-	-	-
V	-	-	-	-	10.15	-	-
Hf	-	-	-	-	-	10.91	-
Ga	-	-	-	-	-	-	12.10

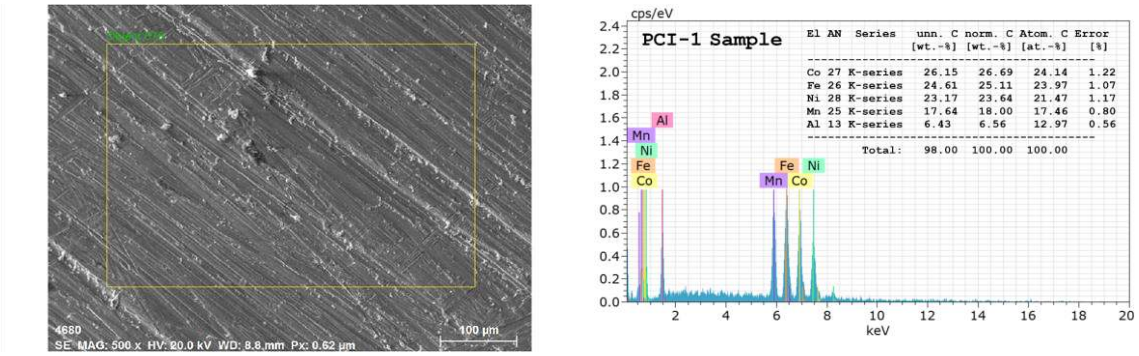

Figure 4.1. The EDX results of the PCI-1 alloy

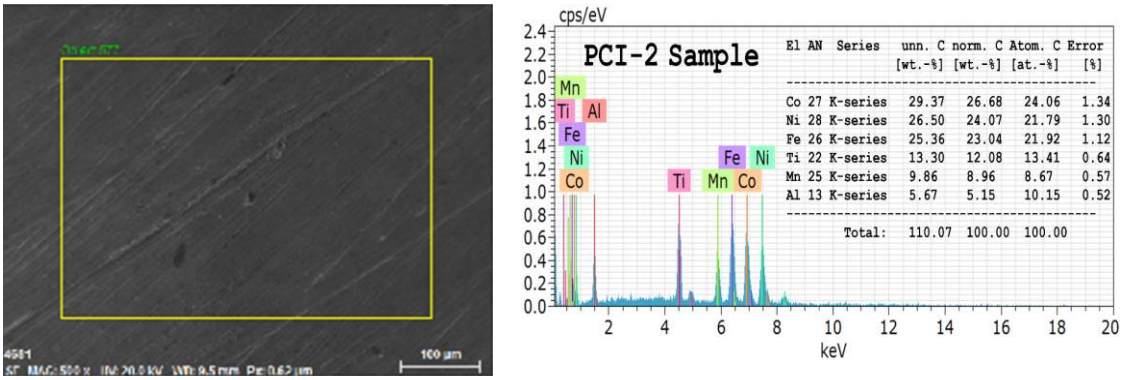

Figure 4.2. The EDX results of the PCI-2 alloy

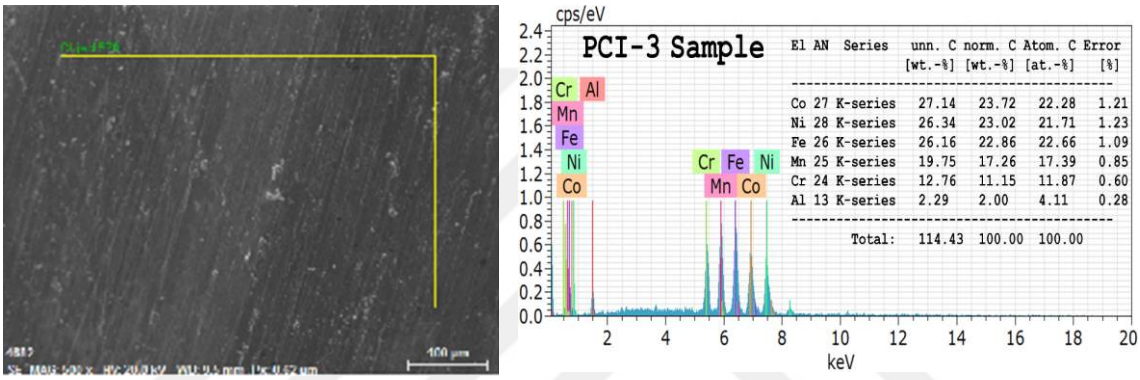

Figure 4.3. The EDX results of the PCI-3 alloy

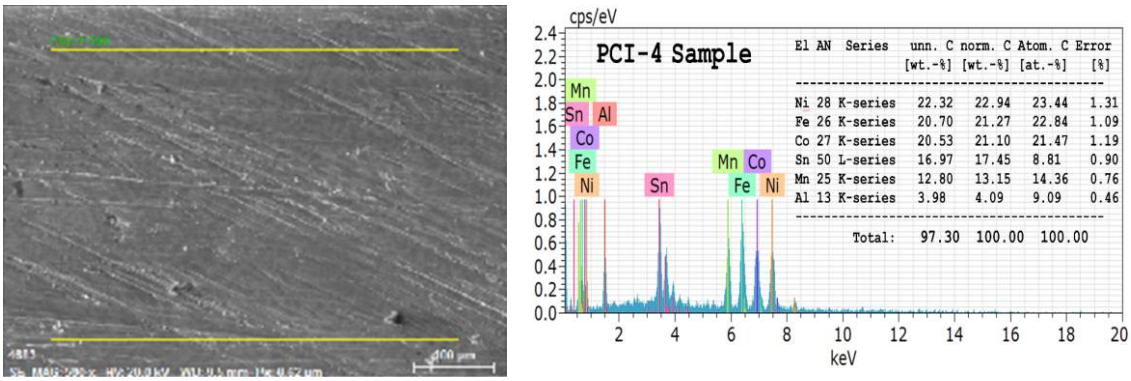

Figure 4.4. The EDX results of the PCI-4 alloy

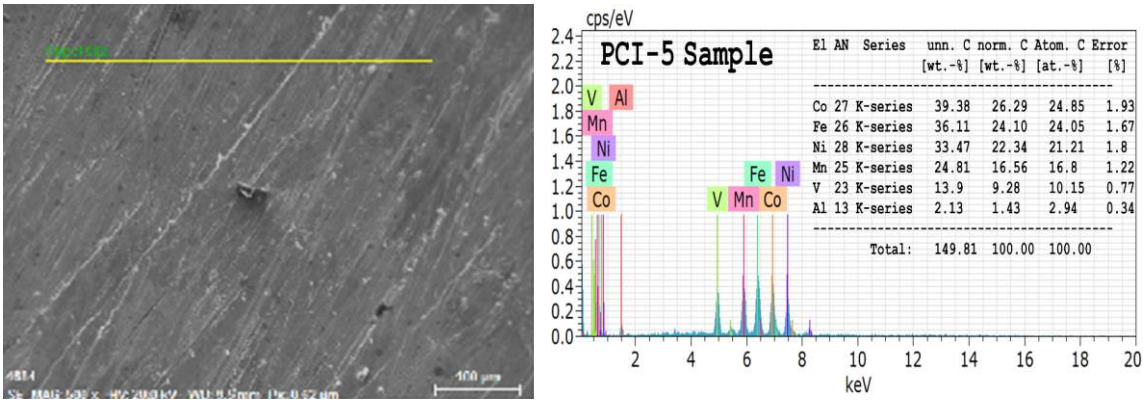

Figure 4.5. The EDX results of the PCI-5 alloy

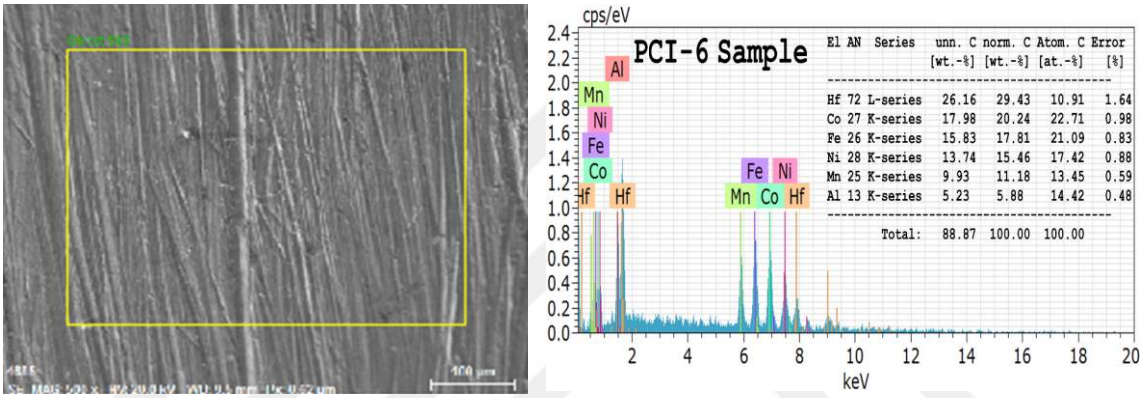

Figure 4.6. The EDX results of the PCI-6 alloy

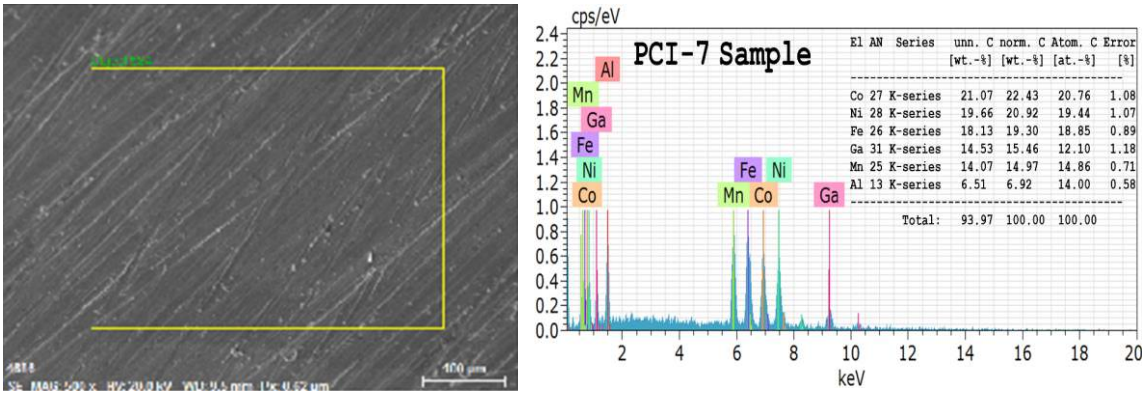

Figure 4.7. The EDX results of the PCI-7 alloy

4.2. SEM Results

SEM characterizations were performed at room temperature to deal with the microstructure of the fabricated samples. The SEM results are given in Figure 4.8, Figure 4.9, Figure 4.10, Figure 4.11, Figure 4.12, Figure 4.13, and Figure 4.14 for the PCI-1, PCI-2, PCI-3, PCI-4, PCI-5, PCI-6,

and PCI-7 sample respectively. From the results were obtained, it is significant that the microstructure of the samples was in V shape, which is one of the common microstructure shapes in martensite phase structure [137]. Furthermore, it is noticeable that the surfaces don't contain holes from the images. This agrees that the elements dissolve entirely in the arc melting furnace, and the bulk defect (pores) doesn't appear. This is one advantage of using arc melting to fabricate samples because both these techniques, induction melting and stirring, cause the appearance of many pores.

Further, the addition of the elements in this study doesn't affect much on microstructure; this is due to little change in the composition of the samples, which is only 10%. On the other hand, the differences in the quenching speed of the samples could affect their microstructure. Moreover, small spherical shapes spread out over the surfaces that indicate the appearance of the second phase [138].

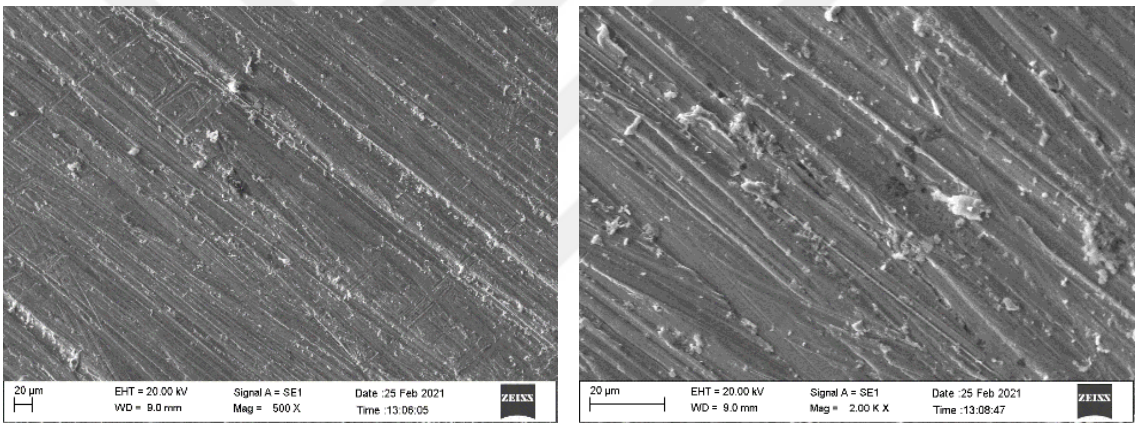

Figure 4.8. The SEM images of the PCI-1 sample

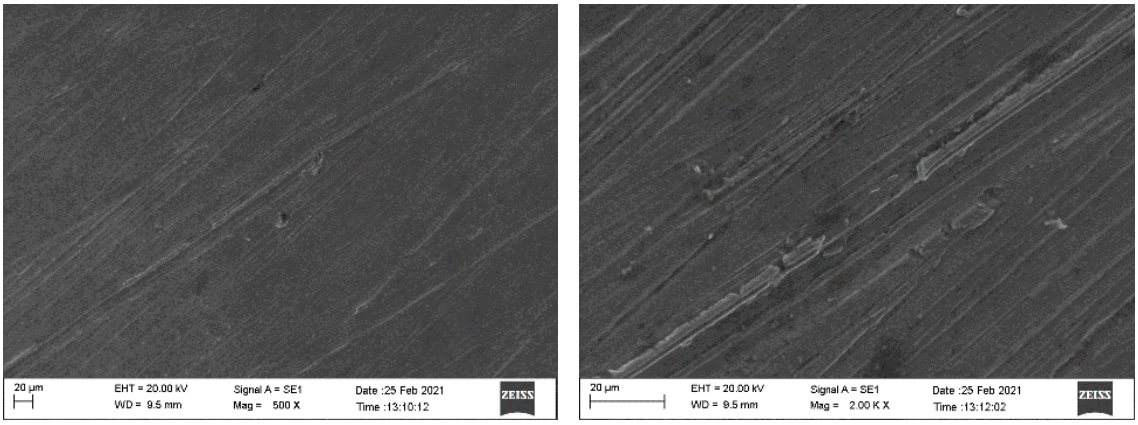

Figure 4.9. The SEM images of the PCI-2 sample

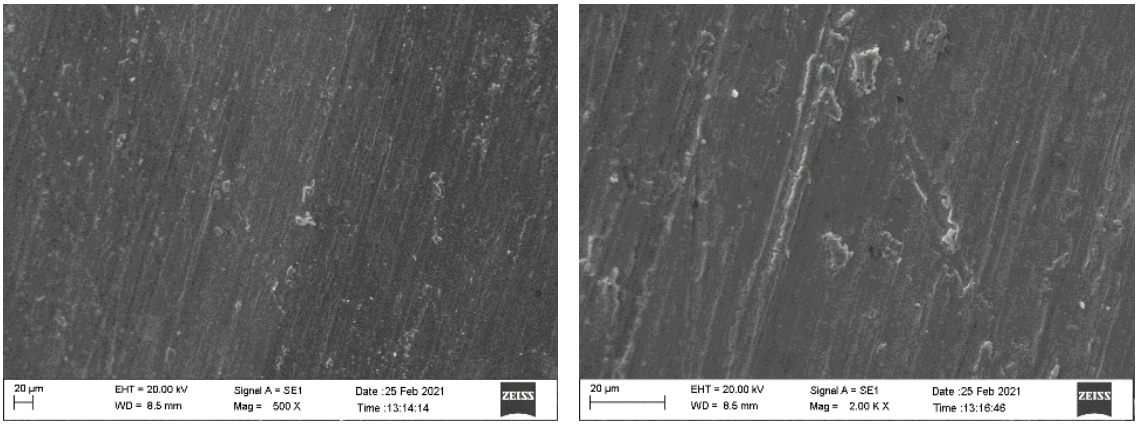

Figure 4.10. The SEM images of the PCI-3 sample

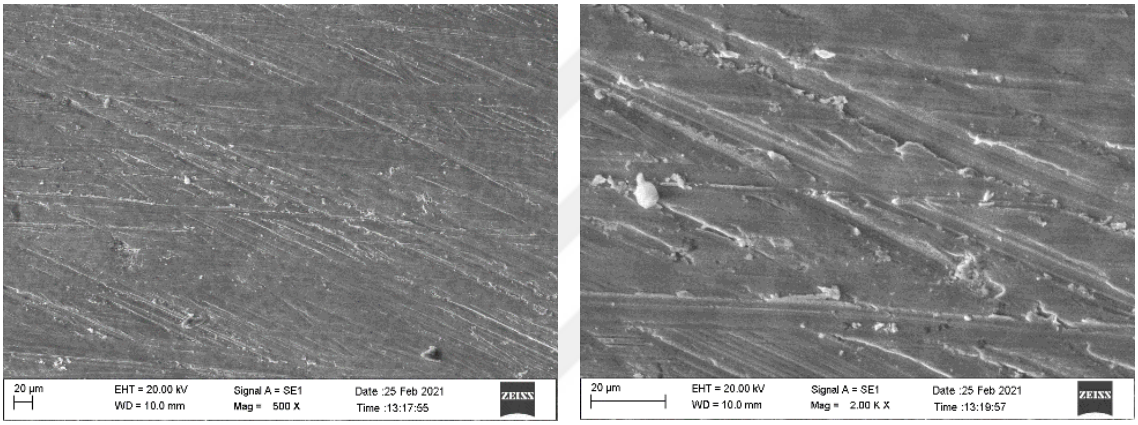

Figure 4.11. The SEM images of the PCI-4 sample

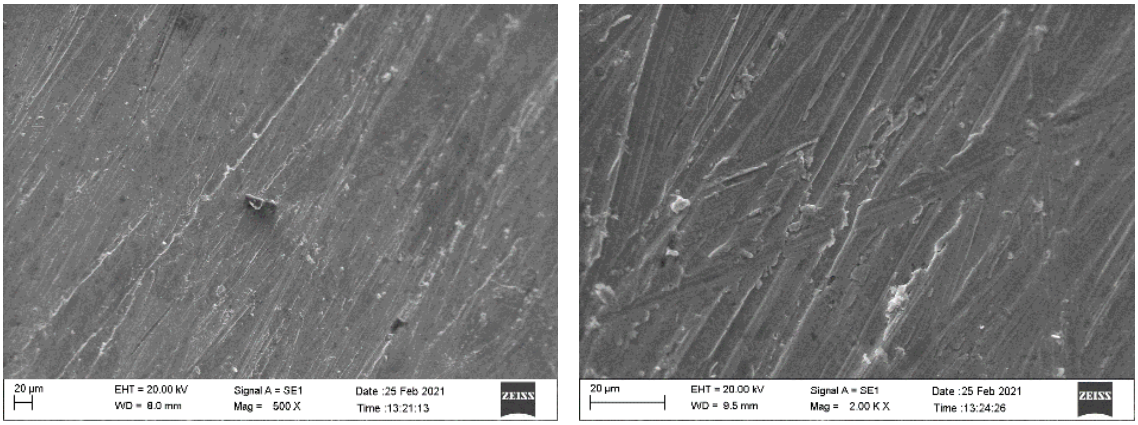

Figure 4.12. The SEM images of the PCI-5 sample

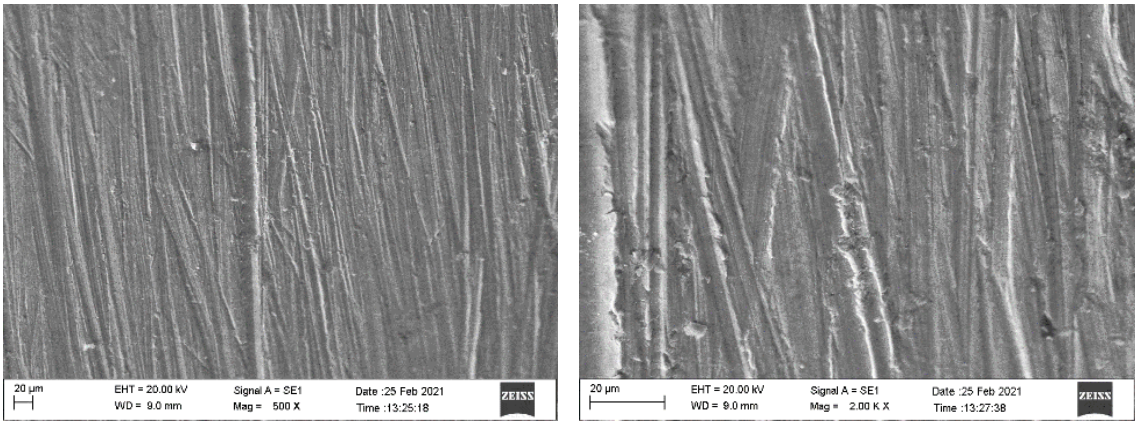

Figure 4.13. The SEM images of the PCI-6 sample

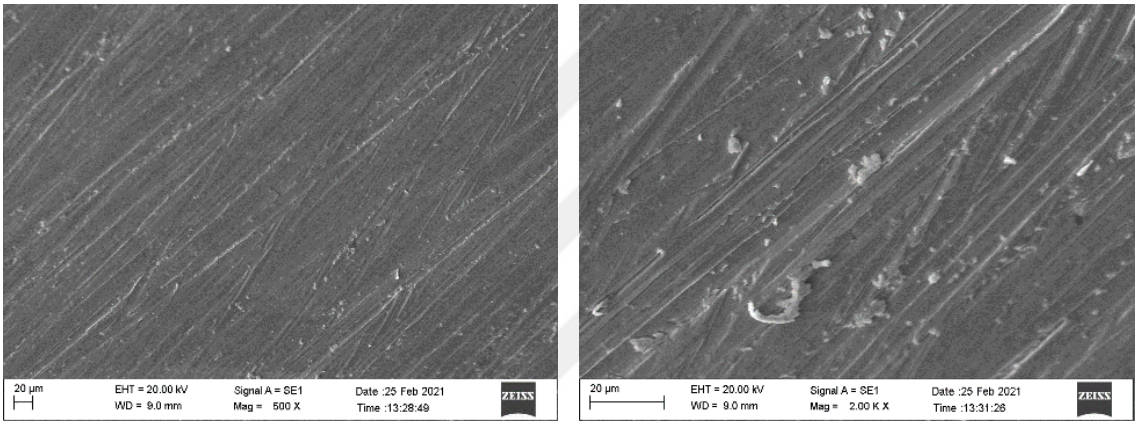

Figure 4.14. The SEM images of the PCI-7 sample

4.3. Crystal Structure Analysis

The X-ray diffraction was performed to crystal structure characterizations at room temperature. Figure 4.22 gives a comparison between all XRD patterns of studied samples. There are also more detailed XRD patterns for each sample separately. According to previous studies, the BCC and/or BCC+FCC phases can be formed more easily with the addition of Al [5, 139]. In addition, the addition of Al content could make BCC phase as reported in AlCoFeMnNi [40], CoFeMnNiAl [38], and AlxCoCrFeNi (x = 0–2) systems [88]. Thus, it is noticeable that Al performs as a stabilizer for the BCC phase, as demonstrated by these three alloy systems. Meanwhile, there is also a B2 phase that appears in the equiatomic AlCoFeMnNi alloy as the XRD pattern is confirmed [38, 40]. It is also agreed by TEM studies [140].

In this research, all samples structure formed the majority of both BCC and FCC phases, while a few more phases were detected in some samples. As it is noticeable from Table 4.2, it can be seen that Ni has the highest negative enthalpy when combined with the other metals in the presented samples. Therefore, there is a probability that all other elements will dissolve into Ni

[39]. The XRD pattern of the PCI-1 sample, which is AlCoFeMnNi alloy shown in Figure 4.15. It verifies that the PCI-1 alloy has the (100) peak at $2\theta \approx 31.4°$ which corresponds to the B2 phase. While both two studies are at as-cast [38, 40] but they have the same peak in that angle. It can be explained through different processing conditions.

Additionally, the PCI-1 sample has some other peaks with different intensities, such as (111) peak at $2\theta \approx 43.5°$ which corresponds to FCC phase, (110) peak at $2\theta \approx 44.2°$, (200) peak at $2\theta \approx 64.1°$, and (211) peak at $2\theta \approx 81.5°$ which these correspond to BCC phase. Besides these, the volume fraction of the BCC phase is more significant than the FCC phase, which can notice through different intensities in the XRD pattern. It also shows that the majority phase is the BCC phase for the presented alloy. Moreover, the calculated crystallite size is 17.1 nm for the PCI-1 sample.

The XRD pattern of the PCI-2 sample, which is $AlCoFeMnNiTi_{10}$ alloy given in Figure 4.16. Furthermore, the PCI-2 sample has some peaks with different intensities, such as (111) peak at $2\theta \approx 43.5°$ which corresponds to FCC phase, (110) peak at $2\theta \approx 44.2°$, and (211) peak at $2\theta \approx 81.5°$ which these corresponds to BCC phase. It should be reported that the lattice parameter of the BCC solid solution phase has a slight improvement based on Bragg's law ($2d \sin\theta = n\lambda$). This is refers to the large atomic radius of Ti (see Table 4.1) as compared to other elements [141]. Besides, the calculated crystallite size is 25.6 nm for the PCI-2 sample.

Figure 4.17 represents the XRD pattern of the PCI-3 sample, which is $AlCoFeMnNiCr_{10}$ alloy. The PCI-3 sample also has some peaks with different intensities, such as (111) peak at $2\theta \approx 43.5°$ which corresponds to FCC phase, (110) peak at $2\theta \approx 44.2°$, (200) peak at $2\theta \approx 64.1°$, and (211) peak at $2\theta \approx 81.5°$ which these corresponds to BCC phase. Also, the calculated crystallite size is 19.99 nm for the PCI-3 sample.

Figure 4.18 shows the XRD pattern of the PCI-4 sample, which is $AlCoFeMnNiSn_{10}$ alloy. Moreover, the PCI-4 sample has some peaks with different intensities, such as (111) peak at $2\theta \approx 43.5°$ which corresponds to FCC phase, (110) peak at $2\theta \approx 44.2°$, (200) peak at $2\theta \approx 64.1°$, and (211) peak at $2\theta \approx 81.5°$ which these corresponds to BCC phase. Besides the coexistence of BCC and FCC phases, Co2MnSn phase also appears in alloys containing Sn [38] as noticed like (311) peak at $2\theta \approx 48.9°$ and (420) peak at $2\theta \approx 71.4°$. Further, the calculated crystallite size is 30.67 nm for the PCI-4 sample. Remarkably, it has a high value of crystallite size as compared to other produced samples, and this refers to the large atomic radius of Sn (see Table 4.1) as compared to other components which the PCI-4 sample contains.

Figure 4.19 represents the XRD pattern of the PCI-5 sample, which is $AlCoFeMnNiV_{10}$ alloy. Additionally, the PCI-5 sample has some peaks with different intensities, such as (111) peak at $2\theta \approx 43.5°$ which corresponds to FCC phase, (110) peak at $2\theta \approx 44.2°$, (200) peak at $2\theta \approx$

64.1°, and (211) peak at $2\theta \approx 81.5°$ which these corresponds to BCC phase. Further, the calculated crystallite size is 28.63 nm for the PCI-5 sample.

Figure 4.20 represents the XRD pattern of the PCI-6 sample, which is $AlCoFeMnNiHf_{10}$ alloy. It approves that the PCI-6 alloy has (100) peak at $2\theta \approx 31.4°$ which corresponds to the B2 phase. While the B2 phase was absent in some of the presented samples, and it has the same peak in that angle with PCI-1 and PCI-7. Besides, the PCI-6 sample has some other peaks with different intensities, such as (111) peak at $2\theta \approx 43.5°$ which corresponds to FCC phase, (110) peak at $2\theta \approx 44.2°$, (200) peak at $2\theta \approx 64.1°$, and (211) peak at $2\theta \approx 81.5°$ which these correspond to BCC phase. Also, some other peaks appear, which refers to the second phases of other peaks. Therefore, while searching for HEAs candidates for magnetic applications, we couldn't reach any alloy which contains Hf. Further, the calculated crystallite size is 17.02 nm for the PCI-6 sample.

The XRD pattern of the PCI-7 sample, which is $AlCoFeMnNiGa_{10}$ alloy given in Figure 4.21. The PCI-7 alloy has a (100) peak at $2\theta \approx 31.4°$ which corresponds to the B2 phase. Besides, the PCI-7 sample has some other peaks with different intensities, such as (111) peak at $2\theta \approx 43.5°$ which corresponds to FCC phase, (110) peak at $2\theta \approx 44.2°$, (200) peak at $2\theta \approx 64.1°$, and (211) peak at $2\theta \approx 81.5°$ which these correspond to BCC phase. Besides, the calculated crystallite size is 18.66 nm for the PCI-7 sample.

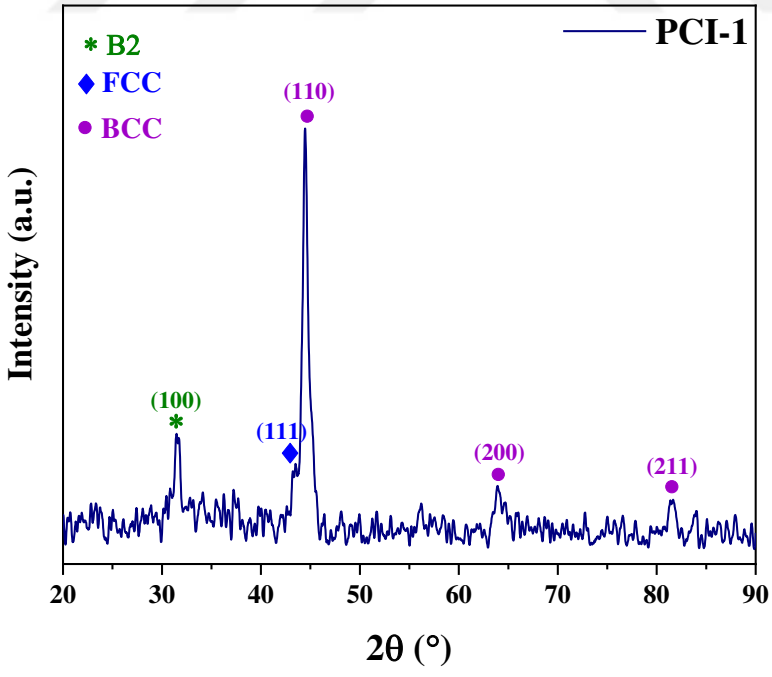

Figure 4.15. XRD pattern of the PCI-1 sample

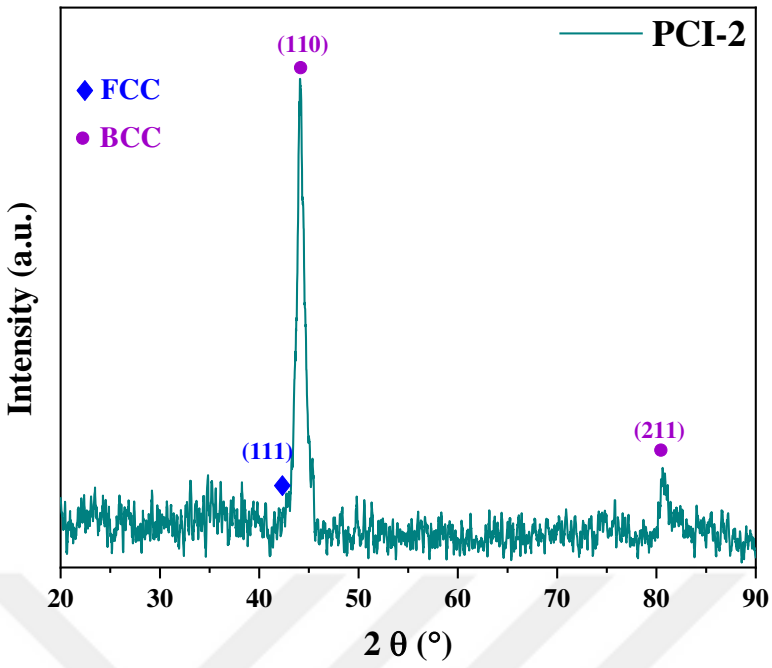

Figure 4.16. XRD pattern of the PCI-2 sample

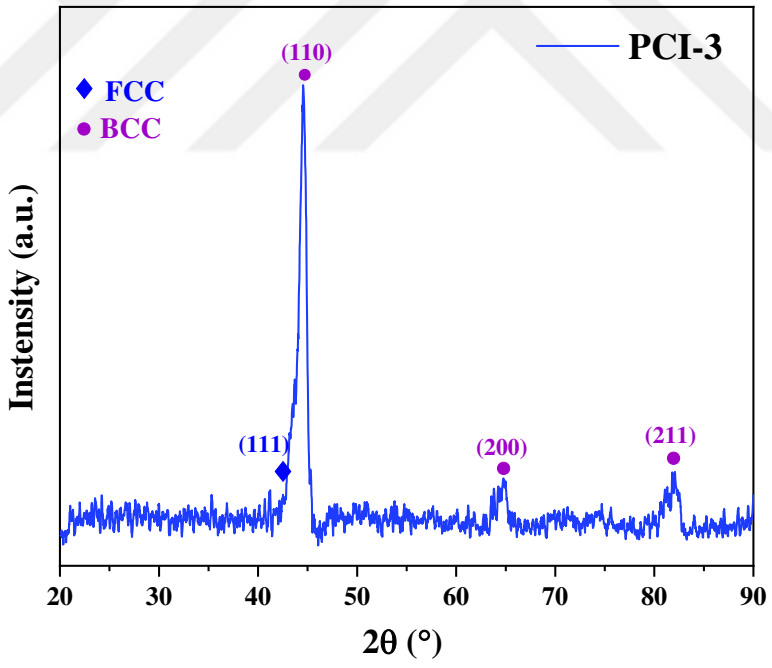

Figure 4.17. XRD pattern of the PCI-3 sample

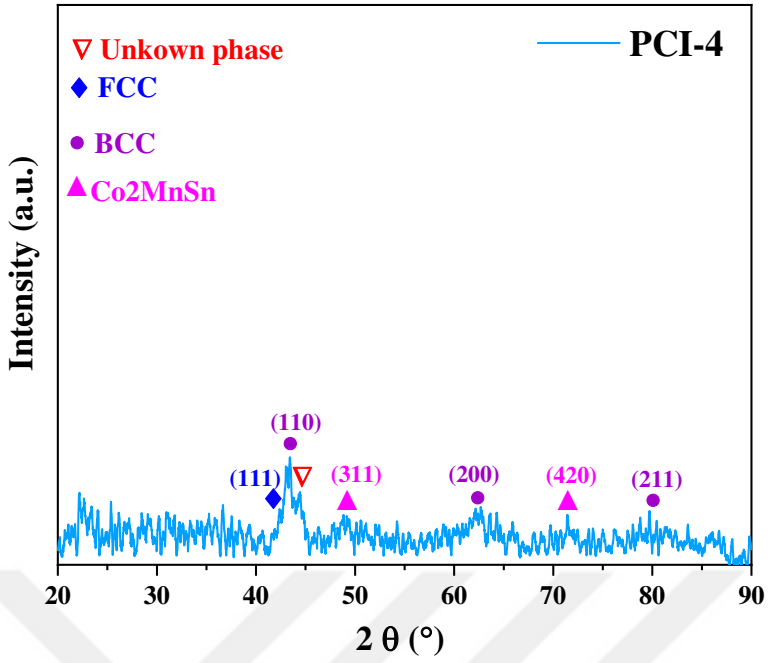

Figure 4.18. XRD pattern of the PCI-4 sample

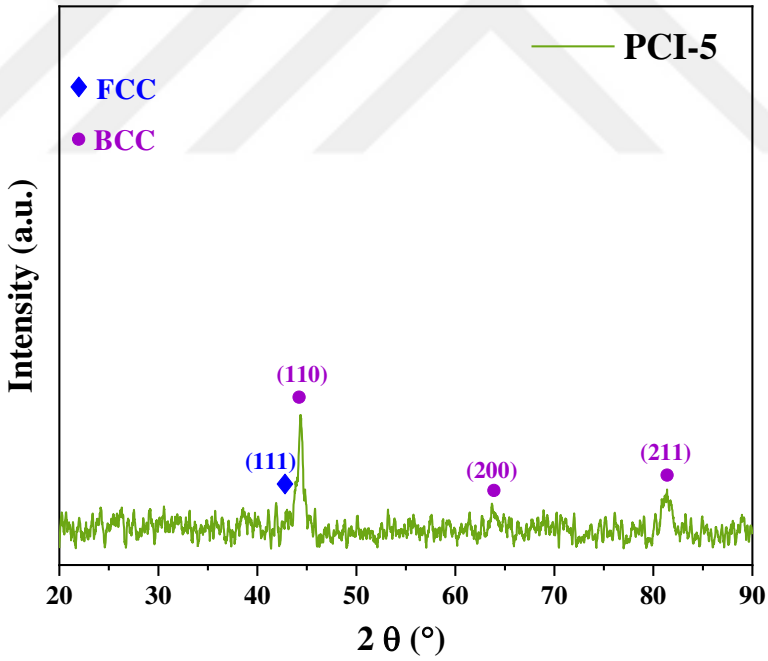

Figure 4.19. XRD pattern of the PCI-5 sample

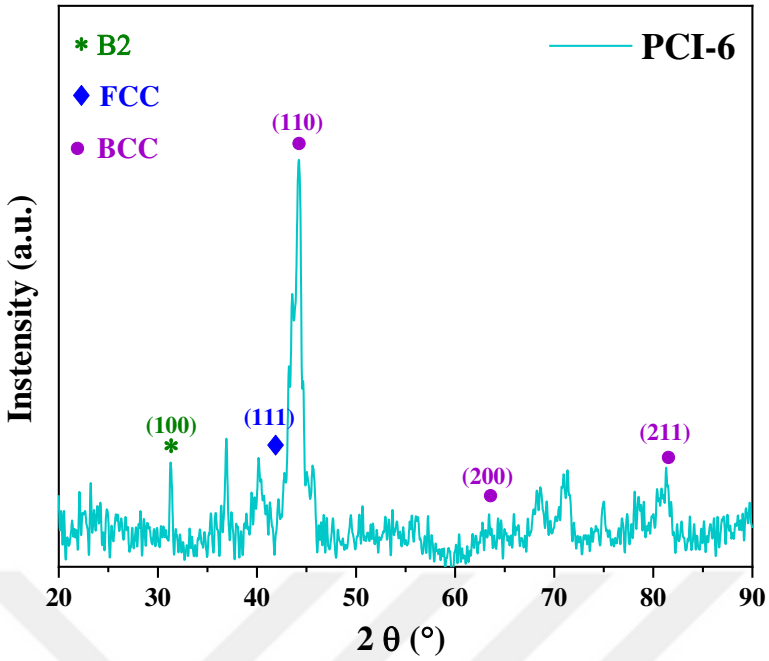

Figure 4.20. XRD pattern of the PCI-6 sample

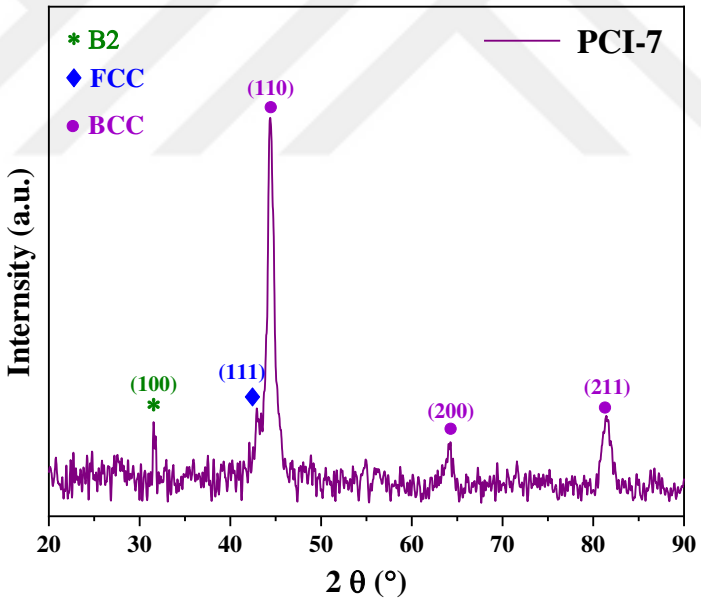

Figure 4.21. XRD pattern of the PCI-7 sample

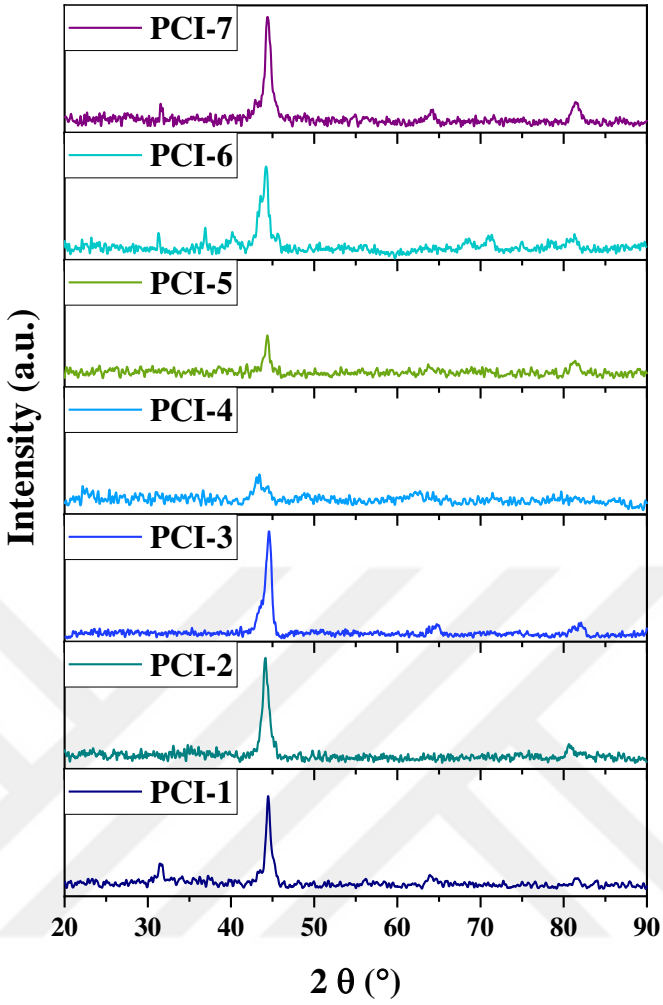

Figure 4.22. A comparison between XRD patterns of all studied samples

4.4. VSM Results

The VSM analyses were performed at room temperature to examine the magnetic applicability of the fabricated alloys. Magnetic properties should be studied through two parameters which are magnetic saturation (M_s) and coercivity (H_c). M_s value mainly depends on the composition of alloys and the crystal structure of HEA [34, 37]. The three ferromagnetic elements (i.e., Fe, Co, Ni) in 60 at.% were used in producing AlCoFeMnNi alloy to get better magnetic properties. The addition of aluminium (Al) to CoFeNi alloys enhanced yield strength and hardness while decreasing magnetic saturation [142]. Al doping also could give ductility to the alloy [143].

Furthermore, Zhong et al. reported that the phase fraction of BCC or FCC could control the magnetic behaviours [144]. Hariharan et al. recommended that the magnetic saturation should be improved through the BCC phase in the first generation of HEAs [40]. Using the DFT, the simulation outcomes show that the Al addition into FeCoNi alloy guides the transformation from FCC to BCC+B2 structure of the alloy [145]. On the other hand, Mishra et al. reported that the

doping of Al for Mn contains HEAs to get excellent magnetic properties [39]. In CoFeNiMn alloy, to limit the antiferromagnetic arranging of Mn atoms, it is investigated M_s value from 18.14 to 148.7 emu/g when Al was added [38]. Adding Al causes a significant shift in an Mn dominant spin peak from above to below the Fermi level due to a change in order from anti-ferromagnetic to ferromagnetic, which has a substantial impact on AlCoFeMnNi's magnetization [38].

In addition, compared with literature studies, all studied samples are listed in Table 4.5 with some similar previous works in their route, Phases, M_s, and H_c values. As we mentioned above, Zuo et al. presented that the Al doping is disapproving the anti-ferromagnetic of Mn [38]. Now it is significantly noticeable from the alloys mentioned in Table 4.5. For instance, CoNiMnGa and FeCoNiMn alloys have lower magnetization than AlCoFeMnNi, and it is due to the anti-ferromagnetic coupling of Mn.

Alloys containing Mn have a lower M_s value than CoFeMn alloy with the excellent M_s value of 155.7 emu/g [142]. For example, CoFeMnNi alloy was studied firstly by Zuo et al. that observed 18.14 emu/g and 1.5 Oe for $M_s$and H_c values, respectively [38]. It was also examined by Hariharan et al., which gets M_s and H_c values of 18.8 emu/g and 10.5 Oe for Al0 (CoFeMnNi) alloy [40]. This is due to the anti-ferromagnetic coupling of Mn with these ferromagnetic elements (Co, Fe, Ni) [38]. Another reason for getting the highest magnetisation value for CoFeNi alloy is that alloy includes 100 at.% of ferromagnetic elements [146]. Above all these, the compared alloys (the first eight rows in Table 4.5) show the difference of crystal structure (phases and if they are homogenized or not) which also remarkably affects the magnetic saturation [40, 144, 145]. Experimental evidence confirms results from first-principle calculations made in the CoFeNi(AlMn)x (x= 0 – 2) system, which show that Mn atoms convert from anti-ferromagnetic to ferromagnetic order when the structure shifts from an FCC to BCC phase [145, 146]. The presented sample (first alloy: PCI-1) has a greater H_c value (325.1 Oe) among all compared alloys listed in Table 4.5; it also has a better M_s amount of 141.1 emu/g (see Figure 4.23) among the six mentioned alloys. But it has lower magnetization as compare to AlCoFeMnNi (148 emu/g) [38]. This is because of differences in phase fraction and processing conditions. Regardless of what phase structure the alloying elements have, non-magnetic components can effectively reduce the magnetization of the CoFeNi alloy [38]. From this, we can clarify that the first alloy (PCI-1) has excellent magnetic saturation compared to the other six produced alloys.

The second sample (PCI-2) has better magnetic saturation ($M_s = 84.4$ emu/g) than alloys containing Ti such as TiFeNiCrCo and TiFeNiCrMn [37]. It refers to two main factors. Firstly, the two mentioned alloys include Cr, which negatively affect magnetization [102]. Secondly, the phase of both two alloys was FCC, but the present sample's phase is BCC+FCC. Although, two alloys (TiFeNiCrCo, TiFeNiCrMn) contain some ferromagnetic components (Co, Fe, and Ni). Figure 4.24 shows the M-H curve of the PCI-2 sample. According to Zhang et al. findings, the magnetic

saturation of HEAs is mainly dependent on the crystal structure and chemical composition [34]. As a result, it can be said that for HEAs, the value of M_s is dependent on the presence of magnetic components and improves noticeably as the number of ferromagnetic elements increases [37].

The third alloy (PCI-3) which is $AlCoFeMnNiCr_{10}$ have greater magnetization as compare to four mentioned alloys CoFeMnNiCr [38], CoNiMnCrAl [147], $AlCo_{0.5}Cr_{0.5}FeNi$ [148], AlCoCrFeNi [149]. The M_s value of the PCI-3 sample is 98.33 emu/g (see Figure 4.25), but the M_s quantity of other alloys was between 1.39 emu/g to 64 emu/g. This can be explained through the luck of ferromagnetic elements (Fe in CoNiMnCrAl and low Co composition in $AlCo_{0.5}Cr_{0.5}FeNi$). It also refers to the high ratio of Cr element in CoFeMnNiCr, CoNiMnCrAl, and AlCoCrFeNi alloys which is 20 at.% in all these three alloys, but our current sample has a lower atomic ratio (10 at.%) of Cr element. And it is well known that the highest composition of Cr results in the lower magnetization because it has an anti-parallel magnetic moment with Co, Fe, and Ni [102]. Remarkably, the M_s value of CoFeMnNiCr is the lowest (1.39 emu/g) and this is because of Cr and Mn elements. The Coercivity of presented (PCI-3) sample was found to be 90.65 Oe.

In a comparison of $FeCoNi(CuAl)_{0.8}Sn_{0.1}$ [150] with CoFeMnNiSn [38] alloys, the $FeCoNi(CuAl)_{0.8}Sn_{0.1}$ has better magnetization (88.8 emu/g), which refers to Al addition, phases difference, and ferromagnetic elements ratio. But if we wonder about making a comparison between these two alloys and this current alloy (the fourth alloy: PCI-4), the M_s value of PCI-4 ($AlCoFeMnNiSn_{10}$) is 97.5 emu/g (see Figure 4.26), which is greater than their magnetization value. Firstly, the CoFeMnNiSn doesn't contain the Al element, and $FeCoNi(CuAl)_{0.8}Sn_{0.1}$ has lower Al composition, which helps to improve magnetic saturation by minimizing the role of the Mn element. Secondly, our produced sample has FCC+BCC phases, but the CoFeMnNiSn has BCC+Co_2MnSn phases. Thirdly, this fabricated alloy (PCI-4) has been homogenized (HM) which these two alloys are in as-cast (AC). These three listed points help to analyse differences between our samples and compare alloys.

Compared to the FeCoNiMnV alloy, the fifth sample (PCI-5) is almost the same in phases and magnetizations. The similarity in phases made the similarity in magnetic saturation. Figure 4.27 gives the M-H curve of PCI-5. The present sample's ($AlCoFeMnNiV_{10}$) coercivity became lower (94.1 Oe) than FeCoNiMnV alloy. That could explain through the equiatomic ratio of V in FeCoNiMnV alloy. To get better magnetic saturation, we should make V in equiatomic proportion with all other compositions in our sample (AlCoFeMnNiV10). Even though the M_s value of FeCoNiMnV alloy was 100 emu/g just when it is milled 48 h; otherwise, it has lower magnetization [151]. Moreover, the production techniques were different, we fabricated alloys through arc melting, but the FeCoNiMnV alloy was produced with mechanical alloying. The difference in processing conditions is possibly the cause of this variance [152].

In addition, the sixth sample (PCI-6) has lower magnetization than the rest of the other fabricated alloys. Figure 4.28 reports the M-H curve of the PIC-6 ($AlCoFeMnNiHf_{10}$) sample. It is noticeable that the M-H curve of the PCI-6 sample is different in shape from other curves, which seems like it doesn't get full saturation. Therefore, it might give better results under a higher magnetic field. It also refers to the Hf structure, which makes different phases reported in XRD results. Besides, we couldn't find an alloy containing Hf in the literature for magnetic purposes.

Additionally, the seventh sample (PCI-7) has lower magnetization as compared to AlCoFeMnNi alloy, and it's due to the formation of FCC+BCC phases in the PCI-7 sample. But the PCI-7 ($AlCoFeMnNiGa_{10}$) alloy has better magnetization (see Figure 4.29) than some literature works like $FeCoNi(CuAl)_{0.8}Ga_{0.08}$, CoFeMnNiGa, and $Fe_{0.5}Co_{0.5}$ NiMnGa as mentioned in Table 4.5. And this is referring to Al additions. On the other hand, the coercivity of the presented sample (PCI-7) has been improved compared to all mentioned alloys, which contain Ga elements.

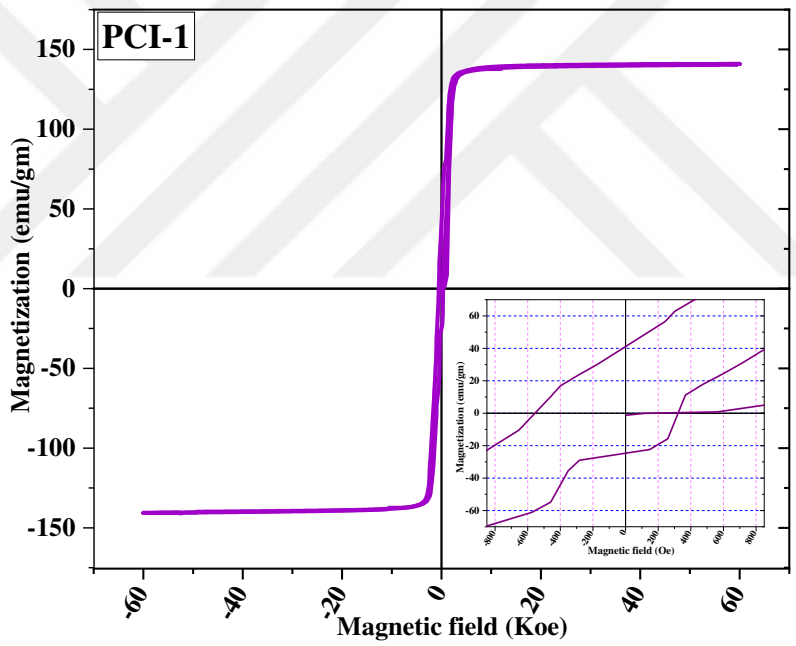

Figure 4.23. Magnetic hysteresis loop of homogenized AlCoFeMnNi (PCI-1) HEA. The magnified picture of the selected region of the M-H curve is shown in the inset

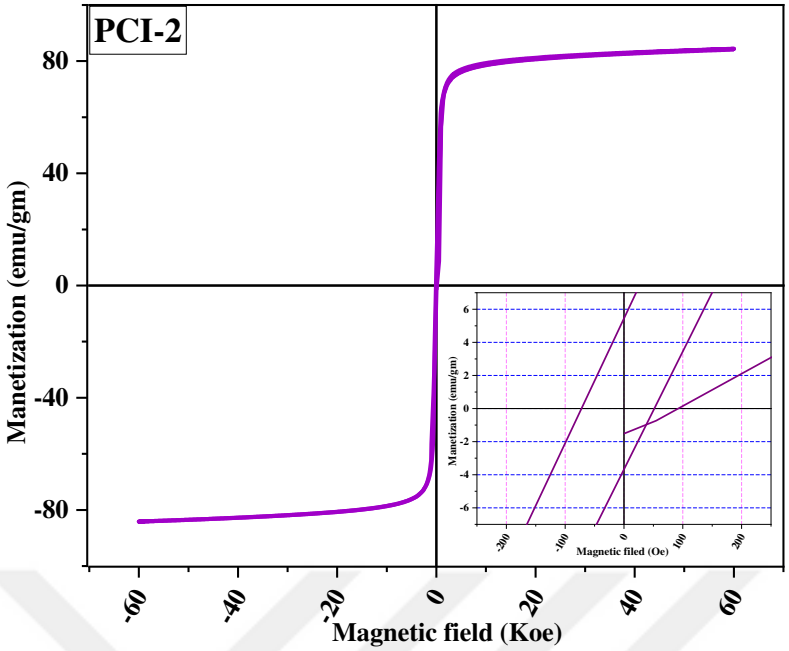

Figure 4.24. Magnetic hysteresis loop of homogenized $AlCoFeMnNiTi_{10}$ (PCI-2) HEA. The magnified picture of the selected region of the M-H curve is shown in the inset

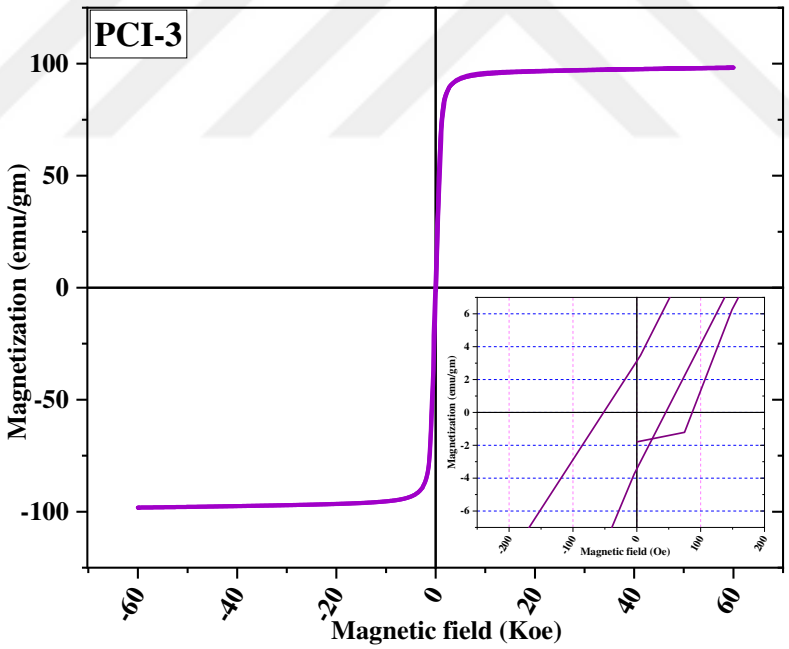

Figure 4.25. Magnetic hysteresis loop of homogenized $AlCoFeMnNiCr_{10}$ (PCI-3) HEA. The magnified picture of the selected region of the M-H curve is shown in the inset

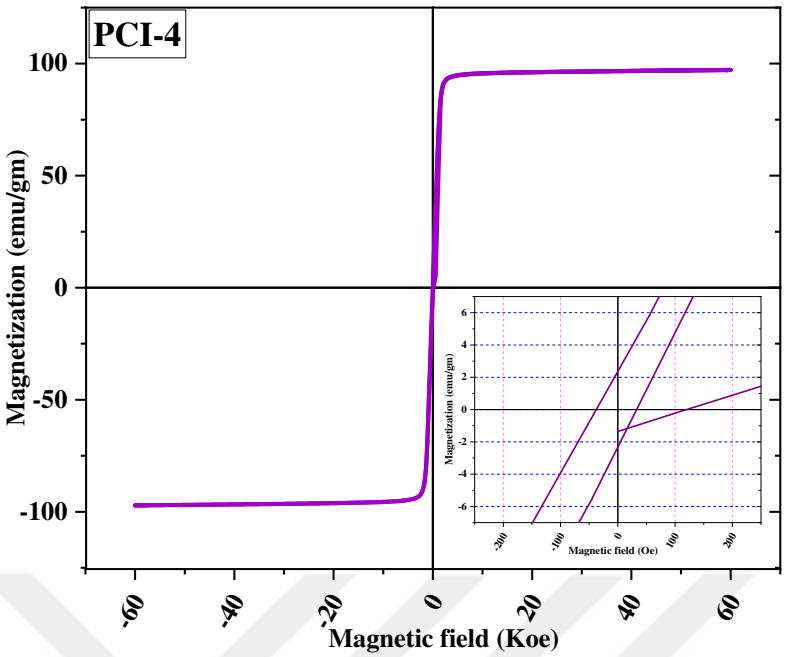

Figure 4.26. Magnetic hysteresis loop of homogenized $AlCoFeMnNiSn_{10}$ (PCI-4) HEA. The magnified picture of the selected region of the M-H curve is shown in the inset

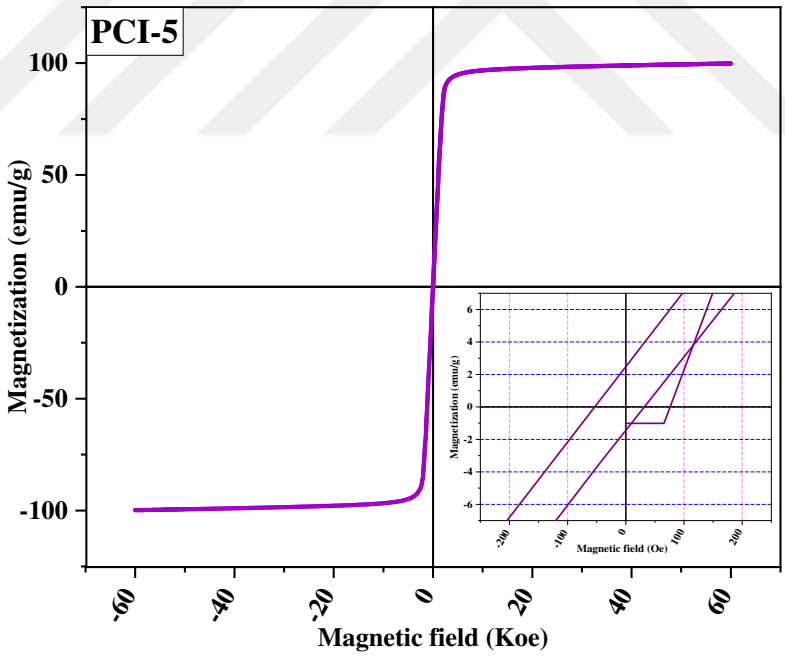

Figure 4.27. Magnetic hysteresis loop of homogenized $AlCoFeMnNiV_{10}$ (PCI-5) HEA. The magnified picture of the selected region of the M-H curve is shown in the inset

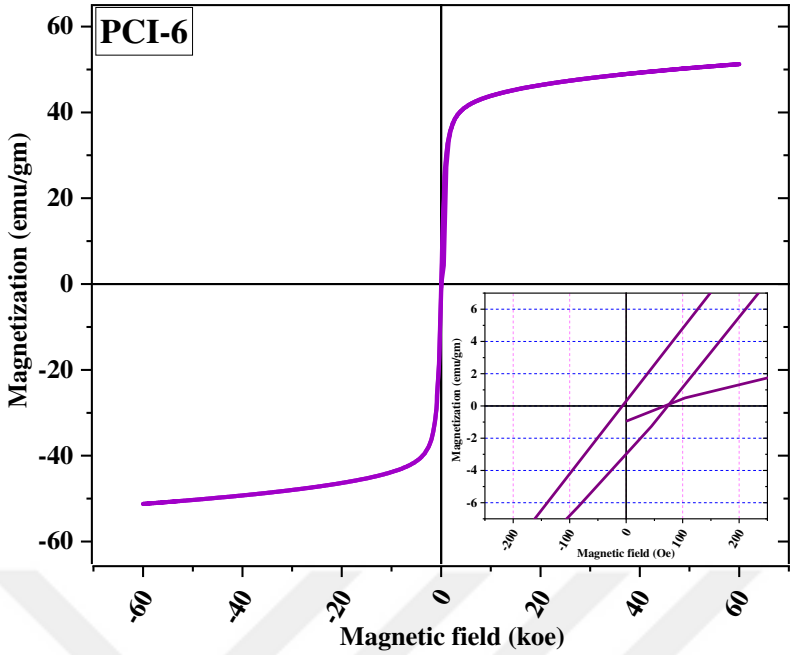

Figure 4.28. Magnetic hysteresis loop of homogenized $AlCoFeMnNiHf_{10}$ (PCI-6) HEA. The magnified picture of the selected region of the M-H curve is shown in the inset

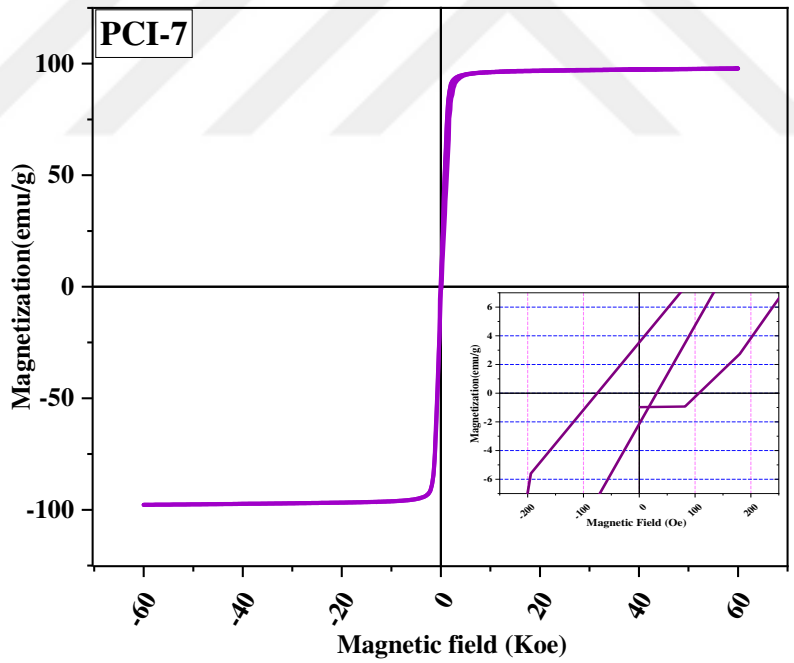

Figure 4.29. Magnetic hysteresis loop of homogenized $AlCoFeMnNiGa_{10}$ (PCI-7) HEA. The magnified picture of the selected region of the M-H curve is shown in the inset

All M-H curves show the hysteresis loop of all homogenized studied samples. The values of M_s and H_c have been reported in a bar chart (Figure 4.30 (a)), which compares magnetization and coercivity between all samples. As a consequence, the highest value of magnetization was determined from PCI-1 alloy, which is 141.1 emu/g but the lowest value of M_s among these seven

Table 4.5. Comparison between High entropy alloys due to magnetic properties, M_s and H_c are symbols for magnetization and coercivity

No.	Alloys	Route	Phase	M_s (emu/g)	H_c (Oe)	References
1	**FeCoNi**	HM	FCC	155.7	2.37	[146]
2	**FeCoNiMn**	AC	FCC	18.14	1.5	[38]
3	**AlCoFeMnNi**	AC	BCC+B2	148	8	[38]
4	**AlCoFeMnNi**	HM	BCC+FCC+B2	141.1	325.1	Current study
5	**$FeCoNiMn_1Al_1$**	HM	BCC	132.2	3.34	[146]
6	**$FeCoNiMn_{0.25}Al_{0.25}$**	AC	FCC	101	3.36	[33]
7	**AlCoFeMnNi**	HM	BCC+FCC	94	5	[40]
8	**$Al_{0.7}$CoFeMnNi**	HM	BCC+FCC	60	10	[40]
9	**TiFeNiCrMn**	AC	FCC	2.28	225.8	[37]
10	**TiFeNiCrCo**	AC	FCC	24.44	149.5	[37]
11	**$AlCoFeMnNiTi_{10}$**	HM	B2+BCC+FCC	84.4	100.9	Current study
12	**AlCoCrFeNi**	AC	BCC	64	52	[149]
13	**$AlCo_{0.5}Cr_{0.5}FeNi$**	HM	BCC+B2	46	96	[148]
14	**$AlCoFeMnNiCr_{10}$**	HM	BCC+FCC	98.33	90.6	Current study
15	**CoFeMnNiCr**	AC	FCC	1.39	135.8	[38]
16	**CoNiMnCrAl**	AC	BCC+FCC	31.23	39.2	[147]
17	**CoFeMnNiSn**	AC	BCC+Co2MnSn	80.29	43.1	[38]
18	**$AlCoFeMnNiSn_{10}$**	HM	BCC+FCC+Co_2MnSn	97.5	127.8	Curent study
19	**$FeCoNi(CuAl)_{0.8}Sn_{0.1}$**	AC	BCC+FCC	88.8	12.8	[150]
20	**FeCoNiMnV**	HM	BCC+FCC	100	150	[151]
21	**$AlCoFeMnNiV_{10}$**	HM	BCC+FCC	99.88	94.1	Current study
22	**$AlCoFeMnNiHf_{10}$**	HM	B2+BCC+FCC	51.2	78.6	Current study
23	**CoNiMnGa**	AC	BCC	115.92	27.9	[153]
24	**$AlCoFeMnNiGa_{10}$**	HM	B2+BCC+FCC	97.83	116.7	Current study
25	**$FeCoNi(CuAl)_{0.8}Ga_{0.08}$**	AC	BCC+FCC	82.8	8.6	[154]
26	**CoFeMnNiGa**	AC	BCC+FCC	80.43	11.5	[38]
27	**$Fe_{0.5}Co_{0.5}$ NiMnGa**	AC	BCC	78.48	27.4	[153]

AC: as-cast, HM: homogenized

alloys studied in that research was 51.2 emu/g for PCI-6 alloy. Besides, the Coercivity value gets the lowest value with Hf addition (PCI-6 alloy) which is 78.63 Oe, but the H_c value is 325.1 Oe for PCI-1 alloy among these tested samples. It needs more attention to notice that the hysteresis curve of PCI-2 and PCI-6 with lower magnetization is still linearly increasing around +60 Koe, which means they aren't fully saturated. But it is getting stable (i.e., the constant value of M_S) for the rest of the alloys, which means they got semi-full saturation. The hysteresis was low for all samples. In

addition, samples were obtained magnetic saturation, and they are all should count as ferromagnetic alloys. Besides, the coercivity of tested alloys was between 78 Oe and 325 Oe that led to counting these alloys as semi-hard magnetic material. Moreover, the magnetic resonance (M_r) is the magnitude of magnetization when the applied field is zero. The M_r values were 41.3 emu/g, 5.55 emu/g, 3.5 emu/g, 2.9 emu/g, 2.53 emu/g, 0.53 emu/g, and 4.2 emu/g for PCI-1, PCI-2, PCI-3, PCI-4, PCI-5, PCI-6, and PCI-7 alloy, respectively. Figure 4.30 (b) shows the remanence ratio (M_r/M_s) in % for all studied alloys in a bar chat. Remarkably, the PCI-1 has the highest value in remanence ratio among other alloys.

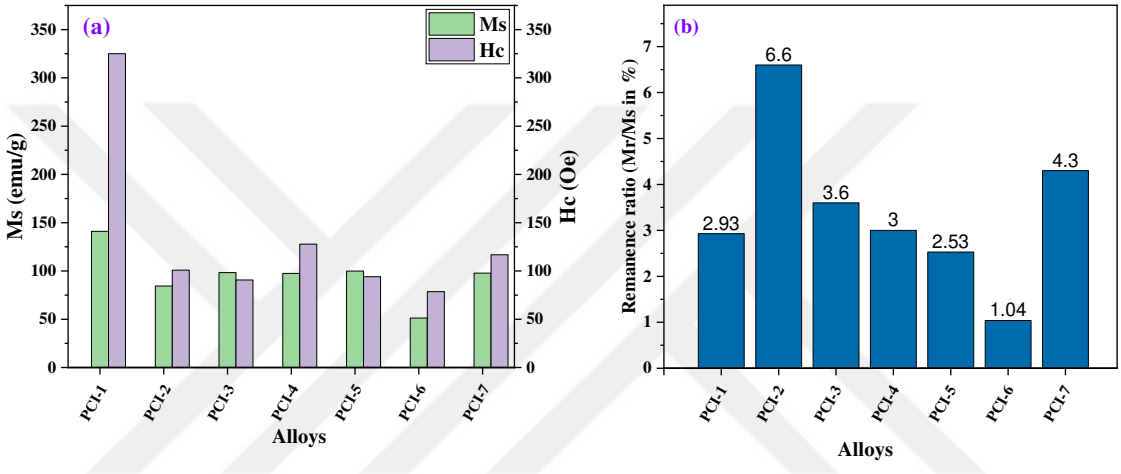

Figure 4.30. A comparison between all produced samples based on (a) magnetization (M_s) and coercivity (H_c), (b) Remanence ratio (M_r/M_s) in %

4.5. DTA Measurements

Temperature and heat energy intake are factoring that thermal analysis considers when determining a material's structure, whether it is degrading or not. Therefore, the samples' transitions in a solid-state phase could be observed. Analyses were performed using DTA, and phase alterations within the structure were determined. All details of the experimental procedure were reported before (see section 3.3.4). Furthermore, endothermic (downward) and exothermic (upward) reactions were going inside the structure, and multiple reactions were noted on the structure itself.

Figure 4.31 shows the DTA curve of PCI-1 alloy, and it is noticeable that there are two phase transitions. Two exothermic peaks could find around 250 °C and 540 °C. Thus, there is a phase transition between 270 °C and 500 °C, another one also observed between 590 °C and 700 °C. The DTA result of PCI-2 alloy is shown in Figure 4.32, and remarkably there are two endothermic peaks around 400 °C and 700 °C. Figure 4.33 gives a DTA curve of PCI-3 alloy, and it has two endothermic peaks around 450 °C and 600 °C. The DTA curve of PCI-4 alloy is shown in Figure

4.34, and it can observe a phase transition between 400 °C and 500 °C and an endothermic peak found around 640 °C. Figure 4.35 presents the DTA curve of PCI-5 alloy, and it has an endothermic peak around 600 °C. Figure 4.36 shows the DTA curve of PCI-6 alloy, and Figure 4.37 shows the DTA curve of PCI-7 alloy. Both of them have phase transitions between 400 °C and 600 °C. Figure 4.38 shows the DTA curves of all samples. It can detect a slight change in phase transitions between alloys, and all samples get oxidation around 700 °C. After oxidation, the samples take less heat than before, as lines in a graph show it also.

Whereas the samples' Al and Ni alloying components exhibit BCC structures, the elements Fe and Mn exhibit FCC structures and create a metastable B2 ordered solid solution in the alloy [155, 156]. A sequential B2 phase transition is expected to occur when these phase transitions are considered eutectic transitions. In addition, the determining melting points are 1416.1 K, 1389.3 K, and 1346.4 K for CoNiMnGa, $Fe_{0.5}Co_{0.5}$NiMnGa, and FeNiMnGa alloys, respectively [153]. When Co is added, the melting point rises, but Fe decreases the melting point slightly. This shows that Co has a greater connection with other elements than Fe does [153].

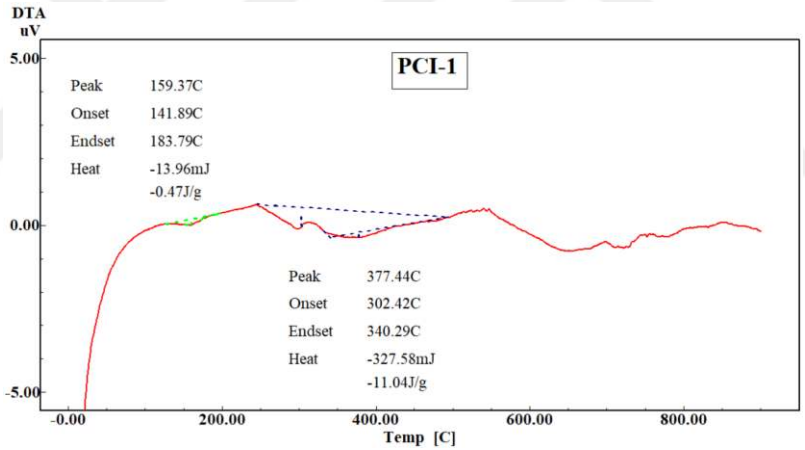

Figure 4.31. DTA curve of the PCI-1 sample with heating/cooling rates of 20 °C/min

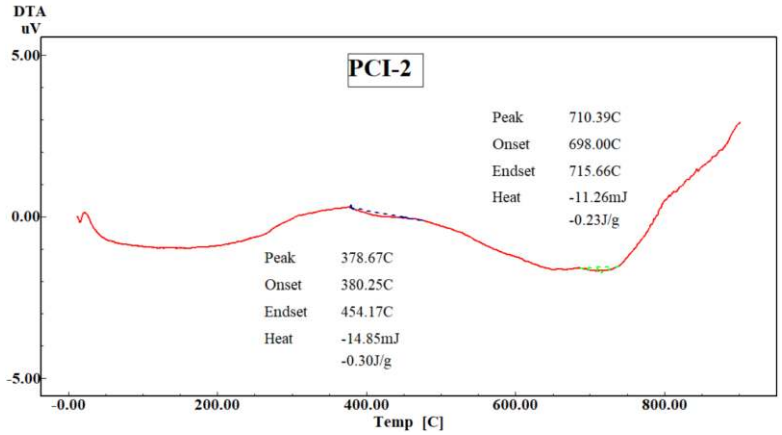

Figure 4.32. DTA curve of the PCI-2 sample with heating/cooling rates of 20 °C/min

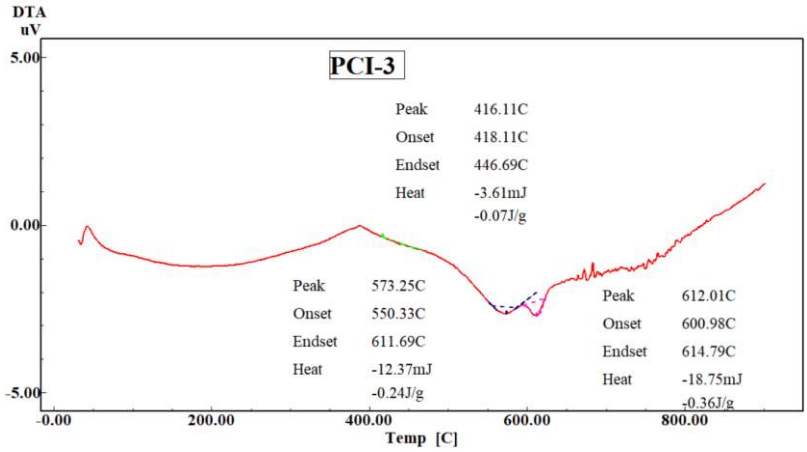

Figure 4.33. DTA curve of the PCI-3 sample with heating/cooling rates of 20 °C/min

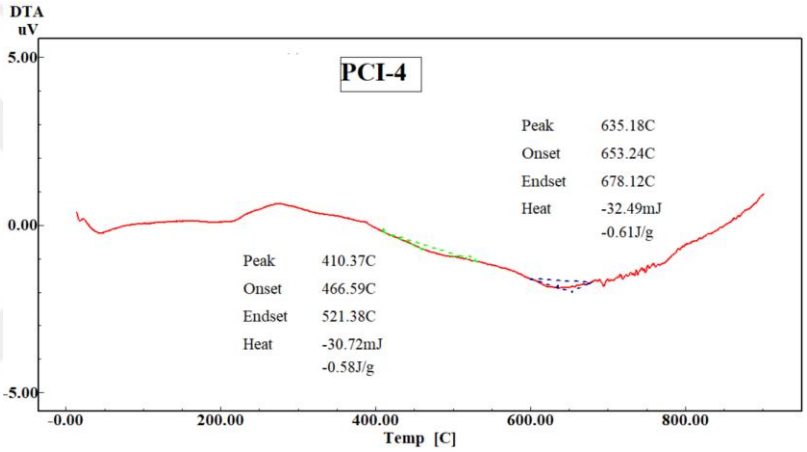

Figure 4.34. DTA curve of the PCI-4 sample with heating/cooling rates of 20 °C/min

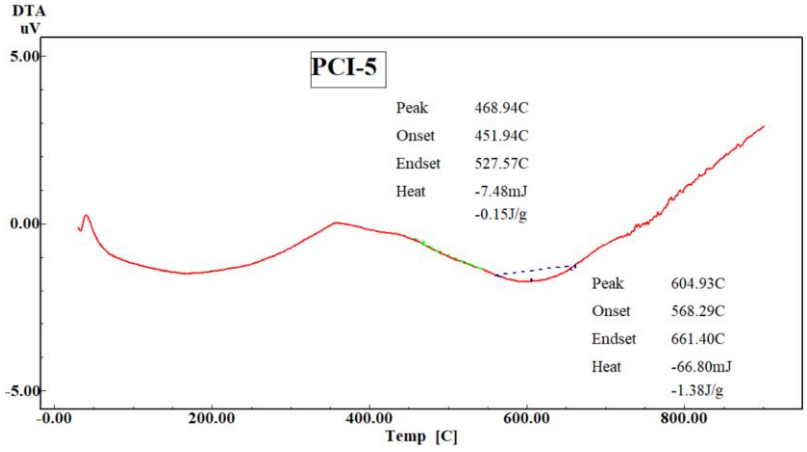

Figure 4.35. DTA curve of the PCI-5 sample with heating/cooling rates of 20 °C/min

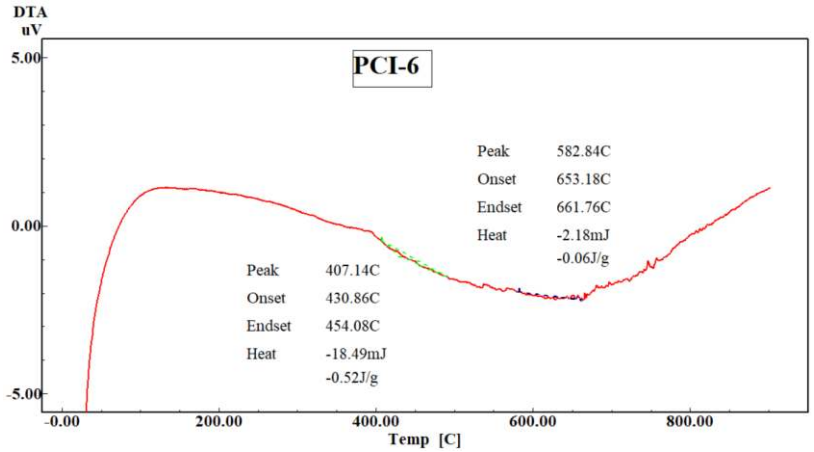

Figure 4.36. DTA curve of the PCI-6 sample with heating/cooling rates of 20 °C/min

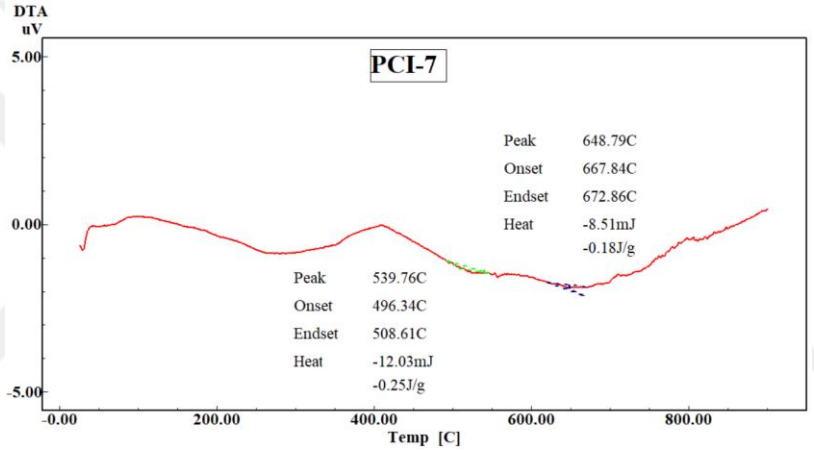

Figure 4.37. DTA curve of the PCI-7 sample with heating/cooling rates of 20 °C/min

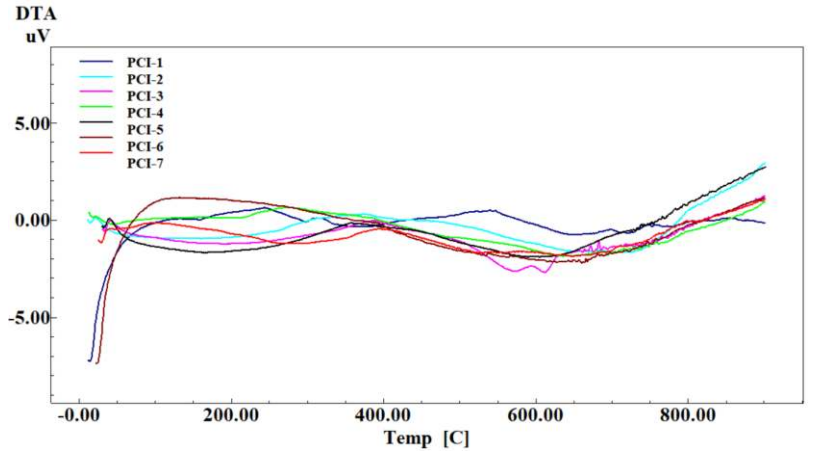

Figure 4.38. DTA curves of all samples with heating/cooling rates of 20 °C/min

5. CONCLUSION

To sum up, this study enlightens the significant role of different element additions to AlCoFeMnNi equiatomic alloy on the microstructure and magnetic characteristics. First of all, the seven samples, which include $Al_{20}Co_{20}Fe_{20}Mn_{20}Ni_{20}$ and $Al_{18}Co_{18}Fe_{18}Mn_{18}Ni_{18}X_{10}$ (X: Ti, Cr, Sn, V, Hf, Ga) fabricated through arc melting with new compositions. Secondly, all samples were homogenized with an arc melting furnace through the remelting process. Thirdly, several basic calculations were done using obtained results and theoretical mathematical models, such as the configurational entropy, mixing enthalpy, valence electron concentration, and melting temperature. Fourthly, several characterization techniques were performed with different purposes. Then, the most remarkable outcomes of this research should list as follows:

Based on EDX-SEM results:

- ✓ EDX values closely follow nominal compositions for all tested samples.
- ✓ There aren't any holes in the surfaces. The bulk defect (pores) does not occur because the arc melting furnace dissolves all of the elements, the bulk defect (pores) does not occur.

From XRD measurements:

- ✓ All produced samples contain BCC and FCC phases. Further, the BCC phase is the primary phase in all of them.
- ✓ Meanwhile, there is also the observation of the B2 phase (<100> peak at $2\theta \approx 31.4°$) in $Al_{20}Co_{20}Fe_{20}Mn_{20}Ni_{20}$, $Al_{18}Co_{18}Fe_{18}Mn_{18}Ni_{18}Hf_{10}$, and $Al_{18}Co_{18}Fe_{18}Mn_{18}Ni_{18}Ga_{10}$ alloys.
- ✓ It should detect that from the XRD pattern, the Co2MnSn phase is also available in two angles for the $Al_{18}Co_{18}Fe_{18}Mn_{18}Ni_{18}Sn_{10}$ sample.
- ✓ The calculated crystallite size ranges between 17.1 nm and 31 nm for all samples.

Due to VSM characterizations:

- ✓ The equiatomic AlCoFeMnNi alloy has better magnetization ($M_s = 141.1\ emu/g$) among all fabricated alloys. In other words, that means these elements (Ti, Cr, Sn, V, Hf, Ga) additions to AlCoFeMnNi negatively influenced the magnetic properties of samples.
- ✓ Besides, the lowest value of M_s ($51.2\ emu/g$) was obtained through Hf addition ($Al_{18}Co_{18}Fe_{18}Mn_{18}Ni_{18}Hf_{10}$) to the base alloy.
- ✓ The coercivity of samples was in the range of 78 Oe to 325 Oe. Thus, the samples are good candidates for soft magnetic applications.
- ✓ The hysteresis of samples is low. The presented alloys also show ferromagnetic behaviour.

As outcomes from DTA analysis:

- ✓ The DTA curves of the samples show a solid-state transition around 400 °C and 600 °C.
- ✓ The results of DTA tests confirm that the samples have BCC and FCC structures.

REFERENCES

[1] Davis, J.R., (2001). *Alloying: understanding the basics*, ASM international, USA

[2] Praveen, S. and Kim, H.S. (2018). High-Entropy Alloys: Potential Candidates for High-Temperature Applications–An Overview, *Advanced Engineering Materials*, 20 (1700645), pp: 1-22. doi: 10.1002/adem.201700645.

[3] Yeh, J.W., Chen, Y.L., Lin, S.J., and Chen, S.K. (2007). High-entropy alloys–a new era of exploitation. in *Materials Science Forum*. Trans Tech Publ.

[4] Jien-Wei, Y. (2006). Recent progress in high entropy alloys, *Ann. Chim. Sci. Mat*, 31 (6), pp: 633-648. doi: 10.3166/acsm.31.633-648.

[5] Tsai, M.-H. and Yeh, J.-W. (2014). High-entropy alloys: a critical review, *Materials Research Letters*, 2 (3), pp: 107-123. doi: 10.1080/21663831.2014.912690.

[6] Murty, B.S., Yeh, J.-W., Ranganathan, S., and Bhattacharjee, P., (2019). *High-entropy alloys*, Elsevier, Amesterdam

[7] Yeh, J.-W. (2013). Alloy design strategies and future trends in high-entropy alloys, *The Minerals, Metals & Materials Society*, 65 (12), pp: 1759-1771. doi: 10.1007/s11837-013-0761-6.

[8] Zhang, Y., (2019). *High-Entropy Materials*, Springer, Singapore

[9] Pickering, E. and Jones, N. (2016). High-entropy alloys: a critical assessment of their founding principles and future prospects, *International Materials Reviews* 61 (3), pp: 183-202.

[10] Zhang, Y., Yang, X., and Liaw, P. (2012). Alloy design and properties optimization of high-entropy alloys, *The Minerals, Metals & Materials Society*, 64 (7), pp: 830-838.

[11] Ye, Y., Wang, Q., Lu, J., Liu, C., and Yang, Y. (2016). High-entropy alloy: challenges and prospects, *Materials today*, 19 (6), pp: 349-362.

[12] Yeh, J.W., Chen, S.K., Lin, S.J., Gan, J.Y., Chin, T.S., Shun, T.T., Tsau, C.H., and Chang, S.Y. (2004). Nanostructured high-entropy alloys with multiple principal elements: novel alloy design concepts and outcomes, *Advanced Engineering Materials*, 6 (5), pp: 299-303.

[13] Yana, X. and Zhang, Y. (2020). Functional properties and promising applications of high entropy alloys, *Scripta Materialia*, 187, pp: 188-193. doi: 10.1016/j.scriptamat.2020.06.017.

[14] Zhang, W., Liaw, P.K., and Zhang, Y. (2018). Science and technology in high-entropy alloys, *Science China Materials*, 61 (1), pp: 2-22.

[15] Zhang, Y., Zuo, T.T., Tang, Z., Gao, M.C., Dahmen, K.A., Liaw, P.K., and Lu, Z.P. (2014). Microstructures and properties of high-entropy alloys, *Progress in Materials Science*, 61, pp: 1-93. doi: 10.1016/j.pmatsci.2013.10.001.

[16] Jin, X., Bi, J., Zhang, L., Zhou, Y., Du, X., Liang, Y., and Li, B. (2019). A new CrFeNi2Al eutectic high entropy alloy system with excellent mechanical properties, *Journal of Alloys and Compounds*, 770, pp: 655-661. doi: 10.1016/j.jallcom.2018.08.176.

[17] Otto, F., Yang, Y., Bei, H., and George, E.P. (2013). Relative effects of enthalpy and entropy on the phase stability of equiatomic high-entropy alloys, *Acta Materialia*, 61 (7), pp: 2628-2638. doi: 10.1016/j.actamat.2013.01.042.

[18] Koželj, P., Vrtnik, S., Jelen, A., Jazbec, S., Jagličić, Z., Maiti, S., Feuerbacher, M., Steurer, W., and Dolinšek, J. (2014). Discovery of a superconducting high-entropy alloy, *Physical review letters*, 113 (10), pp: 1-5. doi: 10.1103/PhysRevLett.113.107001.

[19] He, Q., Ding, Z., Ye, Y., and Yang, Y. (2017). Design of high-entropy alloy: a perspective from nonideal mixing, *The Minerals, Metals & Materials Society*, 69 (11), pp: 2092-2098. doi: 10.1007/s11837-017-2452-1.

[20] Cantor, B., Chang, I., Knight, P., and Vincent, A. (2004). Microstructural development in equiatomic multicomponent alloys, *Materials Science and Engineering: A,* 375, pp: 213-218.

[21] Ibrahim, P.A., Özkul, İ., and Canbay, C.A. (2021). Methodological Research of High Entropy Alloys by Using Bibliometrics Analysis, *JOURNAL OF MATERIALS AND ELECTRONIC DEVICES*, 5 (1), pp: 7-13.

[22] Chuang, M.-H., Tsai, M.-H., Wang, W.-R., Lin, S.-J., and Yeh, J.-W. (2011). Microstructure and wear behavior of AlxCo1. 5CrFeNi1. 5Tiy high-entropy alloys, *Acta Materialia*, 59 (16), pp: 6308-6317. doi: 10.1016/j.actamat.2011.06.041.

[23] Lin, C.-M. and Tsai, H.-L. (2011). Evolution of microstructure, hardness, and corrosion properties of high-entropy Al0. 5CoCrFeNi alloy, *Intermetallics*, 19 (3), pp: 288-294. doi: 10.1016/j.intermet.2010.10.008.

[24] Gludovatz, B., Hohenwarter, A., Catoor, D., Chang, E.H., George, E.P., and Ritchie, R.O. (2014). A fracture-resistant high-entropy alloy for cryogenic applications, *Science*, 345 (6201), pp: 1153-1158.

[25] Senkov, O., Scott, J., Senkova, S., Meisenkothen, F., Miracle, D., and Woodward, C. (2012). Microstructure and elevated temperature properties of a refractory TaNbHfZrTi alloy, *Journal of materials Science*, 47 (9), pp: 4062-4074.

[26] Huang, S., Li, W., Li, X., Schönecker, S., Bergqvist, L., Holmström, E., Varga, L.K., and Vitos, L. (2016). Mechanism of magnetic transition in FeCrCoNi-based high entropy alloys, *Materials & Design*, 103, pp: 71-74. doi: 10.1016/j.matdes.2016.04.053.

[27] Chang, S.-Y., Li, C.-E., Chiang, S.-C., and Huang, Y.-C. (2012). 4-nm thick multilayer structure of multi-component (AlCrRuTaTiZr) Nx as robust diffusion barrier for Cu interconnects, *Journal of Alloys and Compounds*, 515, pp: 4-7. doi: 10.1016/j.jallcom.2011.11.082.

[28] Tsai, M.-H., Yeh, J.-W., and Gan, J.-Y. (2008). Diffusion barrier properties of AlMoNbSiTaTiVZr high-entropy alloy layer between copper and silicon, *Thin Solid Films*, 516 (16), pp: 5527-5530. doi: 10.1016/j.tsf.2007.07.109.

[29] Xia, S., Yang, X., Yang, T., Liu, S., and Zhang, Y. (2015). Irradiation resistance in Al x CoCrFeNi high entropy alloys, *The Minerals, Metals & Materials Society*, 67 (10), pp: 2340-2344. doi: 10.1007/s11837-015-1568-4.

[30] Granberg, F., Nordlund, K., Ullah, M.W., Jin, K., Lu, C., Bei, H., Wang, L., Djurabekova, F., Weber, W., and Zhang, Y. (2016). Mechanism of radiation damage reduction in equiatomic multicomponent single phase alloys, *Physical review letters*, 116 (13), pp: 1-8. doi: 10.1103/PhysRevLett.116.135504.

[31] Xing, Q., Ma, J., Wang, C., and Zhang, Y. (2018). High-throughput screening solar-thermal conversion films in a pseudobinary (Cr, Fe, V)–(Ta, W) system, *ACS combinatorial science,* 20 (11), pp: 602-610.

[32] Zhang, Y., *History of High-Entropy Materials*, in *High-Entropy Materials*2019, Springer: Singapore. p. 1-33.

[33] Li, P., Wang, A., and Liu, C.T. (2017). A ductile high entropy alloy with attractive magnetic properties, *Journal of Alloys and Compounds*, 694, pp: 55-60. doi: 10.1016/j.jallcom.2016.09.186.

[34] Zhang, Y., Zuo, T., Cheng, Y., and Liaw, P.K. (2013). High-entropy alloys with high saturation magnetization, electrical resistivity and malleability, *Scientific reports*, 3 (1), pp: 1-7.

[35] Park, J.H., Hong, Y.K., Bae, S., Lee, J.J., Jalli, J., Abo, G.S., Neveu, N., Kim, S.G., Choi, C.J., and Lee, J.G. (2010). Saturation magnetization and crystalline anisotropy calculations for MnAl permanent magnet, *Journal of applied physics*, 107 (9), pp: 1-3. doi: 10.1063/1.3337640.

[36] Liu, Z.W., Chen, C., Zheng, Z.G., Tan, B.H., and Ramanujan, R.V. (2012). Phase transitions and hard magnetic properties for rapidly solidified MnAl alloys doped with C, B, and rare earth elements, *Journal of materials Science*, 47 (5), pp: 2333-2338. doi: 10.1007/s10853-011-6049-8.

[37] Mishra, R.K. and Shahi, R.R. (2017). Phase evolution and magnetic characteristics of TiFeNiCr and TiFeNiCrM (M= Mn, Co) high entropy alloys, *Journal of Magnetism and Magnetic Materials*, 442, pp: 218-223. doi: 10.1016/j.jmmm.2017.06.124.

[38] Zuo, T., Gao, M.C., Ouyang, L., Yang, X., Cheng, Y., Feng, R., Chen, S., Liaw, P.K., Hawk, J.A., and Zhang, Y. (2017). Tailoring magnetic behavior of CoFeMnNiX (X= Al, Cr, Ga, and Sn) high entropy alloys by metal doping, *Acta Materialia*, 130, pp: 10-18. doi: 10.1016/j.actamat.2017.03.013.

[39] Mishra, R.K., Sahay, P.P., and Shahi, R.R. (2019). Alloying, magnetic and corrosion behavior of AlCrFeMnNiTi high entropy alloy, *Journal of materials Science*, 54 (5), pp: 4433-4443. doi: 10.1007/s10853-018-3153-z.

[40] Hariharan, V.S., Karati, A., Parida, T., John, R., Babu, D.A., and Murty, B.S. (2020). Effect of Al addition and homogenization treatment on the magnetic properties of CoFeMnNi high-entropy alloy, *Journal of materials Science*, 55 (36), pp: 17204-17217. doi: 10.1007/s10853-020-05171-8.

[41] Gao, M.C., Miracle, D.B., Maurice, D., Yan, X., Zhang, Y., and Hawk, J.A. (2018). High-entropy functional materials, *Journal of Materials Research*, 33 (19), pp: 3138-3155. doi: 10.1557/jmr.2018.323.

[42] Huang, K.-H. and Yeh, J. (1996). A study on the multicomponent alloy systems containing equal-mole elements, *Hsinchu: National Tsing Hua University*, 1.

[43] Yeh, J.W., Chen, S.K., Lin, S.J., Gan, J.Y., Chin, T.S., Shun, T.T., Tsau, C.H., and Chang, S.Y. (2004). Nanostructured high-entropy alloys with multiple principal elements: novel alloy design concepts and outcomes, *Advanced Engineering Materials*, 6 (5), pp: 299-303.

[44] Huang, P.K., Yeh, J.W., Shun, T.T., and Chen, S.K. (2004). Multi-principal-element alloys with improved oxidation and wear resistance for thermal spray coating, *Advanced Engineering Materials*, 6 (1-2), pp: 74-78.

[45] Firstov, G.S., Kosorukova, T.A., Koval, Y.N., and Odnosum, V.V. (2015). High entropy shape memory alloys, *Materials Today: Proceedings*, 2, pp: 499-503. doi: 10.1016/j.matpr.2015.07.335

[46] Cantor, B., Chang, I., Knight, P., and Vincent, A. (2004). Microstructural development in equiatomic multicomponent alloys, *Materials Science and Engineering: A*, 375-377, pp: 213-218. doi: 10.1016/j.msea.2003.10.257.

[47] Zhang, C., Gao, M.C., and Lin, S.-K. (2019). Progress in High-Entropy Alloys, *The Minerals, Metals & Materials Society*, 71 (10), pp: 3417-3418. doi: 10.1007/s11837-019-03728-w.

[48] Sheng, G. and Liu, C.T. (2011). Phase stability in high entropy alloys: formation of solid-solution phase or amorphous phase, *Progress in Natural Science: Materials International*, 21 (6), pp: 433-446. doi: 10.1016/S1002-0071(12)60080-X.

[49] Guo, S., Ng, C., Lu, J., and Liu, C.J. (2011). Effect of valence electron concentration on stability of fcc or bcc phase in high entropy alloys, *Journal of Applied Physics,* 109 (10), pp: 1-5. doi: 10.1063/1.3587228.

[50] Urban, K. and Feuerbacher, M. (2004). Structurally complex alloy phases, *Journal of Non-Crystalline Solids*, 334-335, pp: 143-150. doi: 10.1016/j.jnoncrysol.2003.11.029.

[51] Troparevsky, M.C., Morris, J.R., Kent, P.R., Lupini, A.R., and Stocks, G.M. (2015). Criteria for predicting the formation of single-phase high-entropy alloys, *Physical review x*, 5 (1), pp: 1-6. doi: 10.1103/PhysRevX.5.011041.

[52] Cantor, B. (2014). Multicomponent and high entropy alloys, *Entropy*, 16 (9), pp: 4749-4768.

[53] Ye, Y., Wang, Q., Lu, J., Liu, C., and Yang, Y. (2015). Design of high entropy alloys: A single-parameter thermodynamic rule, *Scripta Materialia*, 104, pp: 53-55. doi: 10.1016/j.scriptamat.2015.03.023.

[54] Takeuchi, A., Amiya, K., Wada, T., Yubuta, K., Zhang, W., and Makino, A. (2013). Entropies in alloy design for high-entropy and bulk glassy alloys, *Entropy*, 15 (9), pp: 3810-3821. doi: 10.3390/e15093810.

[55] Kohn, W. and Sham, L.J. (1965). Self-consistent equations including exchange and correlation effects, *Physical review*, 140 (4A), pp: 1133-1138. doi: 10.1103/PhysRev.140.A1133.

[56] Wu, Z., Bei, H., Pharr, G.M., and George, E.P. (2014). Temperature dependence of the mechanical properties of equiatomic solid solution alloys with face-centered cubic crystal structures, *Acta Materialia*, 81, pp: 428-441. doi: 10.1016/j.actamat.2014.08.026.

[57] MacDonald, B., Fu, Z., Zheng, B., Chen, W., Lin, Y., Chen, F., Zhang, L., Ivanisenko, J., Zhou, Y., and Hahn, H. (2017). Recent progress in high entropy alloy research, *The Minerals, Metals & Materials Society*, 69 (10), pp: 2024-2031. doi: 10.1007/s11837-017-2484-6.

[58] Miracle, D.B. and Senkov, O.N. (2017). A critical review of high entropy alloys and related concepts, *Acta Materialia*, 122, pp: 448-511. doi: 10.1016/j.actamat.2016.08.081.

[59] Martyushev, L.M. and Seleznev, V.D. (2006). Maximum entropy production principle in physics, chemistry and biology, *Physics Reports*, 426 (1), pp: 1-45. doi: 10.1016/j.physrep.2005.12.001.

[60] Zhang, Y., Zhou, Y., Hui, X., Wang, M., and Chen, G. (2008). Minor alloying behavior in bulk metallic glasses and high-entropy alloys, *Science in China Series G: Physics, Mechanics and Astronomy*, 51 (4), pp: 427-437.

[61] DR., G., (1995). *Introduction to the thermodynamics of materials*, Taylor & Francis, Washinton (DC)

[62] Cheng, K.-H., Lai, C.-H., Lin, S.-J., and Yeh, J.-W. (2006). Recent progress in multi-element alloy and nitride coatings sputtered from high-entropy alloy targets. in *Annales de chimie (Paris. 1914)*.

[63] Huang, P.K., Yeh, J.W., Shun, T.T., and Chen, S.K. (2004). Multi-principal-element alloys with improved oxidation and wear resistance for thermal spray coating, *Advanced Engineering Materials*, 6 (1-2), pp: 74-78.

[64] Tong, C.-J., Chen, Y.-L., Yeh, J.-W., Lin, S.-J., Chen, S.-K., Shun, T.-T., Tsau, C.-H., and Chang, S.-Y. (2005). Microstructure characterization of Al x CoCrCuFeNi high-entropy alloy system with multiprincipal elements, *Metallurgical and Materials Transactions A*, 36 (4), pp: 881-893.

[65] Tsai, K.-Y., Tsai, M.-H., and Yeh, J.-W. (2013). Sluggish diffusion in Co–Cr–Fe–Mn–Ni high-entropy alloys, *Acta Materialia*, 61 (13), pp: 4887-4897. doi: 10.1016/j.actamat.2013.04.058.

[66] Vaidya, M., Trubel, S., Murty, B., Wilde, G., and Divinski, S.V. (2016). Ni tracer diffusion in CoCrFeNi and CoCrFeMnNi high entropy alloys, *Journal of Alloys and Compounds*, 688, pp: 994-1001.

[67] Tsai, C.-W., Chen, Y.-L., Tsai, M.-H., Yeh, J.-W., Shun, T.-T., and Chen, S.-K. (2009). Deformation and annealing behaviors of high-entropy alloy $Al_{0.5}$CoCrCuFeNi, *Journal of Alloys and Compounds*, 486 (1-2), pp: 427-435.

[68] Senkov, O.N., Wilks, G., Scott, J., and Miracle, D.B. (2011). Mechanical properties of $Nb_{25}Mo_{25}Ta_{25}W_{25}$ and $V_{20}Nb_{20}Mo_{20}Ta_{20}W_{20}$ refractory high entropy alloys, *Intermetallics*, 19 (5), pp: 698-706. doi: 10.1016/j.intermet.2011.01.004.

[69] Kelsall, R.W., Hamley, I.W., and Geoghegan, M., (2005). *Nanoscale science and technology*, Wiley Online Library,

[70] Yeh, J.-W., Chang, S.-Y., Hong, Y.-D., Chen, S.-K., Lin, S.-J. (2007). Anomalous decrease in X-ray diffraction intensities of Cu–Ni–Al–Co–Cr–Fe–Si alloy systems with multi-principal elements, *Materials chemistry and physics,* 103 (1), pp: 41-46.

[71] Yeh, J.-W., Lin, S.-J., Chin, T.-S., Gan, J.-Y., Chen, S.-K., Shun, T.-T., Tsau, C.-H., and Chou, S.-Y. (2004). Formation of simple crystal structures in Cu-Co-Ni-Cr-Al-Fe-Ti-V alloys with multiprincipal metallic elements, *Metallurgical Materials Transactions A*, 35 (8), pp: 2533-2536.

[72] Tsai, M.-H. (2013). Physical properties of high entropy alloys, *Entropy*, 15 (12), pp: 5338-5345. doi: 10.3390/e15125338.

[73] Zou, Y., Maiti, S., Steurer, W., and Spolenak, R. (2014). Size-dependent plasticity in an $Nb_{25}Mo_{25}Ta_{25}W_{25}$ refractory high-entropy alloy, *Acta Materialia*, 65, pp: 85-97. doi: 10.1016/j.actamat.2013.11.049.

[74] Yeh, J.-W. (2015). Physical metallurgy of high-entropy alloys, *The Minerals, Metals & Materials Society*, 67 (10), pp: 2254-2261.

[75] Ranganathan, S. (2003). Alloyed pleasures: multimetallic cocktails, *Current science*, 85 (10), pp: 1404-1406.

[76] Chen, M.-R., Lin, S.-J., Yeh, J.-W., Chuang, M.-H., Chen, S.-K., and Huang, Y.-S. (2006). Effect of vanadium addition on the microstructure, hardness, and wear resistance of Al $_{0.5}$ CoCrCuFeNi high-entropy alloy, *METALLURGICAL AND MATERIALS TRANSACTIONS*, 37A (5), pp: 1363-1369.

[77] Wu, J.-M., Lin, S.-J., Yeh, J.-W., Chen, S.-K., Huang, Y.-S., and Chen, H.-C. (2006). Adhesive wear behavior of AlxCoCrCuFeNi high-entropy alloys as a function of aluminum content, *Wear*, 261 (5-6), pp: 513-519. doi: 10.1016/j.wear.2005.12.008.

[78] Mizutani, U., (2010). *The Hume-Rothery rules for structurally complex alloy phases*, in *Surface Properties And Engineering Of Complex Intermetallics*, World Scientific. p. 323-399.

[79] Yang, X., Zhang, Y., and Liaw, P. (2012). Microstructure and compressive properties of NbTiVTaAlx high entropy alloys, *Procedia Engineering*, 36, pp: 292-298. doi: 10.1016/j.proeng.2012.03.043

[80] Chen, R., Qin, G., Zheng, H., Wang, L., Su, Y., Chiu, Y., Ding, H., Guo, J., and Fu, H. (2018). Composition design of high entropy alloys using the valence electron concentration to balance strength and ductility, *Acta Materialia*, 144, pp: 129-137. doi: 10.1016/j.actamat.2017.10.058.

[81] Yang, X. and Zhang, Y. (2012). Prediction of high-entropy stabilized solid-solution in multi-component alloys, *Materials Chemistry and Physics*, 132 (2-3), pp: 233-238. doi: 10.1016/j.matchemphys.2011.11.021.

[82] Takeuchi, A. and Inoue, A. (2005). Classification of bulk metallic glasses by atomic size difference, heat of mixing and period of constituent elements and its application to characterization of the main alloying element, *Materials Transactions*, 46 (12), pp: 2817-2829.

[83] Cahn, R.W. and Haasen, P., *Editors. Physical Metallurgy*, 1996, Elsevier Amsterdam.

[84] Zhang, Y., Zhou, Y.J., Lin, J.P., Chen, G.L., and Liaw, P.K. (2008). Solid-solution phase formation rules for multi-component alloys, *Advanced Engineering Materials*, 10 (6), pp: 534-538.

[85] Singh, S., Wanderka, N., Murty, B.S., Glatzel, U., and Banhart, J. (2011). Decomposition in multi-component AlCoCrCuFeNi high-entropy alloy, *Acta Materialia*, 59 (1), pp: 182-190.

[86] Tsai, M.-H., Yuan, H., Cheng, G., Xu, W., Tsai, K.-Y., Tsai, C.-W., Jian, W.W., Juan, C.-C., Shen, W.-J., and Chuang, M.-H. (2013). Morphology, structure and composition of precipitates in Al0. 3CoCrCu0. 5FeNi high-entropy alloy, *Intermetallics*, 32, pp: 329-336.

[87] Tsai, M.-H., Yuan, H., Cheng, G., Xu, W., Jian, W.W., Chuang, M.-H., Juan, C.-C., Yeh, A.-C., Lin, S.-J., and Zhu, Y. (2013). Significant hardening due to the formation of a sigma phase matrix in a high entropy alloy, *Intermetallics*, 33, pp: 81-86.

[88] Kao, Y.-F., Chen, T.-J., Chen, S.-K., and Yeh, J.-W. (2009). Microstructure and mechanical property of as-cast,-homogenized, and-deformed AlxCoCrFeNi ($0 \leq x \leq 2$) high-entropy alloys, *Journal of Alloys and Compounds*, 488 (1), pp: 57-64.

[89] Tsau, C.-H. and Chang, Y.-H. (2013). Microstructures and mechanical properties of TiCrZrNbNx alloy nitride thin films, *Entropy*, 15 (11), pp: 5012-5021.

[90] Zhao, Y.J., Qiao, J.W., Ma, S.G., Gao, M.C., Yang, H.J., Chen, M.W., and Zhang, Y. (2016). A hexagonal close-packed high-entropy alloy: The effect of entropy, *Materials & Design*, 96, pp: 10-15.

[91] Guo, S., Ng, C., Lu, J., and Liu, C.T. (2011). Effect of valence electron concentration on stability of fcc or bcc phase in high entropy alloys, *Journal of applied physics*, 109 (10), pp: 1-5. doi: 10.1063/1.3587228.

[92] Hsu, C.-Y., Yeh, J.-W., Chen, S.-K., and Shun, T.-T. (2004). Wear resistance and high-temperature compression strength of Fcc CuCoNiCrAl $_{0.5}$ Fe alloy with boron addition, *Metallurgical and Materials Transactions A*, 35 (5), pp: 1465-1469.

[93] Wen, L.H., Kou, H.C., Li, J.S., Chang, H., Xue, X.Y., and Zhou, L. (2009). Effect of aging temperature on microstructure and properties of AlCoCrCuFeNi high-entropy alloy, *Intermetallics*, 17 (4), pp: 266-269.

[94] Pickering, E.J. and Jones, N.G. (2016). High-entropy alloys: a critical assessment of their founding principles and future prospects, *International Materials Reviews*, 61 (3), pp: 183-202. doi: 10.1080/09506608.2016.1180020.

[95] Zhang, C., Zhang, F., Chen, S., and Cao, W. (2012). Computational thermodynamics aided high-entropy alloy design, *The Minerals, Metals & Materials Society*, 64 (7), pp: 839-845.

[96] Senkov, O.N., Miller, J.D., Miracle, D.B., and Woodward, C. (2015). Accelerated exploration of multi-principal element alloys with solid solution phases, *Nature communications*, 6 (1), pp: 1-10.

[97] Ng, C., Guo, S., Luan, J., Shi, S., and Liu, C.T. (2012). Entropy-driven phase stability and slow diffusion kinetics in an Al0. 5CoCrCuFeNi high entropy alloy, *Intermetallics*, 31, pp: 165-172.

[98] George, E.P., Raabe, D., and Ritchie, R.O. (2019). High-entropy alloys, *Nature Reviews Materials*, 4 (8), pp: 515-534. doi: 10.1038/s41578-019-0121-4.

[99] George, E.P., Curtin, W., and Tasan, C.C.J.A.M. (2020). High entropy alloys: A focused review of mechanical properties and deformation mechanisms, *Acta Materialia*, 188, pp: 435-474. doi: 10.1016/j.actamat.2019.12.015.

[100] Kao, Y.-F., Chen, S.-K., Chen, T.-J., Chu, P.-C., Yeh, J.-W., and Lin, S.-J. (2011). Electrical, magnetic, and Hall properties of AlxCoCrFeNi high-entropy alloys, *Journal of Alloys and Compounds*, 509 (5), pp: 1607-1614. doi: 10.1016/j.jallcom.2010.10.210.

[101] Liu, L., Zhu, J.B., Li, J.C., and Jiang, Q. (2012). Microstructure and magnetic properties of FeNiCuMnTiSnx high entropy alloys, *Advanced Engineering Materials*, 14 (10), pp: 919-922. doi: 10.1002/adem.201200104.

[102] Zhang, Y., Zuo, T., Cheng, Y., and Liaw, P.K. (2013). High-entropy alloys with high saturation magnetization, electrical resistivity, and malleability, *Scientific reports*, 3, pp: 1-7. doi: 10.1038/srep01455.

[103] Lucas, M., Mauger, L., Munoz, J., Xiao, Y., Sheets, A., Semiatin, S., Horwath, J., and Turgut, Z. (2011). Magnetic and vibrational properties of high-entropy alloys, *Journal of Aplied Physics*, 109 (7), pp: 1-3. doi: 10.1063/1.3538936].

[104] Wang, X., Zhang, Y., Qiao, Y., and Chen, G. (2007). Novel microstructure and properties of multicomponent CoCrCuFeNiTix alloys, *Intermetallics*, 15 (3), pp: 357-362. doi: 10.1016/j.intermet.2006.08.005.

[105] Singh, S., Wanderka, N., Kiefer, K., Siemensmeyer, K., and Banhart, J. (2011). Effect of decomposition of the Cr–Fe–Co rich phase of AlCoCrCuFeNi high entropy alloy on magnetic properties, *Ultramicroscopy*, 111 (6), pp: 619-622. doi: 10.1016/j.ultramic.2010.12.001.

[106] Chou, H.-P., Chang, Y.-S., Chen, S.-K., and Yeh, J.-W. (2009). Microstructure, thermophysical and electrical properties in AlxCoCrFeNi ($0 \leq x \leq 2$) high-entropy alloys, *Materials Science and Engineering: B,* 163 (3), pp: 184-189. doi: 10.1016/j.mseb.2009.05.024.

[107] Shackelford, J.F., Han, Y.-H., Kim, S., and Kwon, S.-H., (2016). *CRC materials science and engineering handbook*, CRC press,

[108] Hsu, C.-Y., Juan, C.-C., Wang, W.-R., Sheu, T.-S., Yeh, J.-W., and Chen, S.-K. (2011). On the superior hot hardness and softening resistance of $AlCoCrxFeMo_{0.5}Ni$ high-entropy alloys, *Materials Science Engineering: A*, 528 (10-11), pp: 3581-3588. doi: 10.1016/j.msea.2011.01.072.

[109] Shi, Y., Yang, B., and Liaw, P.K. (2017). Corrosion-resistant high-entropy alloys: A review, *Metals*, 7 (2), pp: 1-18. doi: 10.3390/met7020043.

[110] Chen, Y., Duval, T., Hung, U., Yeh, J., and Shih, H. (2005). Microstructure and electrochemical properties of high entropy alloys—a comparison with type-304 stainless steel, *Corrosion Science*, 47 (9), pp: 2257-2279. doi: 10.1016/j.corsci.2004.11.008.

[111] Chou, Y., Yeh, J., and Shih, H. (2010). The effect of molybdenum on the corrosion behaviour of the high-entropy alloys $Co_{1.5}CrFeNi_{1.5}Ti_{0.5}Mox$ in aqueous environments, *Corrosion Science*, 52 (8), pp: 2571-2581. doi: 10.1016/j.corsci.2010.04.004.

[112] Kao, Y.-F., Lee, T.-D., Chen, S.-K., and Chang, Y.-S. (2010). Electrochemical passive properties of AlxCoCrFeNi (x= 0, 0.25, 0.50, 1.00) alloys in sulfuric acids, *Corrosion Science*, 52 (3), pp: 1026-1034. doi: 10.1016/j.corsci.2009.11.028.

[113] Hsu, Y.-J., Chiang, W.-C., Wu, J.-K.J.M.C., and Physics. (2005). Corrosion behavior of FeCoNiCrCux high-entropy alloys in 3.5% sodium chloride solution, 92 (1), pp: 112-117.

[114] Lin, C.-M., Tsai, H.-L., and Bor, H.-Y. (2010). Effect of aging treatment on microstructure and properties of high-entropy $Cu_{0.5}CoCrFeNi$ alloy, *Intermetallics*, 18 (6), pp: 1244-1250. doi: 10.1016/j.intermet.2010.03.030.

[115] Lee, C., Chang, C., Chen, Y., Yeh, J., and Shih, H. (2008). Effect of the aluminium content of $AlxCrFe_{1.5}MnNi_{0.5}$ high-entropy alloys on the corrosion behaviour in aqueous environments, *Corrosion Science*, 50 (7), pp: 2053-2060. doi: 10.1016/j.corsci.2008.04.011.

[116] Inkson, B.J., (2016). *Scanning electron microscopy (SEM) and transmission electron microscopy (TEM) for materials characterization*, in *Materials characterization using nondestructive evaluation (NDE) methods*, Elsevier. p. 17-43.

[117] Ibrahim, P.A., Özkul, İ., and Canbay, C.A. (2021). An Experimental Study on High Entropy Alloy Using Different Alloying Elements, *JOURNAL OF MATERIALS AND ELECTRONIC DEVICES*, 1 (1), pp: 11-15.

[118] Shindo, D. and Oikawa, T., (2013). *Analytical electron microscopy for materials science*, Springer Science & Business Media,

[119] Scimeca, M., Bischetti, S., Lamsira, H.K., Bonfiglio, R., and Bonanno, E. (2018). Energy Dispersive X-ray (EDX) microanalysis: A powerful tool in biomedical research and diagnosis, *European journal of histochemistry: EJH*, 62 (2841), pp: 89-98. doi: 10.4081%2Fejh.2018.2841.

[120] Canbay, C.A., Karaduman, O., Ibrahim, P.A., and Ozkul, İ. (2021). Thermostructural shape memory effect observations of ductile Cu-Al-Mn smart alloy, *Advances in materials Research*, 10 (1), pp: 45-56. doi: 10.12989/amr.2021.10.1.045.

[121] Bunaciu, A.A., UdriŞTioiu, E.G., and Aboul-Enein, H.Y. (2015). X-ray diffraction: instrumentation and applications, *Critical reviews in analytical chemistry*, 45 (4), pp: 289-299. doi: 10.1080/10408347.2014.949616.

[122] Ahmed, H.M., Canbay, C.A., and Özkul, İ. (2019). Fabrication of quaternary high temperature shape memory alloys. in *Turkish Physical Society 35th International Physics Congress (TPS35)*. Turkey, Bodrum AIP Publishing LLC.

[123] Jauncey, G.E.M. (1924). The scattering of x-rays and Bragg's law, *Proceedings of the National Academy of Sciences of the United States of America*, 10 (2), pp: 57-60. doi: 10.1073%2Fpnas.10.2.57.

[124] Foner, S. (1996). The vibrating sample magnetometer: Experiences of a volunteer, *Journal of applied physics*, 79 (8), pp: 4740-4745. doi: 10.1063/1.361657.

[125] Bowden, G.J. (1972). Detection coil systems for vibrating sample magnetometers, *Journal of Physics E: Scientific Instruments*, 5 (11), pp: 11-15.

[126] Paulik, F., (1995). *Special trends in thermal analysis*, Wiley,

[127] Ozawa, T. (2000). Thermal analysis—review and prospect, *Thermochimica Acta*, 355 (1-2), pp: 35-42. doi: 10.1016/S0040-6031(00)00435-4.

[128] Taylor, A., Kagle, B., and Beiter, E. (1961). Geometrical Representation and X-Ray Fluorescence Analysis of Ternary Alloys, *Analytical Chemistry*, 33 (12), pp: 1699-1706.

[129] Senkov, O.N. and Miracle, D.B. (2001). Effect of the atomic size distribution on glass forming ability of amorphous metallic alloys, *Materials Research Bulletin*, 36 (12), pp: 2183-2198. doi: 10.1016/S0025-5408(01)00715-2.

[130] Zhang, J.J., Yin, X.L., Dong, Y., Lu, Y.P., Jiang, L., Wang, T.M., and Li, T.J. (2014). Corrosion properties of AlxCoCrFeNiTi$_{0.5}$ high entropy alloys in 0· 5M H2SO4 aqueous solution, *Materials Research Innovations*, 18 (sup4), pp: 756-760. doi: 10.1179/1432891714Z.000000000778.

[131] Y. Qiu, M.A.G., H. L. Fraser, and N. Birbilis. (2015). Corrosion characteristics of high entropyalloys, *Materials Science and Technology*, 31 (10), pp: 1235-1243. doi: 10.1179/1743284715Y.0000000026.

[132] Guo, S., Ng, C., Lu, J., and Liu, C. (2011). Effect of valence electron concentration on stability of fcc or bcc phase in high entropy alloys, *Journal of applied physics*, 109 (10), pp: 103505.

[133] Zhang, A., Han, J., Meng, J., Su, B., and Li, P. (2016). Rapid preparation of AlCoCrFeNi high entropy alloy by spark plasma sintering from elemental powder mixture, *Materials letters*, 181, pp: 82-85. doi: 10.1016/j.matlet.2016.06.014.

[134] Dong, Y. and Lu, Y. (2019). Microstructure and Mechanical Properties of CoCrFeNi2Al1-xWx High Entropy Alloys, *Arabian Journal for Science & Engineering (Springer Science & Business Media BV)*, 44 (2), pp: 803-808. doi: 10.1007/s13369-018-3297-9.

[135] Wu, C.-S., Tsai, P.-H., Kuo, C.-M., and Tsai, C.-W. (2018). Effect of atomic size difference on the microstructure and mechanical properties of high-entropy alloys, *Entropy*, 20 (12), pp: 1-10. doi: 10.3390/e20120967.

[136] Erdal, Z.A., (2020). *Structural and mechanical characterization of scale-up FeCoCrNi, FeCoCrNiCux, AND FeCoCrNiAlx high entropy alloys (HEAs)*, Master thesis, Middle East Technical University.

[137] Marattukalam, J.J., Balla, V.K., Das, M., Bontha, S., and Kalpathy, S.K. (2018). Effect of heat treatment on microstructure, corrosion, and shape memory characteristics of laser deposited NiTi alloy, *Journal of Alloys and Compounds*, 744, pp: 337-346. doi: 10.1016/j.jallcom.2018.01.174.

[138] Quéré, D. (2005). Non-sticking drops, *Reports on Progress in Physics*, 68 (11), pp: 2495.

[139] Zhang, K. and Fu, Z. (2012). Effects of annealing treatment on phase composition and microstructure of CoCrFeNiTiAlx high-entropy alloys, *Intermetallics*, 22, pp: 24-32. doi: 10.1016/j.intermet.2011.10.010.

[140] Karati, A., Guruvidyathri, K., Hariharan, V.S., and Murty, B.S. (2019). Thermal stability of AlCoFeMnNi high-entropy alloy, *Scripta Materialia*, 162, pp: 465-467. doi: 10.1016/j.scriptamat.2018.12.017.

[141] Cui, P., Ma, Y., Zhang, L., Zhang, M., Fan, J., Dong, W., Yu, P., Li, G., and Liu, R. (2018). Effect of Ti on microstructures and mechanical properties of high entropy alloys based on CoFeMnNi system, *Materials Science and Engineering: A*, 737, pp: 198-204. doi: 10.1016/j.msea.2018.09.050.

[142] Zuo, T.T., Li, R.B., Ren, X.J., and Zhang, Y. (2014). Effects of Al and Si addition on the structure and properties of CoFeNi equal atomic ratio alloy, *Journal of Magnetism and Magnetic Materials*, 371, pp: 60-68. doi: 10.1016/j.jmmm.2014.07.023.

[143] Mishra, R.K. and Shahi, R.R. (2018). *Magnetic characteristics of high entropy alloys*, in *Magnetism and magnetic materials*, IntechOpen. p. 67-80.

[144] Li, Z., Gu, Y., Wang, C., Pan, M., Zhang, H., Wu, Z., Hou, X., Tan, X., and Xu, H. (2019). Microstructure and magnetic properties of the FeCoNi (CuAl) $_{0.8}$ Ga$_{0.06}$ high-entropy alloy during the phase transition, *Journal of Alloys and Compounds*, 779, pp: 293-300. doi: 10.1016/j.jallcom.2018.11.235.

[145] Feng, W., Qi, Y., and Wang, S. (2018). Effects of Mn and Al addition on structural and magnetic properties of FeCoNi-based high entropy alloys, *Materials Research Express*, 5 (10), pp: 1-13. doi: 10.1088/2053-1591/aadaa7.

[146] Li, P., Wang, A., and Liu, C.T. (2017). Composition dependence of structure, physical and mechanical properties of FeCoNi (MnAl) x high entropy alloys, *Intermetallics*, 87, pp: 21-26. doi: 10.1016/j.intermet.2017.04.007.

[147] Ghasemi, A., Zamani, K., Tavoosi, M., and Gordani, G.R. (2020). Enhanced Soft Magnetic Properties of CoNi-Based High Entropy Alloys, *Journal of superconductivity and novel magnetism*, 33 (10), pp: 3189-3196. doi: 10.1007/s10948-020-05579-y.

[148] Chaudhary, V., Gwalani, B., Soni, V., Ramanujan, R.V., and Banerjee, R. (2018). Influence of Cr substitution and temperature on hierarchical phase decomposition in the AlCoFeNi high entropy alloy, *Scientific reports*, 8 (15578), pp: 1-12. doi: 10.1038/s41598-018-33922-w.

[149] Ma, S.G. and Zhang, Y. (2012). Effect of Nb addition on the microstructure and properties of AlCoCrFeNi high-entropy alloy, *Materials Science and Engineering: A*, 532, pp: 480-486. doi: 10.1016/j.msea.2011.10.110.

[150] Li, Z., Wang, C., Yu, L., Gu, Y., Pan, M., Tan, X., and Xu, H. (2018). Magnetic properties and microstructure of FeCoNi (CuAl) $_{0.8}$ Snx ($0\leq x\leq 0.10$) high-entropy alloys, *Entropy*, 20 (872), pp: 1-11. doi: 10.3390/e20110872.

[151] Alijani, F., Reihanian, M., and Gheisari, K. (2019). Study on phase formation in magnetic FeCoNiMnV high entropy alloy produced by mechanical alloying, *Journal of Alloys and Compounds*, 773, pp: 623-630. doi: 10.1016/j.jallcom.2018.09.204.

[152] Zuo, T.-t., Ren, S.-b., Liaw, P.K., and Zhang, Y. (2013). Processing effects on the magnetic and mechanical properties of FeCoNiAl $_{0.2}$ Si $_{0.2}$ high entropy alloy, *International Journal of Minerals, Metallurgy, and Materials*, 20 (6), pp: 549-555. doi: 10.1007/s12613-013-0764-x.

[153] Zuo, T., Zhang, M., Liaw, P.K., and Zhang, Y. (2018). Novel high entropy alloys of FexCo1-xNiMnGa with excellent soft magnetic properties, *Intermetallics*, 100, pp: 1-8. doi: 10.1016/j.intermet.2018.05.014.

[154] Li, Z., Xu, H., Gu, Y., Pan, M., Yu, L., Tan, X., and Hou, X. (2018). Correlation between the magnetic properties and phase constitution of FeCoNi (CuAl) $_{0.8}$ Gax ($0\leq x\leq 0.08$) high-entropy alloys, *Journal of Alloys and Compounds*, 746, pp: 285-291. doi: 10.1016/j.jallcom.2018.02.189.

[155] Yang, C., Zhang, J., Li, M., and Liu, X. (2020). Soft-Magnetic High-Entropy AlCoFeMnNi Alloys with Dual-Phase Microstructures Induced by Annealing, *Acta Metallurgica Sinica (English Letters)*, 33 (8), pp: 1124-1134.

[156] Bahrami, A., Mohammadnejad, A., and Sajadi, M. (2021). Microstructure and mechanical properties of spark plasma sintered AlCoFeMnNi high entropy alloy (HEA)-carbon nanotube (CNT) nanocomposite, *Journal of Alloys and Compounds*, 862, pp: 1-7. doi: 10.1016/j.jallcom.2020.158577

CURRICULUM VITAE

Pshdar Ahmed IBRAHIM

[redacted]

ACADEMIC ACTIVITIES

Paper:

1. Canbay, C.A., Karaduman, O., Ibrahim, P.A., and Ozkul, I. (2021). Thermostructural shape memory effect observations of ductile Cu-Al-Mn smart alloy, *Advances in materials Research*, 10 (1), pp: 45-56. Doi: 10.12989/amr.2021.10.1.045
2. Ibrahim, P.A., Özkul, I., and Canbay, C.A. (2021). An Experimental Study on High Entropy Alloy Using Different Alloying Elements, *Journal of Materials and Electronic Devices*, 1 (1), pp: 11-15.
3. Ibrahim, P.A., Özkul, İ., and Canbay, C.A. (2021). Methodological Research of High Entropy Alloys by Using Bibliometrics Analysis, *Journal of Materials and Electronic Devices*, 5 (1), pp: 7-13.

Oral presentations at Conferences:

1. Canbay, C.A., Karaduman, O., Ibrahim, P.A., and Özkul, İ. (2020). SME Observations of Cu-Al based SMA in *TFD36,* Bodrum, Turkey.
2. Canbay, C.A., Özkul, İ., Güler, Ö., Güler, S.H., and Ibrahim, P.A. (2020). Effect of B4C Adding on NiCoFeAlMoTiCr High Entropy Alloy in *TFD36*, Bodrum, Turkey.
3. Ibrahim, P.A., Özkul, İ., and Canbay, C.A. (2021). Methodological Review of the Literature Refers to High Entropy Alloys by using Bibliometrics Analysis in *MSNG2021,* Elazig, Turkey.
4. Ibrahim, P.A., Özkul, İ., and Canbay, C.A. (2021). Microstructure and magnetic properties of the AlCoFeMnNi-X(X=Ga, V) High entropy alloys in *TFD37,* Bodrum, Turkey.
5. Özkul, İ., Karaduman, O., Canbay, C.A., Ibrahim, P.A., and AK, İ. (2021). Thermomechanical and Structural Effect of the Quaternary Alloying Elements on Cu Based Shape Memory in *TFD37,* Bodrum, Turkey.

Projects:

This thesis was supported by Firat University Scientific Research Projects Coordination Unit (FÜBAP) with the project number **FF.21.11.**